April 2021

Synthesis of Inorganic Porous Materials With Tunable Morphology for Molecular Adsorption and Separation

Sanket Sabnis
University of Massachusetts Amherst

SYNTHESIS OF INORGANIC POROUS MATERIALS WITH TUNABLE MORPHOLOGY FOR MOLECULAR ADSORPTION AND SEPARATION

A Dissertation Presented

by

SANKET U. SABNIS

Submitted to the Graduate School of the
University of Massachusetts Amherst in partial fulfillment
of the requirements for the degree of

DOCTOR OF PHILOSOPHY

February 2021

Department of Chemical Engineering

SYNTHESIS OF INORGANIC POROUS MATERIALS WITH TUNABLE MORPHOLOGY FOR MOLECULAR ADSORPTION AND SEPARATION

A Dissertation Presented

by

SANKET U. SABNIS

Approved as to style and content by:

_____
Wei Fan, Chair

_____
H. Henning Winter, Member

_____
Stephen Nonnenmann, Outside Member

_____
Michael Henson, Interim Head
Department of Chemical Engineering
University of Massachusetts Amherst

DEDICATION

To my grandparents,
Urmila and Late Prabhakar Masurekar
Late Prema and Late Jayavant Sabnis

ACKNOWLEDGMENTS

This work was supported by the Catalysis Center for Energy Innovation, an Energy Frontier Research Center funded by the U.S. Department of Energy, Office of Science, Basic Energy Sciences under award number DE-SC0001004 and U.S. National Science Foundation (CMMI-1334460). This work was also supported by U.S. Department of Energy, Office of Science, Basic Energy Sciences, Material Sciences and Engineering Division, under award number DE-SC0019170 and by ACS-PRF (58675-ND10).

I would like to thank my advisor Prof. Wei Fan and past and present members of the Fan research group- Dr. Hong Je Cho, Dr. Xiaoduo Qi, Dr. Vivek Vattipalli, Jason Gulbinski, Song Luo, Dr. Qiyu Liu and Kaivalya Gawande. I would also like to thank my collaborator and committee member, Prof. H. Henning Winter. I would also like to thank Dr. Vijesh Tanna for help with rheology experiments and for many stimulating discussions. I would like to thank my other committee member, Prof. Stephen Nonnenmann. I would like to thank Dr. Jiaxin Zhu for help with AFM imaging. I would like to thank Prof. Omar Abdelrahman and his research group members, Ajibola Lawal and Han Chen. I would like to thank Prof. Michael Tsapatsis and his research group member, Xuekui Duan. I would like to thank Prof. Zhiping Lai and his research group member, Guan Sheng. I would also like to thank Prof. Lili He and Dr. Yanqi Qu for help with Raman spectroscopy. I would like to thank Dr. Alexander Ribbe and Louis Raboin for training me on using TEM and SEM. I would like to thank the ChE department staff- Amity Lee, Marie Wallace, Joe Smith and Gary Czupkiewicz. I would also like to thank Prof. Sarah Perry for her kind support.

I would like to thank my friends in Amherst- Mimi Alkattan, Arpita Biswas, Laura Fattaruso, Dr. Raquel Bryant, Rose Berns-Zieve, Edwin Murenzi, Nigel Golden, Rene Cabrera, Cynthia Cabrera, Marsha Allen, Debadatta Chakraborty, Onupurba Das, Sarah McKnight, Mariela Garcia Arredondo, Bogumila Backiel, Dr. Benjamin Keisling, Phoebe Bisnoff, Sophia Kramer, Dr. Pritha Dutta, Hia Ghosh, Meghna Marjadi, Shaina Sadai, Robin Zollner, Chinedum Eluwa and Lila Durán Ruiz. In addition, I would like to thank all the members of oSTEM UMass Amherst, Graduate Students of Color Association (GSCA) and Graduate Women in STEM (GWIS).

Lastly, I would like to thank my parents, Ulhas and Madhavi Sabnis, for their constant love and support.

ABSTRACT

SYNTHESIS OF INORGANIC POROUS MATERIALS WITH TUNABLE MORPHOLOGY FOR MOLECULAR ADSORPTION AND SEPARATION

FEBRUARY 2021

Sanket U. Sabnis, B.Chem.Engg., Institute of Chemical Technology, Mumbai

Ph.D., University of Massachusetts Amherst

Directed by: Professor Wei Fan

Global industrial and economic development over the past century has largely relied on combustion of non-renewable fossil fuels, such as petroleum, coal, and natural gas, which are also harmful to environment because of the release of CO_2, responsible for global warming and climate change. Establishing eco-friendly, energy-efficient and cost-effective processes to reduce environmental impact is currently one of the most urgent issues for the sustainable development of our society. Inorganic porous materials have found applications in the fields of renewable energy and environmental protection such as biomass conversion, fuel cells, thermal energy storage, CO_2 capture and conversion, air pollution remediation, water purification, etc. Their advantages such as high surface area, tunable properties and stability at high temperatures and high pressures make them potential candidates as solutions to the sustainability issues in our society. In this thesis, we synthesized inorganic porous materials, namely zeolites and mesoporous carbons, by tuning their morphology, hydrophobicity and micro- and mesopore structure.

Mesoporous carbons with functional surface groups have recently received significant attention as catalysts for cellulose hydrolysis and as adsorbents for sugars due

to their low cost, hydrothermal stability and ability of their graphitic domains to bond with sugars with CH-π interactions. In the first part of this thesis, a three-dimensionally ordered mesoporous (3DOm) carbon was synthesized as a potential adsorbent for the recovery of glucose obtained from cellulose hydrolysis in molten salt hydrate. Lanthanum-embedded silica nanoparticles were used as a template and ethylene was used as a carbon source to achieve a graphitic structure.

Zeolites (microporous aluminosilicates) are normally synthesized under hydrothermal conditions in a sealed autoclave, which involves the use of a large amount of water as a solvent leading to high autogenous pressures, and safety and environmental issues. Recent research on solvent-free synthesis of zeolites, poses a question whether autogenous pressure is required for crystallization of zeolites or whether zeolites can be synthesized at atmospheric pressure. An atmospheric, solvent-free synthesis can lead to reduction in recycling and waste costs and can lead to potential capital savings from a reduction in the need for pressure vessels In the second part of this thesis, the role of water and autogenous pressure in vapor-phase transport method for zeolite (silicalite-1) synthesis was investigated.

About one third of the CO_2 emissions in the U.S. come from the electric power sector, a major fraction of which come from coal power plants. A hydrogen-selective membrane reactor can replace the energy-intensive solvent-based process used for CO_2 capture in an IGCC power plant. ITQ-1(P), a two-dimensional layered zeolite with MWW framework is an excellent candidate for fabrication of such a membrane. The MWW framework contains six-membered ring (~0.3 nm) apertures that can allow the passage of H_2 but restrict the passage of CO_2. The current challenge is to develop a facile method for

exfoliation of ITQ-1(P), to obtain high aspect-ratio MWW nanosheets. The other challenge is to form a uniformly oriented, defect-free coating of these nanosheets on a porous support, while minimizing the film-thickness to achieve high flux. In the third part of this thesis, a successful room temperature self-exfoliation of swollen ITQ-1(P) in commercially available liquid hydroxyl-terminated polybutadiene (HTPB) was achieved, and high-aspect ratio nanosheets were obtained. A uniform coating of MWW nanosheets on a sintered silica fiber (SSF) support was achieved by vacuum filtration. A successful gel-free secondary growth was performed on this coating by preserving its preferred orientation. The effects of framework aluminum and nature of organic structure directing agent (OSDA) in the interlayer on exfoliation were studied. The polymer-zeolite interactions were studied using rheology, highlighting the role of polymer end-groups in exfoliation.

TABLE OF CONTENTS

Page

LIST OF TABLES

Table Page

LIST OF FIGURES

Figure Page

CHAPTER 1

INTRODUCTION

1.1. Inorganic porous materials for sustainable chemistry

Sustainability represents a state of society where living conditions and resources continue to meet human needs without undermining the integrity and stability of the natural systems. Global industrial and economic development over the past century has largely relied on combustion of non-renewable fossil fuels, such as petroleum, coal, and natural gas, which are also harmful to our environment because of the release of a large amount of CO_2. Meanwhile, industrial processes and human activities have produced various hazardous gases, such as NO, NO_2, NH_3, and volatile organic compounds, and liquid wastes containing heavy metals and radionuclides, which have posed serious threats to the environment and human health. Therefore, establishing eco-friendly and cost-effective processes to achieve renewable energy sources and environmental improvement is currently one of the most urgent issues for the sustainable development of our society. To achieve this, many efforts have been made to develop new materials and technologies.[1]

Porous materials comprise of a network of ordered and disordered pores or voids and are normally characterized by low density, high surface area, controllable pore sizes, surface functionalities and tunable compositions. They have a great potential in many applications such as separations and adsorption, energy storage, heterogenous catalysis, sensing and drug delivery.[2] Materials with pore widths of less than 2 nm are classified as microporous, those with pore sizes between 2 and 50 nm are mesoporous and those with pore sizes between 50 and 1000 nm are called macroporous. Although the field of porous

materials has matured, further improvement is still required to achieve their economical synthesis, and extend their use to new areas to meet new technological challenges.

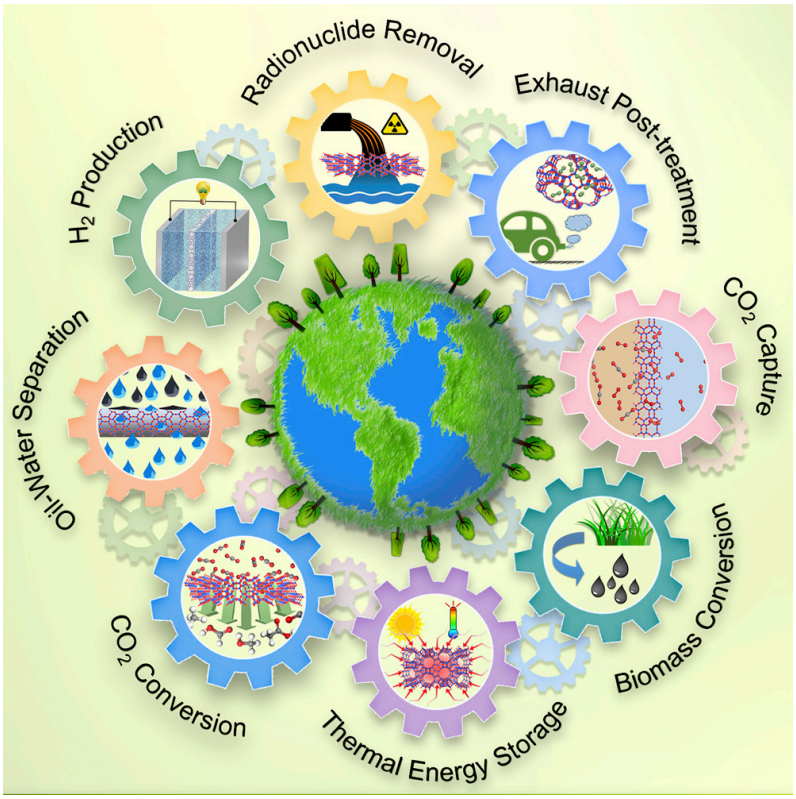

Figure 1.1 Applications of inorganic porous materials for a sustainable chemistry

1.2. Zeolites

Zeolites, also called molecular sieves, are a family of aluminosilicate materials consisting of orderly distributed micropores in molecular dimensions. They have been widely used as highly efficient catalysts, adsorbents and ion exchangers in petrochemical industries and in our daily life. Beyond these traditional applications, research on zeolites has been focused on their role in many sustainable processes. In particular, zeolites have found promising applications in the fields of renewable energy and environmental improvement such as biomass conversion, fuel cells, thermal energy storage, CO_2 capture

and conversion, air pollution remediation, water purification, etc. These applications make zeolites potential candidates as solutions to the sustainability issues in our society. The frameworks of zeolites are built from the connections of corner-sharing TO_4 tetrahedra ("T" denotes tetrahedrally coordinated Si, Al, etc.), and different ways of tetrahedra connection lead to a diversity of zeolite framework types based on various compositions. To date, 242 distinct framework types have been identified in natural or synthetic zeolites, each of which has been assigned a three-letter code by the International Zeolite Association (IZA). The frameworks of the zeolites can be decomposed into rings of different sizes, which correspond to the pore-opening windows of zeolites. According to their largest pore windows, zeolites can be categorized into small-pore ($\leq$ 8-membered ring), medium ring (10-membered ring), large pore (12-membered ring) and extra-large pore (> 12-membered ring) (Fig. 1.1). The negative charges of zeolite frameworks are usually compensated by extra-frameworks are usually compensated by extra-framework mono- or di-valent cations, which can be exchanged by other cations.

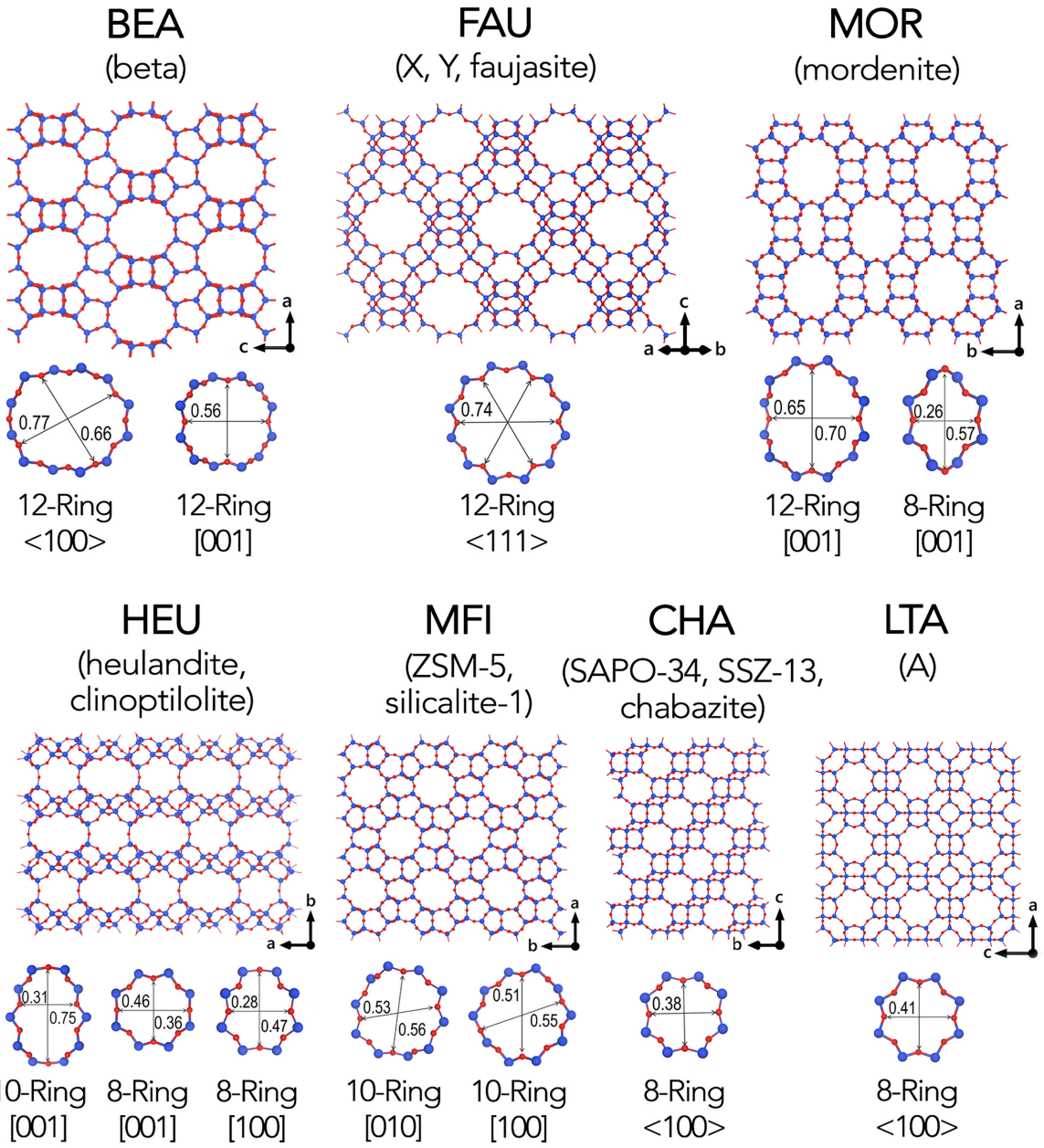

Figure 1.2 Selected widely used zeolite framework types. For each framework type, the three-letter code assigned by the International Zeolite Association (IZA), the names of zeolites belonging to the corresponding framework type, the ball stick atomic model and the pore windows are given.[1]

Many zeolites can be made using only inorganic reactants, and all the phases studied up to 1961 (such as the classical synthetic zeolites A, X and Y) were synthesized

in this manner.[3] However, in the 1960s, increasing use was made of organic compounds, particularly quaternary ammonium salts. These are often referred to as templates/ organic structure directing agents (OSDAs), since the zeolite structure appears to form around them, in some cases encapsulating them with a very close fit between the organic groups and the pore walls. The steric requirement limits the number of organic units which can be accommodated. Quaternary salts, which also act as charge balancing cations, impose a restriction on the zeolite framework charge density, resulting in products of increased Si/Al ratio. Most high-silica zeolites (Si/Al > 10) are synthesizing using organic templates, which have to be removed from the structure (usually using calcination) to produce open pore materials that can be used in separation and catalysis. For high silica zeolites, synthesis temperatures are in 100-200°C can synthesis times are often hours to days.

Later, methods to synthesize mesoporous/ hierarchical zeolites were developed using long-chain surfactant molecules as templates.[4] From 1950 up to 1978, nearly all zeolite syntheses had shared a similar chemistry in which hydroxide ion acted as a mineralizer in high pH hydrothermal conversions. In 1978, the use of fluoride ion was demonstrated in the synthesis of zeolite silicalite. This procedure later came to great prominence, particularly in the synthesis of large crystals, novel structures and heterosubstituted materials.

However, hydrothermal synthesis of zeolites is not a green process. It involves the use of organic templates, the high temperature combustion of which produces hazardous (NO_x) as well as greenhouse gases (CO_2). Conventional hydrothermal synthesis involves heating the reaction mixture (100-200 °C) in a poly(tetrafluorethylene) (PTFE) lined steel autoclave at high autogenous pressure of solvent (mainly water) for a period of time. The

safety of the equipment is always of concern due to this high autogenous pressure. These syntheses also take long times (1-20 days) even at high temperatures (100-200 °C), which is considered a high energy cost process. The large amounts of water used as a solvent leads to safety and environmental issues like generation of large amounts of contaminated water, dissolution of silica-based species in alkaline media and lower zeolite yields.

To overcome the above disadvantages of conventional zeolite preparation processes, alternative routes for synthesizing zeolites in a green or sustainable manner have been sought.[5] Recent important advances in the synthesis of zeolites are focused on the following: (a) use of recyclable, low-cost, and degradable templates for synthesis, (b) oragnotemplate-free zeolite synthesis, (c) ionothermal zeolite synthesis, using ionic liquids as solvent, (d) dry-gel conversion and vapor-phase transport method for synthesis, using negligible amount of solvent (water), (e) solvent-free zeolite synthesis starting from solid raw materials, and (f) microwave assisted zeolite synthesis resulting in low energy consumption. Fundamentally understanding the role of solvent (water) and autogenous pressure in the synthesis of zeolites can open up an avenue to synthesis zeolites in an environmentally friendly and cost-effective manner.

Apart from the shape-selective catalytic properties offered by zeolites resulting into their wide use in industry, zeolites can also act as molecular sieves due to their well-ordered micropores. Inorganic membranes, particularly zeolite membranes are of interest because not only can they withstand high temperatures and pressures, but also offer high selectivity and can replace energy-intensive separation methods currently in use.[6] Some recent industrial projects use zeolite membranes, such as for ethanol dehydration, but so far these projects have been limited. A major constraint has been the low flux and high cost, which

make the required membrane area economically unviable.[7] Therefore, research needs to be directed towards developing facile methods to achieve an order of magnitude reduction in zeolite membrane thickness.

1.3. Mesoporous carbons

Another important inorganic porous material is mesoporous carbons. They have attracted much attention during the past two decades in the fields of energy conversion and storage (Fig. 1.2) because of their advantages such as high surface area, tunable pore size, alternative pore shapes, chemical inertness, as well as optimal electroconductivity.[8,9]

Conventional porous carbon materials, such as activated carbon and carbon molecular sieves, are synthesized by pyrolysis and physical or chemical activation of organic precursors such as coal, wood, fruit shell, or polymers, at elevated temperatures. These carbon materials normally have relatively broad pore-size distributions in both micropore and mesopore ranges. Key advances in synthesizing activated microporous carbon materials include (a) use of potassium hydroxide for synthesis of supermicroporous carbon materials with surface areas as high as 3000 m^2g^{-1}, (b) selective reaction of carbides with halogen gases for generation of carbon materials with controlled microporosity. However, activated microporous carbons have the following drawbacks (a) slow mass transport of molecules because of space confinement imposed by small pore sizes, (b) low conductivity arising from the presence of enormous surface functional groups and defects, and (c) collapse of porous structures during high temperature treatment and graphitization.

Mesoporous carbons overcome many of these limitations.[8] They are synthesized using either a hard-template synthesis method or a soft-template synthesis method.[10–15]

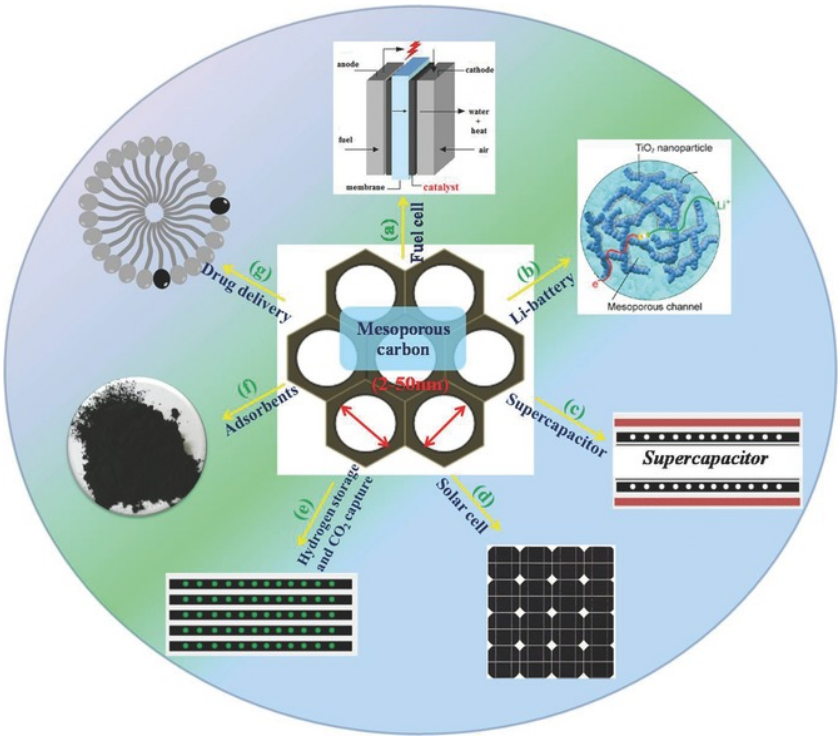

Figure 1.3 Applications of mesoporous carbon materials

In a hard-template method, the templates mainly serve as molds for replication of mesoporous carbon materials, and no significant chemical interactions take place between templates and carbon precursors. The corresponding porous structures are predetermined by the templates, which have well-defined nanostructures. This method was not accomplished until the early 1980s, when the use of spherical solid gel as a template was reported. The method involved (a) preparation of silica gel with controlled pore structure, (b) impregnation/infiltration of the silica template with monomer or polymer precursors, (c) cross-linking and carbonization of the organic precursors, and (d) dissolution of the

silica template. The space once occupied by the host silica materials is transferred into the pores of the resulting carbon materials and the carbon in the pores of the host silica now becomes the continuous carbon framework.

Ordered mesoporous carbons with graphitic pore wall structure is also gaining interest recently because of their great potential in applications such as fuel cells and double-layer capacitors. Three approaches have been used to synthesize ordered mesoporous carbons with graphitic pore walls: (a) using carbon precursors with fused aromatic structures, (b) synthesis by chemical vapor deposition (CVD) at high temperature (>900 °C), and (c) treating carbons with amorphous pore walls at temperatures over 2000 °C to induce graphitization process.

The soft-template method involves generation of nanostructures through self-assembly of organic molecules. The corresponding pore structure is determined by synthetic conditions, such as mixing ratios, solvents and temperatures. In this method, molecules or moieties are manipulated at the molecular level and spatially organized in nanospaces by hydrogen bonding, hydrophobic/hydrophilic interactions, ion pairing and/or dative interactions. The chemical interactions between templates and carbon precursors play an important role in the success of the soft-template synthesis. Amphiphilic molecules like surfactants and block copolymers have been extensively used as soft templates. There are four key requirements for the successful synthesis of mesoporous carbon materials using soft templates: (a) the ability of the precursor components to self-assemble into nanostructures, (b) the presence of at least one pore-forming component and at least one carbon-0yielding component, (c) the stability of the pore-forming component that can sustain the temperature required for curing the carbon-yielding component but can be

readily decomposed with the least carbon yield during carbonization, and (d) the ability of the carbon-yielding component to form a highly cross-linked polymeric material that can retain its nanostructure during the decomposition or extraction of the pore-forming component. So far, only a few materials meet these requirements.

Amorphous carbon materials with functional surface groups have recently received significant attention as catalysts and adsorbents in the process of hydrolysis of cellulose to glucose due to their low cost, hydrothermal stability and unique adsorption properties.[16,17] Mesoporous ordered carbon materials with graphitic pore structure can prove to be excellent candidates for this application. Tuning their surface properties and pore structure needs to be studied. Such materials can not only be used as adsorbents but also can find applications as electrodes in batteries, for hydrogen storage and as catalysts in industrial reactions.

1.4. Thesis outline

Synthesis of a three-dimensionally ordered mesoporous (3DOm) carbon from a lanthanum-embedded silica nanoparticle template and ethylene as a carbon source is described in Chapter 2. Chapter 3 describes the study of the role of water and autogenous pressure on vapor transport synthesis of silicalite-1, a zeolite with MFI framework.

Chapter 4 describes the development of a room-temperature facile method to exfoliate two-dimensional layered zeolites in liquid telechelic polybutadienes. Additionally, the interactions between the polymer and zeolite and the effects of zeolite composition on exfoliation are studied. Preparation of a thin nanosheet coating on a

sintered silica fiber support and the subsequent gel-free secondary growth of the film is described.

Chapter 5 includes conclusions and future directions for the accomplished research as a part of this thesis.

CHAPTER 2

SYNTHESIS OF MESOPOROUS CARBON FOR ADSORPTION OF SUGARS FROM MOLTEN SALT HYDRATE

2.1. Background

About 75% of the world's energy and commodity chemicals are derived from fossil fuels. However, growing economies, rising need for petroleum and decline in the fossil fuel resources makes it imperative to develop processes for sustainable production of fuels and chemicals. Lignocellulosic biomass (obtained from wood, crop residues etc.) is currently the only non-food source of organic carbon.[18,19] Lignocellulose is composed of 35-50% cellulose (a polymer of glucose), 25-30% hemicellulose (a heteropolymer of C_5 sugars) and 15-30% lignin (a large polyaromatic compound).[20] One of the key challenges in biomass conversion is saccharification of cellulose into glucose.[21,22] Cellulose consists of dense intra- and inter-chain hydrogen bonding between the anhydroglucose units (AGUs), which limit the access of both homogeneous and heterogeneous catalysts to the $\beta(1\rightarrow4)$ glycosidic bond. The supramolecular structure of cellulose also imposes significant kinetic barriers on its reactivity and contributes to its low solubility in conventional solvents. Several methods have been developed to address these challenges.[20,23,24]

Conventionally, enzymes collectively known as cellulases are employed for the hydrolysis of cellulose to glucose. The –CH groups in the axial positions of the AGUs form van der Waal bonds with the π electron cloud (termed as CH-π bonds) of the aromatic amino acid residues the enzymes. The recalcitrant glycosidic bond in the adsorbed cellulose molecule can be cleaved at an ambient temperature due to the specific chemical structure

of the enzyme. The activation energy of enzymatic hydrolysis of cellulose is 3-50 kJ/mol.[25] This process is uneconomical due to high cost of the enzymes, need for pH adjustments, and low activity. High glucose yields are obtained by using homogeneous catalysts like dilute HCl and H_2SO_4, however, the activation energy of hydrolysis is very high (170-180 kJ/mol).[26] Researchers then focused on homogeneous catalysis using dilute acids like HCl, H_2SO_4, and HF for hydrolysis. The spent acid is neutralized with a mixture of $CaO/CaSO_4$, which generates large amounts of gypsum as waste. This process also demands corrosion-resistant plants, involving high costs. Heterogeneous catalysts like solid heteropolyacids, niobic acid, MoO_3-ZrO_2, zirconium tungstates, Zr/La/Nb phosphates, Nafion resin, Amberlyst, metal oxides and zeolites offer ease of catalyst separation after hydrolysis, however the glucose yields do not exceed 40% and significant side-reactions occur.[27]

One promising method employs ionic liquids or molten salt hydrates (MSH) to dissolve crystalline cellulose, which can facilitate the cleavage of β(1→4) glycosidic linkages in cellulose structures.[28–30] A proposed mechanism for the dissolution of cellulose in ionic liquids involves interactions between the anions of ionic liquids and the hydroxyls of cellulose *via* hydrogen bonds.[31] In MSH, cations interact with the oxygen in cellulose[32] and highly electronegative halogen ions act as hydrogen-bond acceptors of -OH groups in cellulose, thus breaking the hydrogen bonds.[33,34] In general, ionic liquids are expensive and some are toxic, and require extensive organic synthesis.[35,36] Additionally, the difficulty in recycling ionic liquids also limits their commercial applications.[37,38] MSHs, like LiBr and $ZnCl_2$, prepared with water to salt molar ratio equal or less than the coordination number of the cations are effective in cellulose hydrolysis.[28,29] More than 90% glucose yield is obtained from cellulose hydrolysis in MSH at 85 °C, especially when a small fraction of

an inorganic acid is added.[28,39] Compared to ionic liquids, MSH has a simple structure, is easy to synthesize and can be used under a wide range of operating conditions.

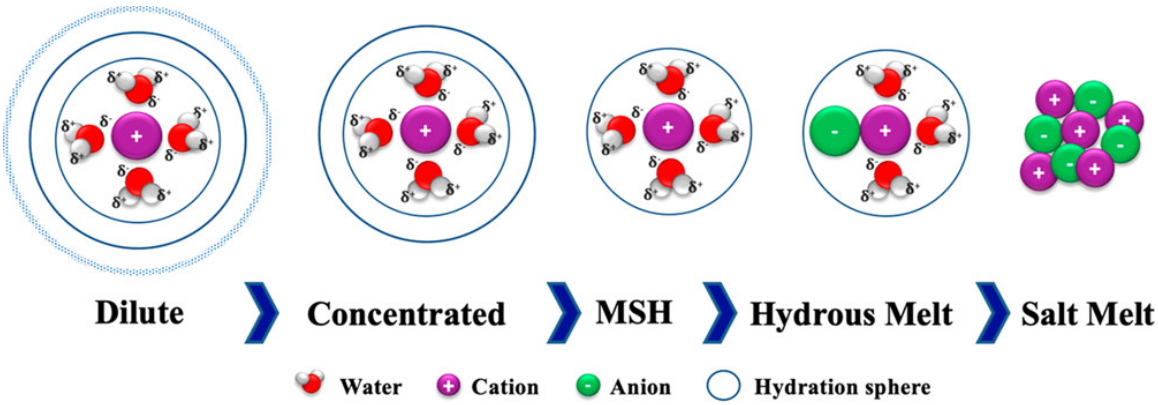

Figure 2.1 Graphical depiction of ion-water and ion-ion interactions in the inner hydration sphere of a lithium cation with changing salt concentration. In MSHs, there is only one hydration layer around the cation.[40]

Despite its promising potential for cellulose hydrolysis, there are still several challenges in its use. Economical separation of the produced sugar from the hydrolysate is a challenge due to the high solubility of sugars in MSH.[28,41] The primary solvation shell around the glucose ring consists predominantly of halogen anions which bind to the hydroxyl groups of glucose by hydrogen bonds, making separation of glucose difficult.[42] In order to address the separation issue, a biphasic reaction system is often used to convert glucose to 5-hydroxymethylfurfuryl (HMF) in MSH with parallel extraction of HMF to an organic phase.[39,43,44] However, direct separation of sugars from MSH without converting them into other chemicals is still highly desired because of their value and additional conversion pathways that sugars provide.

Amorphous carbon materials with functional surface groups have recently received significant attention as catalysts and adsorbents for the aqueous phase hydrolysis of cellulose to glucose due to their low cost, hydrothermal stability and unique adsorption

properties.[45–47] Amorphous carbons are composed of polycyclic aromatic domains in irregular arrangements. The surface of the organic carbon may also contain a large variety of oxygen-containing groups, which can tune the carbon surface properties from hydrophobic to hydrophilic.[48,49] β(1→4) glucan oligomers contain -CH groups in the axial plane. Interactions between β(1→4) glucan oligomers and amorphous carbon are dominated by CH-π bonds.[50–53] The adsorption of glucan oligomers on carbons is both enthalpically and entropically driven, and is controlled by the interaction between the glucan and the carbon surface as well as the number of water molecules being released per AGU.

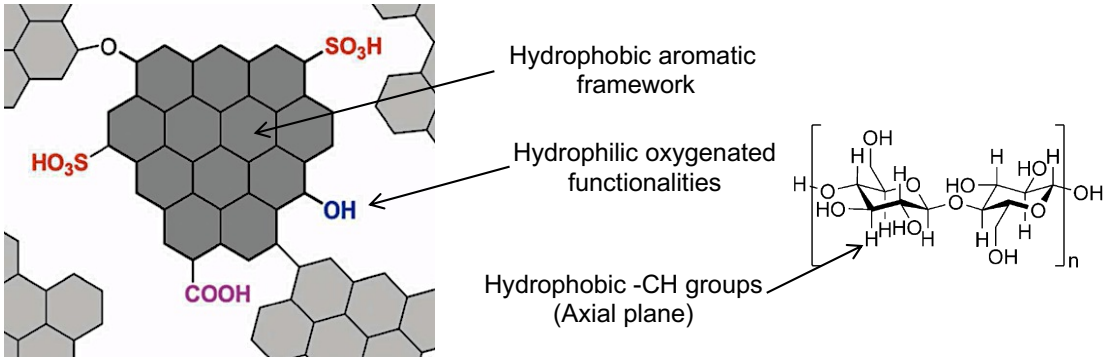

Figure 2.2 Graphical depiction of amorphous carbon with hydrophobic polycyclic aromatic domains and β(1→4) glucan with -CH groups in the axial plane.

The adsorption enthalpy and entropy are determined by several parameters including the hydrophobicity, mesopore/ micropore size, surface functional groups and adsorbed molecules. A large polycyclic aromatic domain and a hydrophobic surface might lead to strong adsorption of glucan oligomers with regard to both enthalpy and entropy aspects. Three-dimensional graphene architectures with periodic mesopores are of topical interest because of the possibility of combining the characteristics of graphene with a three-

dimensional porous structure. A three-dimensionally ordered mesoporous carbon (3DOm carbon) has showed a promising potential for the adsorption of glucan oligomers.[54–56] 3DOm carbon is synthesized by replication of colloidal crystals composed of size-tunable silica nanoparticles, using furfuryl alcohol as the carbon source. We hypothesized that a 3DOm carbon with graphitic pore walls (sp^2 carbon structure) can be synthesized by selectively controlling the deposition of carbon on a colloidal silica nanoparticle template. Such a graphitic 3DOm carbon can provide a large polycyclic aromatic domain size for increasing glucan adsorption from MSH. Recently, a microporous 3D-graphene like carbon was synthesized using zeolite FAU as the template and ethylene as the carbon source.[57–62] Lanthanum (La^{3+}) ions embedded in the zeolite framework acted as a catalyst to facilitate selective deposition of carbon inside the zeolite pores without external carbon deposition.[59] A transition metal element like lanthanum bonds with olefins through a d-π coordination. The d-π interactions stabilize ethylene and the pyrocondensation intermediates to from a carbon framework selectively in the zeolite pores. We hypothesized that the synthesis of a graphitic 3DOm carbon can be achieved by embedding the colloidal silica nanoparticle template with La^{3+} ions and using ethylene as a carbon source.

In this work, the effect of LiBr molten salt hydrate (MSH) concentration on adsorption of glucose on amorphous carbons was studied. Additionally, we attempted the synthesis of graphitic 3DOm carbon using lanthanum-embedded colloidal silica nanoparticle template and ethylene as the carbon source.

2.2. Experimental details

2.2.1. Materials

Glucose (99%), lithium bromide (LiBr, 99%), tetraethyl orthosilicate (TEOS, 98%), furfural alcohol (98%) and lanthanum (III) nitrate hexahydrate (99%) were purchased from Alfa Aesar. Oxalic acid (99%) and L-lysine (98%) were purchased from Sigma Aldrich. Hydrogen peroxide (31.4%) was purchased from Fisher Scientific. Ethylene (ultra high purity) was purchased from Airgas. Powdered activated carbon Norit SX Ultra activated carbon was purchased from Japan EnviroChemicals. Black Pearls 2000 (BP2000) carbon black was purchased from Cabot Ltd.

2.2.2. Adsorption of glucose

The carbon samples were dried at 100 °C for 24 h before using for adsorption. Due to poor dispersion of BP2000 carbon black in the MSH, the carbon was treated with H_2O_2 to introduce oxygen-containing groups on the surface. 1 g of BP2000 was added into a 50 mL centrifuge tube with 20 g of 31.4 wt% H_2O_2. The mixture was stirred at room temperature for 12 h. The obtained sample was then washed with deionized water until the pH of the supernatant was neutral. The sample was called ox-BP2000. BP2000 and ox-BP2000 were characterized by an X-ray photoelectron spectrometer (Thermo-Fisher, equipped with a monochromatic Al Kα X-ray source with 400 μm spot size).

For glucose adsorption, glucose solutions were prepared with LiBr concentrations of 0 wt%, 10 wt%, 30 wt% and 60 wt%. The initial substrate concentration was varied from 1 mg mL^{-1} to 120 mg mL^{-1}. For adsorption 10-40 mg of adsorbent was added into a 5 mL glass vial (Fisher Scientific), containing 2 mL of glucose solution. The contents of the vial were stirred at 750 rpm for 12 h. After adsorption, the liquid phase was separated from the

solid adsorbent by centrifugation at 6000 rpm. The liquid was diluted 10 times with deionized water before analysis using high performance liquid chromatography (HPLC). The HPLC (LC-20AT, Shimadzu) was equipped with a refractive index (RID-10A) detector. A Bio-Rad HPX-87H (300 mm × 7.8 mm) column with a guard column was used. 0.005 M sulfuric acid was used as the mobile phase with a flow rate of 0.6 mL min^{-1}. The adsorption capacity was calculated using the following equation:

$$\text{Glucose adsorbed} = \frac{(M_{GI} - M_{GF})}{M_A} \times 100\ \%$$

where M_A is the amount of adsorbent; M_{GI} is the amount of glucose in the solution before adsorption and M_{GF} is the equilibrium amount of glucose in the solution after adsorption.

2.2.3. Synthesis of 3DOm (Fur) carbon

3DOm (*Fur*) carbon was synthesized according to a reported procedure.[54] 35 nm silica nanoparticles were prepared by mixing 0.198 g L-lysine, 13.3 g TEOS, and 180 g water at 90 °C in a Teflon bottle, stirring at 1000 rpm. An additional amount of 26.6 g of TEOS was added after 24 h, and an additional 26.6 g of TEOS was added after 48 h. The solution was stirred for an additional 24 h after the last addition of TEOS. The resulting solution was evaporated in a convection oven at 70 °C for 72 h to remove water. The precipitated SNPs were calcined for 24 h at 600 °C (with 3 °C min^{-1} ramp rate) in air, to remove L-lysine.

To prepare the resin, 0.08 g oxalic acid was dissolved in 16 g furfuryl alcohol. The SNPs were impregnated with furfuryl alcohol solution by incipient wetness. Excess furfuryl alcohol solution was removed with a filter paper. The sample was then put in a 70

°C oven for 72 h and subsequently carbonized under nitrogen at 200 °C for 3 h, followed by 850 °C for 4 h (1 °C min^{-1} ramp rate). 3 g of the sample was then added to 35 g of 6 M KOH solution and heated at 180 °C for 2 days, to remove silica. This process was repeated twice. Finally, the carbon was repeatedly washed in 1 L of DI water at 70 °C for 3 h, until the pH of the solution fell below 8. The resulting 3DOm (*Fur*) carbon was dried in a 70 °C oven for 24 h.

2.2.4. Synthesis of 3DOm (Eth) carbon

35 nm silica nanoparticles were embedded with La^{3+} ions by incipient wetness. 0.35 mL of 0.1 M $La(NO_3)_3$ solution was added to 1 g of SNPs and the excess solution was removed using a filter paper. The sample was then dried overnight in a 70 ° C oven to obtain La-SNPs. To synthesize 3DOm (*Eth*), 0.15 g of La-SNPs were loaded into a quartz fixed-bed reactor and placed into a proportional integral derivative (PID) controlled furnace. The furnace was heated to 750 °C under helium flow. The flow was then switched to ethylene at 35 mL min^{-1} for 3 h. The temperature was then raised to 850 °C and the flow was switched to helium at 40 mL min^{-1}. The reactor was then cooled under helium flow. The sample was then washed with 6 M KOH solution and heated at 180 °C for 2 days, to remove silica. The carbon was then washed with DI water. The resulting 3DOm (*Eth*) carbon was dried in a 70 °C oven for 24 h.

2.2.5. Characterization

Small-angle X-ray scattering (SAXS) data was obtained using a SAXSLAB's Ganesha instrument with a Cu-Kα radiation source at a constant sample-to-detector

distance of 441 mm. Scanning electron microscope (SEM) images were collected suing FEI Magellan 400 XHR-SEM operated at 3.0 kV. Thermogravimetric analysis (TGA) was performed using TA instruments SDT 600 instrument. Samples (0.02-0.03 g) were placed in an alumina crucible and heated with a ramping rate of 10 K/min in a stream of dry air (Airgas). Raman spectra were measured on DXR Raman microscope (Thermo Scientific) with a laser wavelength of 780 nm and spot size of 3.1 μm. Nitrogen adsorption and desorption isotherms were measured at 77 K on an automated gas sorption analyzer (Autosorb iQ2, Quantachrome) after degassing at 300 °C under vacuum.

2.3. Results and discussion

2.3.1. Surface functionalization of BP2000

Carbon black BP2000 has been used as an adsorbent for sugars due to its high surface area and microporosity.[63–65] However, it exhibits poor dispersion in MSH due to its hydrophobicity. While the dispersion of BP2000 can be improved by introducing hydrophilic oxygenated functionalities, it is important to preserve its polycyclic aromatic domains, which play an important role in adsorption by forming CH-π bonds with the sugar molecule. Treatment with hydrogen peroxide was found to be an efficient way to introduce weak oxygenated functionalities in a carbon material.[66–68]

The XPS results of BP2000 before and after oxidation are shown in Fig. 2.4 and the elemental distribution of the materials is shown in Table 2.1. The data indicates that the oxygenated functionalities on the surface of carbon are increased after treatment with hydrogen peroxide. The increased peaks at 285.6 eV and 286.5 eV are assigned to C-O bonds.[69] The 288.6 eV peak is attributed to the C=O species.[69,70] The elemental distribution

indicates a small increase in the oxygen percentage of the material after oxidation, which could enhance its hydrophilicity and dispersion in MSH. More importantly, there is no obvious change of the peak shape at other abscissas in the XPS spectra, indicating that hydrogen peroxide causes negligible change in the polycyclic aromatic domains of carbon.

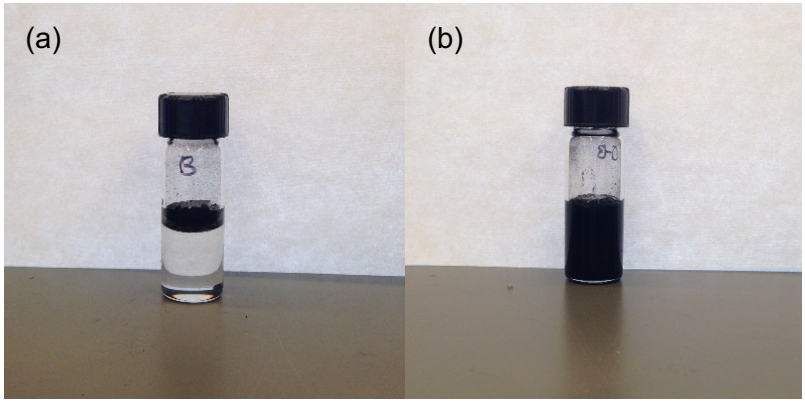

Figure 2.3 (a) BP2000 exhibits poor dispersion in 30 wt% LiBr (b) ox-BP2000 (BP2000 after oxidation with hydrogen peroxide) exhibits good dispersion in 30 wt% LiBr.

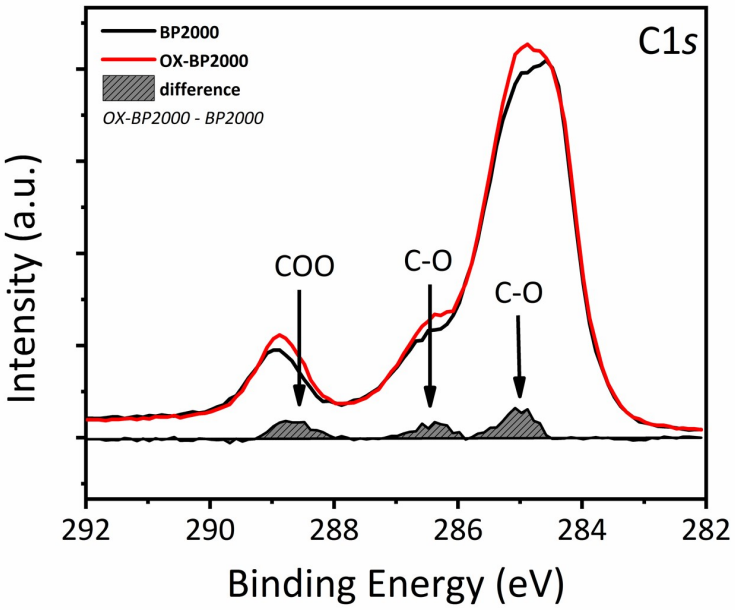

Figure 2.4 Normalized C1s XPS spectra of BP2000 and ox-BP2000 (BP2000 after oxidation with H_2O_2). The difference in the two spectra is calculated by subtracting the BP2000 spectrum from the ox-BP2000 spectrum.

Table 2.1: Elemental composition of BP2000 and ox-BP2000

Materials	C%	O%
BP2000	86.42	13.58
ox-BP2000	85.05	14.95

2.3.2. Glucose adsorption on carbon materials

The surface areas of BP2000, ox-BP2000 and Norit SX Ultra are calculated from their nitrogen adsorption/desorption isotherms. The data is presented in Table 2.2.

Table 2.2 Textural properties of carbon materials measured from nitrogen adsorption/desorption isotherms

Carbon	S_{BET}[a]	S_{micro}[b]	$S_{external}$[b]	V_{micro}[b]

BP2000	1342	339	1003	0.189
ox-BP2000	1336	342	994	0.189
Norit SX Ultra	868	378	490	0.200

[a] Surface area (S_{BET}) was calculated by the Brunauer-Emmett-Teller (BET) isotherm method
[b]Micropore volume (S_{micro}), external surface area ($S_{external}$) and micropores volume (V_{micro}) were calculated according to the *t*-plot method

Glucose adsorption isotherms on Norit SX Ultra and ox-BP2000 were measured at different LiBr concentrations at room temperature (298 K), presented in Fig. 2.5. Activated carbon Norit SX Ultra exhibited lower adsorption capacities than ox-BP2000. The surface area of the former is also much lower than that of the latter. This result indicates that the adsorption capacity of the adsorbents is related to their surface areas.

Three adsorption isotherm models (Langmuir, Freundlich and Redlich-Peterson) were employed to fit the data. The adsorption model equations are presented in Table 2.3. The fitted parameters are listed in Tables 2.4 and 2.5. Since the Redlich-Peterson gives the highest R^2 value, it was chosen to fit and obtain the parameters for glucose adsorption on Norit SX Ultra and ox-BP2000. The results demonstrate that increase in LiBr MSH concentration has a negative effect on adsorption capacity. This might be due to adsorption of salt ions on the adsorption sites leading to reduction in the adsorption capacity.

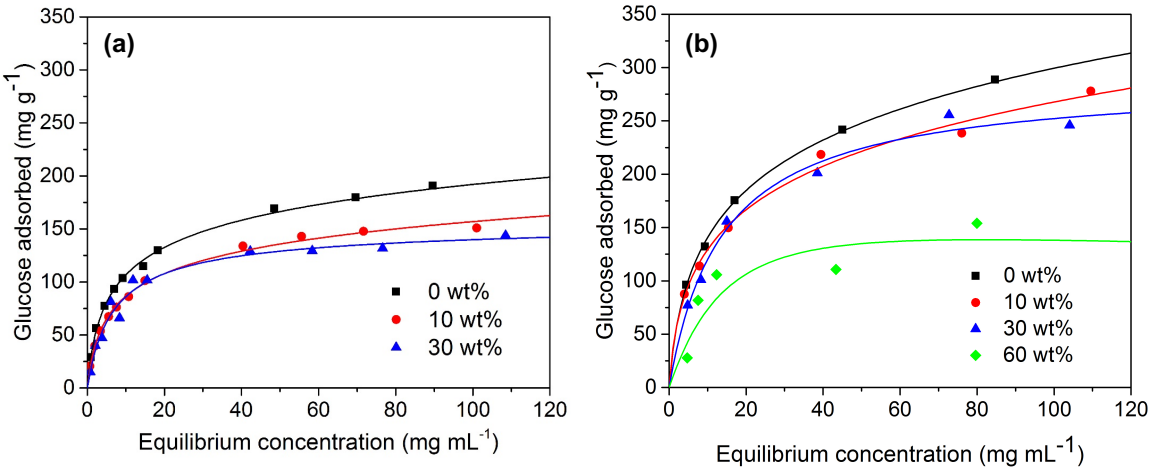

Figure 2.5 Adsorption isotherms of glucose on (a) Norit SX Ultra and (b) ox-BP2000 from LiBr MSH with various concentrations (0-60 wt%) at 298 K. The points are from experimental measurements. The lines are from Redlich-Peterson model fitting.

Table 2.3 Adsorption isotherm models used to fit the adsorption data

Adsorption isotherm model	Mathematical formula[a]
Langmuir	$Q = \frac{Q_{mL} K_L C_e}{1 + K_L C_e}$
Freundlich	$Q = K_F C_e^{1/n_F}$
Redlich-Peterson	$Q = \frac{K_{RP} C_e}{1 + b_{RP} C_e^{n_{RP}}}$

[a] Q is the adsorption loading of the solute, and C_e is the concentration of the solute in the liquid in equilibrium with the solid

Table 2.4 Adsorption isotherm parameters (Langmuir and Freundlich models) for glucose adsorption measured at 298 K

		Langmuir			Freundlich		
Carbon	LiBr (wt%)	Q_{mL} (mg g^{-1})	K_L (mL mg^{-1})	R_L^2	K_F	n_F	R_F^2
ox-BP200	0	329.6	0.0758	0.9813	62.13	0.3443	0.9877
ox-BP200	10	283.9	0.0885	0.9685	57.83	0.3369	0.9821
ox-BP200	30	287.3	0.0723	0.9833	49.41	0.3668	0.9357
ox-BP200	60	171.52	0.0698	0.7865	22.78	0.4408	0.7149
Norit Ultra	0	195.8	0.1370	0.9751	44.51	0.3281	0.9571
Norit Ultra	10	156.5	0.1441	0.9869	33.92	0.3510	0.9439
Norit Ultra	30	147.3	0.1452	0.9712	30.83	0.3562	0.8642

Table 2.5 Adsorption isotherm parameters (Redlich-Peterson model) for glucose adsorption measured at 298 K

		Redlich-Peterson			
Carbon	LiBr (wt%)	K_{RP} (mL mg^{-1})	b_{RP}	n_{RP}	R_{RP}^2
ox-BP2000	0	49.62	0.4101	0.7891	0.9993
ox-BP2000	10	58.33	0.5932	0.7723	0.9886
ox-BP2000	30	20.89	0.0751	0.9929	0.9832
ox-BP2000	60	10.35	0.0264	1.1950	0.7824
Norit Ultra	0	46.33	0.4842	0.8392	0.9969
Norit Ultra	10	36.85	0.4719	0.8388	0.9951

Norit Ultra	30	23.14	0.1833	0.9643	0.9743

2.3.3. Synthesis of three-dimensionally ordered mesoporous (3DOm) carbons

3DOm (Fur) carbon is synthesized by following a procedure reported in the literature.[54] Colloidal 35 nm silica nanoparticles are used as a template and furfuryl alcohol is used as the carbon source, as shown in Fig. 2.6. 3DOm (Eth) is synthesized using lanthanum-embedded silica nanoparticles as the template and ethylene as a carbon source. Lanthanum can act as a catalyst and facilitate selective deposition of carbon by forming d-π coordination with ethylene.[59] Carbon deposition was carried out in a quartz fixed bed reactor placed into a PID controlled furnace. The amount of carbon deposited per unit weight of the sample was determined by thermogravimetric analysis (TGA). The TGA data of samples (before washing with KOH to remove the silica template) synthesized at various operating conditions are shown in Fig. 2.7. The final weight loss at 800 °C in the TGA data represents the amount of carbon deposited as a percentage of the weight of the sample. Deposition at operating conditions of 750 °C and 3 h, yielded a carbon that could retain the structure after the silica template was removed by KOH washing. Therefore, these conditions were used as the optimum conditions for 3DOm (*Eth*) synthesis.

The SAXS patterns of the two carbon samples (after washing with KOH) and the SNPs shown in Fig. 2.8. indicate that the peaks corresponding to 3DOm (*Fur*) shifted to a slightly higher angle compared to the peaks of La-SNPs. This suggests that there is a shrinkage of framework during the carbonization process. On the other hand, 3DOm (*Eth*) exhibits an exact replication of the SNP template. TGA on the two carbon samples (before removing the silica template with KOH washing) indicates that the amount of carbon

deposited per unit weight is higher for 3DOm (*Eth*) is higher than 3DOm (*Fur*). This suggests that 3DOm (*Eth*) is much denser than 3DOm *(Fur*).

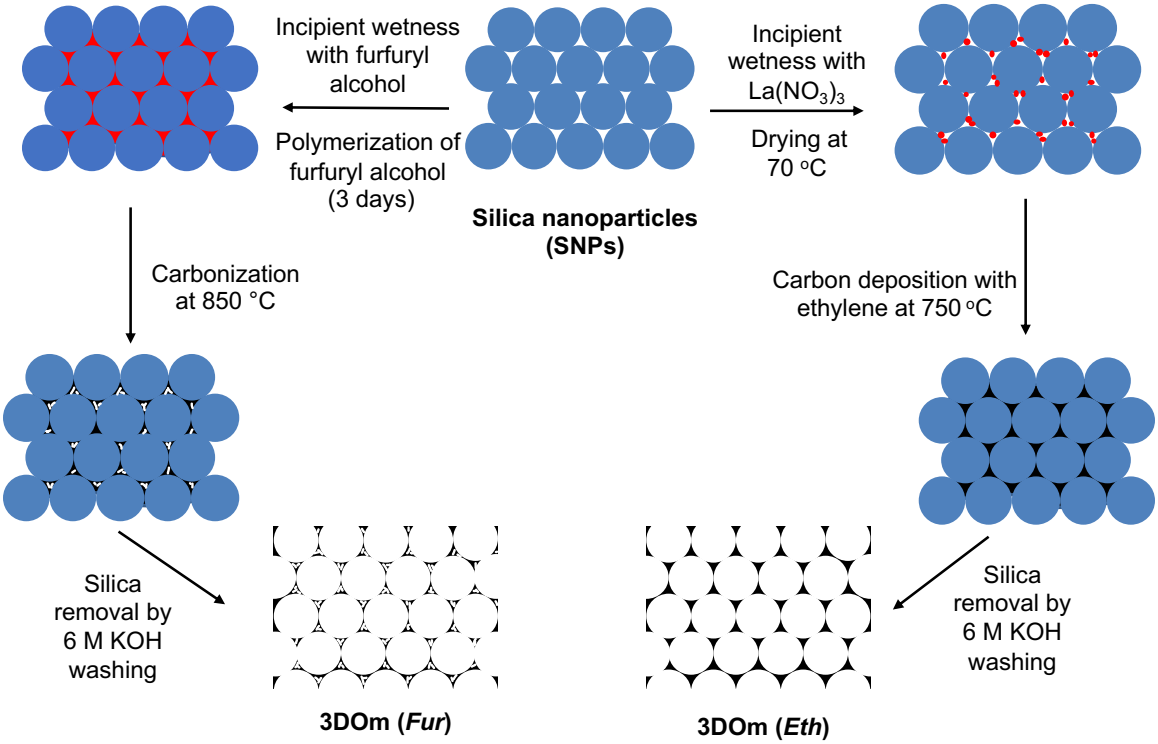

Figure 2.6 Graphical depiction of synthesis of 3DOm carbons. 3DOm (Fur) is synthesized using SNPs as the template and furfuryl alcohol as the carbon source.

3DOm (Eth) is synthesized using lanthanum-embedded SNPs as the template and ethylene as the carbon source.

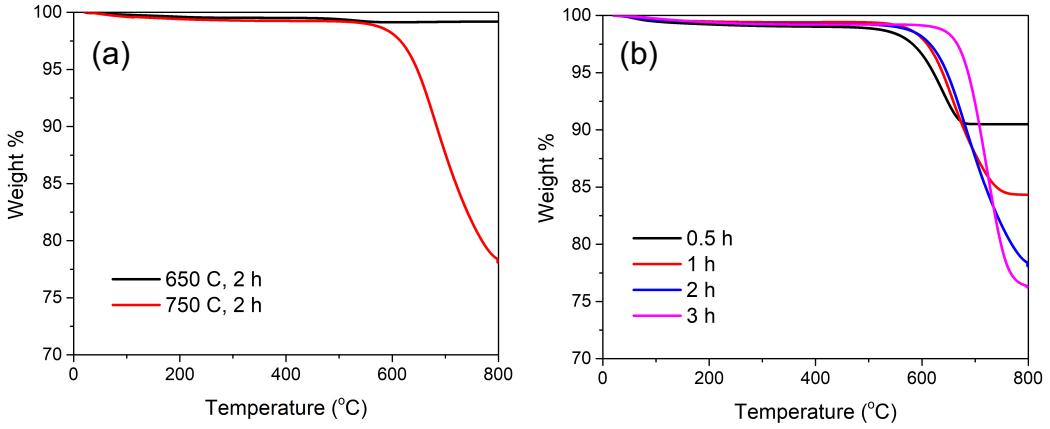

Figure 2.7 Thermogravimetric analysis (TGA) on 3DOm (Eth) samples (before washing with KOH) synthesized with ethylene flow (a) for 2 hours at 650 °C and 750 °C and (b) for various times 0.5-3 h at 750 °C

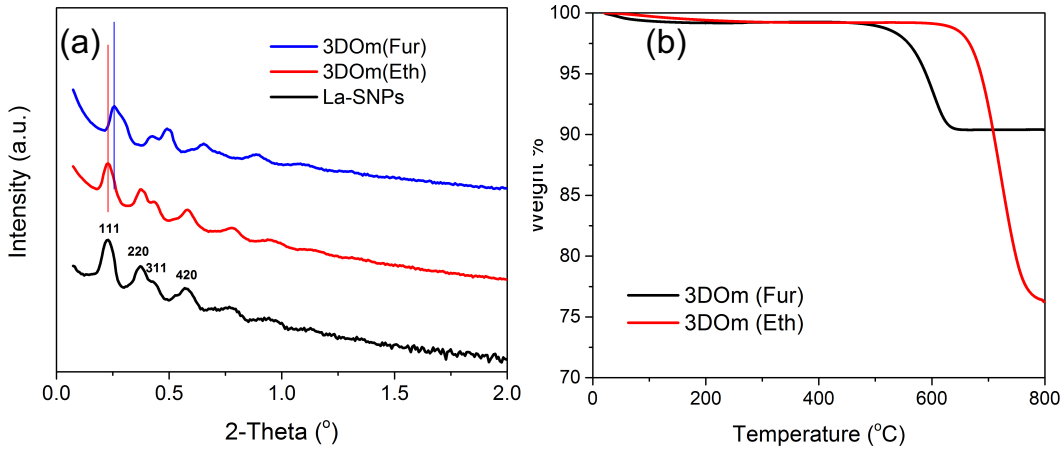

Figure 2.8 (a) Small angle X-ray scattering (SAXS) pattern of lanthanum-embedded SNPs, 3DOm (Eth) and 3DOm (Fur) after washing with KOH, and (b) Thermogravimetric analysis (TGA) on 3DOm (Fur) and 3DOm (Eth) before removing the silica template with KOH washing

The textural properties of the two carbon samples were characterized using nitrogen physisorption at 77 K and are shown in Fig. 2.9. Pore size distribution was calculated using

the Quenched Solid Density Functional Theory (QSDFT) cylindrical/ split pore adsorption branch model.[71–73] The BET surface area and micropore volume are calculated from the nitrogen physisorption isotherms and are listed in Table 2.6. The results indicate that 3DOm (*Fur*) has higher micropore volume per unit weight of carbon as compared to 3DOm (*Eth*). 3DOm (*Eth*) exhibits high mesoporosity and negligible micropores. This can be attributed to the difference in the method of carbon deposition between the two carbons. In the case of 3DOm (*Fur*), furfuryl alcohol occupies the void space in the SNPs through incipient wetness. In the process of carbonization of polymerized furfuryl alcohol, micropores form in the resulting carbon. On the other hand, deposition of carbon happens layer-by-layer on the surface of lanthanum-embedded silica nanoparticles, through carbonization of ethylene. This results in a much denser carbon with negligible micropores. This difference in the morphology is also visible in the SEM images of the two carbon materials shown in Fig. 2.10.

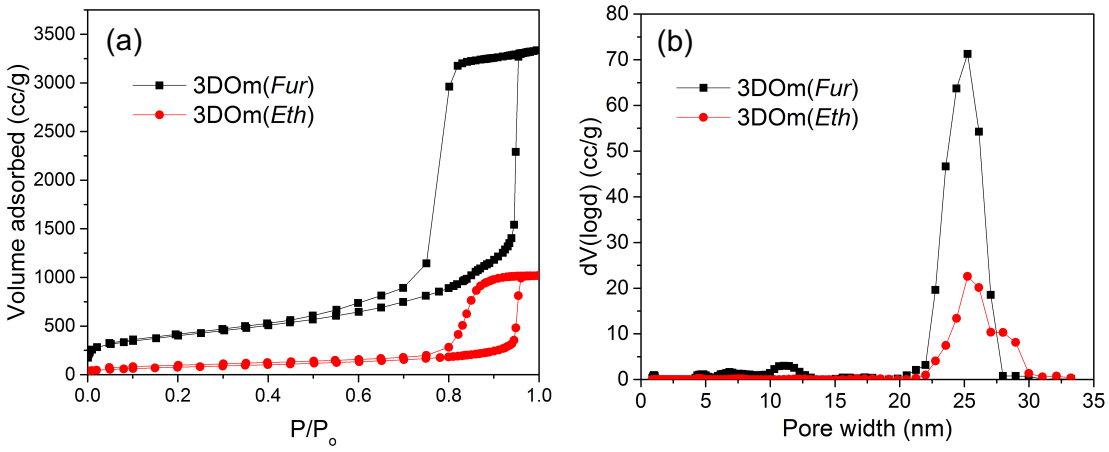

Figure 2.9 (a) Nitrogen physisorption isotherms (at 77 K) of 3DOm (Fur) and 3DOm (Eth), and (b) Pore size distribution calculated by QSDFT cylindrical/ split pore adsorption branch model

Table 2.6 Textural properties of 3DOm (Fur) and 3DOm (Eth) calculated from their nitrogen physisorption isotherms

	3DOm (*Fur*)	3DOm (*Eth*)
BET surface area ($m^2 g^{-1}$)	1417	282
Micropore volume ($cm^3 g^{-1}$)	0.095	0
Total pore volume ($cm^3 g^{-1}$)	5.11	1.53

It has been known that the first order sp^2 vibration bonds of carbon materials occur in the region of 1100 to 1800 cm^{-1}.[74–76] An undisturbed graphitic lattice exhibits one first order band at around 1580 cm^{-1}. This band is known as the G or "graphitic" band, and it corresponds to lattice vibration modes with the E_{2g} symmetry. The spectrum of the graphitic lamella exhibits an additional first order band at around 1360 cm^{-1}. This band is known as the D1 or "defect" band, which corresponds to the atoms on the edge of the graphitic lattice with vibration modes of the A_{1g} symmetry. The ratio of the peak areas of D1 and G peaks, denoted as I_D and I_G respectively, gives an estimate of the defects in the graphitic lattice. A higher I_D/I_G ratio indicates more defects. The Raman spectrum of an amorphous carbon is more complex than that of pure graphene substrates. There are several other types of vibrations from the defects (called D2, D3 and D4). The D2, D3 and D4 peaks for an amorphous carbon are located at 1559-1628, 1489-1545 and 1127-1208 cm^{-1}, respectively.[75] Peak deconvolution of the Raman spectra of 3DOm (*Fur*) and 3DOm (*Eth*) was done using Origin Pro software. The Raman spectra are shown in Fig. 2.11. The I_D/I_G ratios of 3DOm (*Fur*) and 3DOm (*Eth*) were calculated to be 3.77 and 2.96 respectively. Slightly lower ratio for 3DOm (*Eth*) indicates lower defects than 3DOm (*Fur*).

Glucose adsorption isotherms on 3DOm (*Eth*) was not measured in our study due to the low yield of the carbon material. Bulk carbon material can be synthesized using a larger reactor and adsorption isotherms can be measured in future.

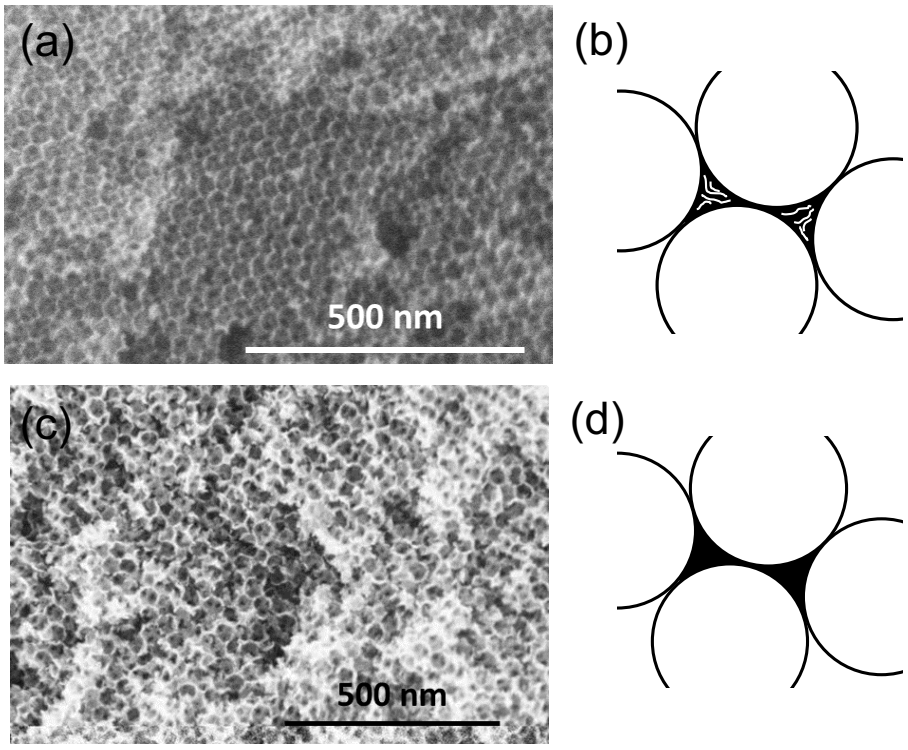

Figure 2.10: (a), (c): SEM images of 3DOm (*Fur*) and 3DOm (*Eth*) respectively, and (b), (d): schematic depiction of the proposed morphology of 3DOm (*Fur*) and 3DOm (*Eth*) respectively. 3DOm (*Fur*) shows presence of significant micropores. 3DOm (*Eth*) is denser, and has negligible micropores.

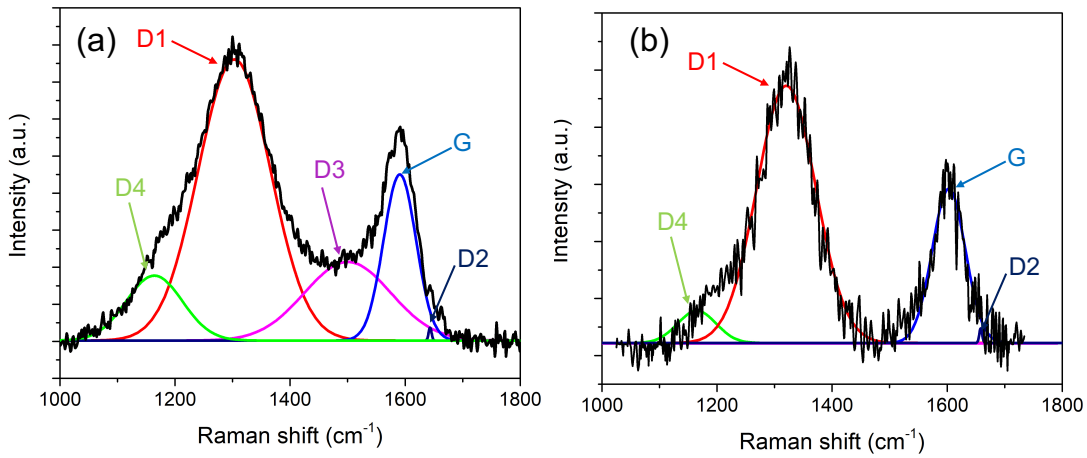

Figure 2.11 Raman spectrum of (a) 3DOm (*Fur*), and (b) 3DOm (*Eth*)

2.4. Conclusions

In summary, adsorption of glucose on Norit SX Ultra activated carbon and ox-BP2000 carbon black in presence of LiBr molten salt hydrate was studied. The results indicated that the adsorption capacity was dependent on the surface area of the carbon material. Increase in LiBr MSH concentration has a negative effect on adsorption capacity. This might be due to adsorption of salt ions on the adsorption sites leading to reduction in the adsorption capacity. A three-dimensionally ordered mesoporous carbon (3DOm (*Eth*)) was synthesized using lanthanum-embedded silica nanoparticles as the template and ethylene as the carbon source. Its textural properties and carbon structure were compared with 3DOm (*Fur*) carbon synthesized conventionally with furfuryl alcohol as the carbon source. The results indicated that 3DOm (*Eth*) is denser, more graphitic and has negligible micropores as compared to 3DOm (*Fur*).

CHAPTER 3

SYNTHESIS OF ZEOLITES BY VAPOR PHASE TRANSPORT METHOD: ROLE OF WATER AND AUTOGENOUS PRESSURE

3.1. Background

Zeolites have been widely used in the energy industry for catalysis as well as separation applications.[77–79] They are normally synthesized under hydrothermal conditions in a sealed autoclave, which involves the use of a large amount of water as a solvent. This typically leads to safety and environmental issues like generation of large amounts of contaminated water, dissolution of silica-based species in alkaline media and lower zeolite yields. In addition to these syntheses require high autogenous pressure.[3,80]

Large amount of water has been long regarded as essential for the synthesis of zeolites because it facilitates efficient transport of reactants in hydrothermal synthesis.[3] Water is used in (i) the stage of depolymerization by hydration of silica species and (ii) the stage of condensation from hydrated silica species, as proposed by the following reactions:[81]

$$\mathrm{Si(OSi)_4 + nH_2O \rightarrow Si(OSi)_{(4-m)}(OH)_m} \qquad (1 \leq m \leq 4)$$

$$\mathrm{Si(OSi)_{4-m}(OH)_m \rightarrow Si(OSi)_4 + nH_2O} \qquad (1 \leq m \leq 4)$$

If the above two reactions are combined, water appears on both sides of the equation. Since water is formed in the hydration of silica species and formed again in the condensation of the hydrated species, water can be considered as a “catalyst” here. If water acts as only a catalyst in zeolite crystallization, the amount of water necessary for crystallization need not be large.

There have been many attempts to synthesize zeolites using a solvent-free route in the past years.[82] Pioneering research to challenge the essentiality of water in zeolite synthesis has been performed using dry-gel conversion (DGC) method through steam-assisted crystallization (SAC) and vapor-phase transport routes.[83–88] In the DGC method (Fig. 3.1), an aqueous solution of the OSDA, inorganic cation and silica source are aged, and then dried to form a hard cake. The cake is then using a pestle and mortar, and the obtained powder is called the 'dry gel'. The H_2O/Si ratios in the dry gel are between 0.5 to 2, which are much lesser than those in the conventional hydrothermal synthesis in alkaline medium ($10 < H_2O/Si < 1000$).[89] The crystallization is carried out by steam assisted crystallization (SAC), in which water is physically separated from the dry gel in an autoclave. At the synthesis temperatures (typically 130-175 °C), the water vaporizes and contacts with the dry gel, aiding in the crystallization of zeolites. The DGC method, therefore, cannot be considered as a solvent-less synthesis method; water is in fact necessary for a successful synthesis using this method. A large amount of water is also necessary for the preparation of the dry gel. Moreover, SAC requires a sealed autoclave and significant autogenous pressure is generated.

Besides water, other solvents, such as alcohols and ionic liquids have also been used in zeolite synthesis.[90–93] However, high costs of common ionic liquids and low yields of zeolites limit the applications of ionothermal synthesis. Ren and coworkers reported a 'solvent-free' synthesis method, where the raw materials (hydrated sodium silicate and fumed silica, plus any organic SDA and sources of heteroatoms such as Al and Fe) were first ground manually for 10-20 min, and then crystallization occurred when the solids were

heated at 180 °C for 24-48 h.[94] Using this approach, zeolites with MFI, SOD, BEA, MOR and FAU framework types, which are industrially important zeolites, were synthesized.

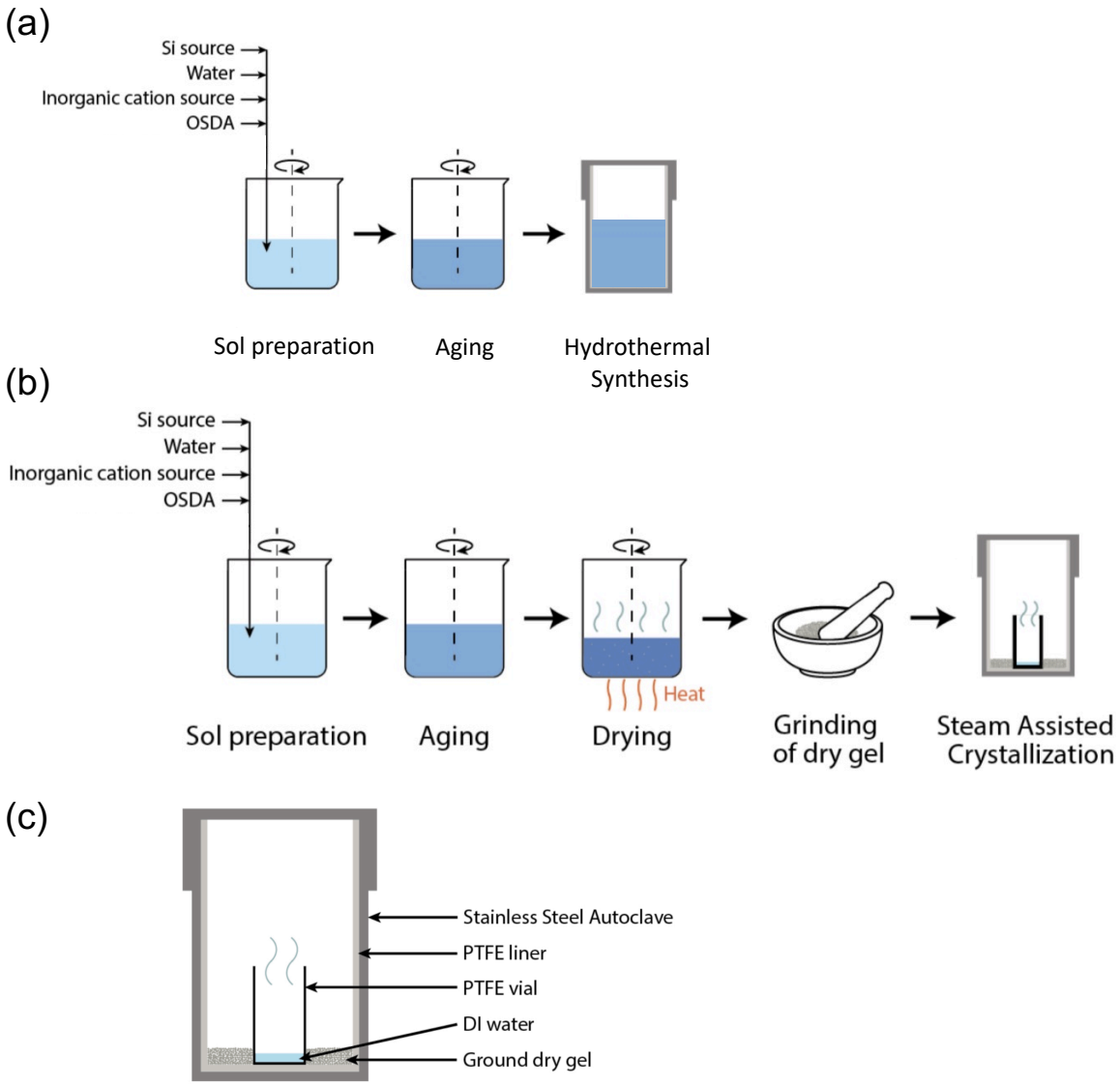

Figure 3.1 (a) Schematic depiction of the steps in hydrothermal synthesis of zeolites, (b) schematic depiction of steps in dry gel conversion (DGC) method to synthesize zeolites, and (c) detailed schematic of the setup for steam-assisted crystallization (SAC)

In this approach, although the bulk of energy needed from crystallization comes from the heating step and the grinding, it is important to note that the starting materials must be hydrated.[94,95] Some amount of water is required for the hydration processes during the crystallization phase, at the least to provide kinetically accessible pathways for the reaction. Therefore, this synthesis is not quite mechanistically solvent-free, even if no solvent is actually deliberately added.[82] Later, Wu and coworkers performed a solvent-free synthesis of zeolites from anhydrous solid materials in the presence of NH_4F, giving zeolite products with high crystallinity.[96] The presence of F^- anions was considered to result in the formation of SiF_6^{2-} species, which are suggested to initiate the crystallization of amorphous SiO_2. However, the role of anionic F^- species in the formation of the crystal from this amorphous phase remains elusive.[97,98] The use of fluorides in the synthesis also pose significant challenges due to cost and process safety related issues. Scaling up this process is also a significant challenge.

Zeolite Socony Mobil-5 (ZSM-5) is a crystalline aluminosilicate zeolite with MFI framework. It is one of the most commonly used catalysts in the petrochemical and fine chemical industry due to its unique physicochemical properties like large surface area, tunable acidity, excellent shape selectivity and high hydrothermal stability.[99–103] In 1978, a pure silica analogue of ZSM-5, called silicalite-1, was reported.[104] The most common method to synthesize silicalite-1 is the hydrothermal crystallization from a mixture containing tetrapropylammonium ions (TPA^+), a silica source and water, under autogenous pressure and temperatures ranging from 100-170 °C.[4] Later, synthesis of silicalite-1 using dry gel conversion method was reported.[105,106]

The advantages with solvent-free synthesis approaches are the obvious reduction in recycling/waste costs and that the separation of the solvent from the product is not required. In addition, potential capital savings are possible from a reduction in the need for pressure vessels, which are used in the conventional hydrothermal synthesis, as solvent heated to a high temperature produces significant autogenous pressure.[82]

Since a large amount of water has always been required for the hydrothermal synthesis of zeolites, it has been associated with a significant autogenous pressure. However, the recent research on solvent-free synthesis of zeolites, poses a question whether autogenous pressure is required for crystallization of zeolites or whether zeolites can be synthesized at atmospheric pressure. In the past, atmospheric synthesis of zeolite crystals has been achieved in the presence of large amount water as a solvent, at lower temperature, using a reflux condenser,[107] or using a dry gel conversion method with ionic liquid as the solvent in assistance with microwave radiation.[108] Solvent-free synthesis of zeolites at atmospheric pressure has not yet been demonstrated.

We proposed synthesis of siliclaite-1 can be achieved at atmospheric pressure starting from a dry gel could potentially lead to a scaled up continuous flow reactor to synthesize zeolites at atmospheric pressure. In addition to avoiding process-safety related issues, this method can also provide more control over crystallization and tuning the zeolite properties. In this setup, we designed and built a fixed-bed reactor to study the solvent-free synthesis of silicalite-1 (pure silica zeolite with MFI framework) under atmospheric pressure, assisted with steam.

3.2. Experimental details

3.2.1. Materials

Tetraethylorthosilicate (TEOS, 99%) and tetrapropylammonium hydroxide (TPAOH, 40 wt%) were purchased from Alfa Aesar. Nitrogen gas (ultra high purity) was purchased from Airgas.

3.2.2. Preparation of silicalite-1 synthesis gel

11.67 g of DI water, 2.44 g of TPAOH (40 wt%) and 4 g of TEOS were mixed well and stirred at room temperature for 2h to achieve complete hydrolysis of TEOS. The solution was then stirred at 350 rpm in an oil bath maintained at 80 °C to evaporate water. The time of stirring was variable and was controlled to achieve a final gel composition of SiO_2: 0.25 TPAOH: *x* H_2O, where $H_2O/Si = x$.

3.2.3. Hydrothermal synthesis of silicalite-1

0.3 g of the gel with composition SiO_2: 0.25 TPAOH: *x* H_2O was added to a PTFE liner of a sealed autoclave. The autoclave was placed in the oven maintained at 120 °C for varying time durations. After the crystallization time, the autoclave was cooled to room temperature under running tap water. The sample was washed with DI water until pH< 8 and centrifuged and dried in a 70 °C oven.

3.2.4. Synthesis of silicalite-1 by dry gel conversion

0.3 g of dry gel with composition SiO_2: 0.25 TPAOH: H_2O was added to a PTFE liner of a stainless-steel autoclave. 0.15 g of DI water was added to a custom-made pre-

cleaned PTFE vial (5 mL capacity, 1.5 cm diameter and 3 cm height). The vial with water was is carefully placed in the autoclave such that the dry gel does not contact with liquid water. The sealed autoclave is maintained at a fixed temperature in the oven for varying time duration. The autoclave was cooled to room temperature under running tap water. When the autoclave is opened, most of the moisture is found to be in contact with the dry gel. The sample was washed with DI water until pH< 8 and centrifuged and dried in a 70 °C oven.

3.2.5. Synthesis of silicalite-1 in a fixed bed reactor at atmospheric pressure

A synthesis fixed-bed with a stainless-steel fritted disk (diameter = 0.0451") was placed inside a temperature-controlled oven (HP 5890 gas chromatograph instrument equipped with thermal conductivity detector (TCD)) as shown in Fig 3.2. DI water was supplied to one branch and nitrogen was supplied to the other branch of the tee junction located inside the oven, where steam was generated. The reactor operated at atmospheric pressure. The 6-port valve was designed such that it could allow the steam to flow through the synthesis bed (position 'b') or to bypass the synthesis bed and flow to the TCD detector (position 'a').

A dry gel with the composition SiO_2: 0.25 TPAOH: H_2O was loaded onto the fritted disk of the synthesis bed. The oven was initially heated to 120 °C, and the valve was placed in position (a). Nitrogen flow was turned on and set to 8 sccm using a mass flow controller. The nitrogen flowrate was confirmed using a bubble flow meter connected to the end of the TCD detector. DI water supply through a syringe pump (Fisher Scientific) was turned on at 1.5 mL h^{-1}. A steady state was ensured by a constant signal on the TCD detector. The

valve was then switched to position (b) so that the steam-nitrogen mixture passed through the synthesis bed. After the desired duration of synthesis, the water flow was turned off. The synthesis bed was cooled to room temperature under nitrogen flow. The sample from the synthesis bed was then collected for further characterization.

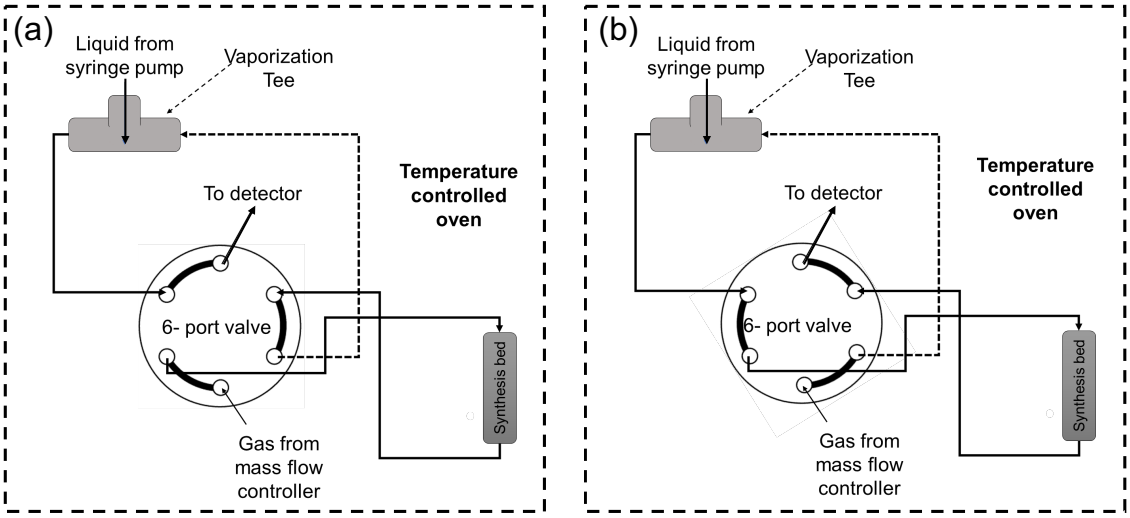

Figure 3.2 Schematic representation of the fixed-bed reactor setup in a temperature controlled oven (a) position of the 6-port valve in which steam bypasses the synthesis bed and directly flows to the detector, (b) position of the 6-port valve in which steam flows through the synthesis bed

3.2.6. Synthesis of silicalite-1 using fixed-bed reactor as a closed-system

The setup described above was modified and a 4-port valve was added (Fig. 3.3.). This valve was used to isolate the bed into a closed system. A dry gel with the composition SiO_2: 0.25 TPAOH: H_2O was loaded onto the fritted disk of the synthesis bed. The oven was initially heated to 120 °C, and the 6-port and 4-port valve were placed in position (a). Nitrogen flow was turned on and set to 8 sccm using a mass flow controller. The nitrogen flowrate was confirmed using a bubble flow meter connected to the end of the TCD detector. DI water supply through a syringe pump (Fisher Scientific) was turned on at 1.5

mL h^{-1}. A steady state was ensured by a constant signal on the TCD detector. The 6-port valve was then switched to position (b) so that the steam-nitrogen mixture passed through the synthesis bed. After 10 min of flow, the synthesis bed was isolated by switching the 4-port valve to position (b) and the oven temperature was reduced to 90 °C. The water and nitrogen flow were turned off. After the desired duration of synthesis, the synthesis bed was cooled to room temperature under nitrogen flow. The sample from the synthesis bed was then collected for further characterization.

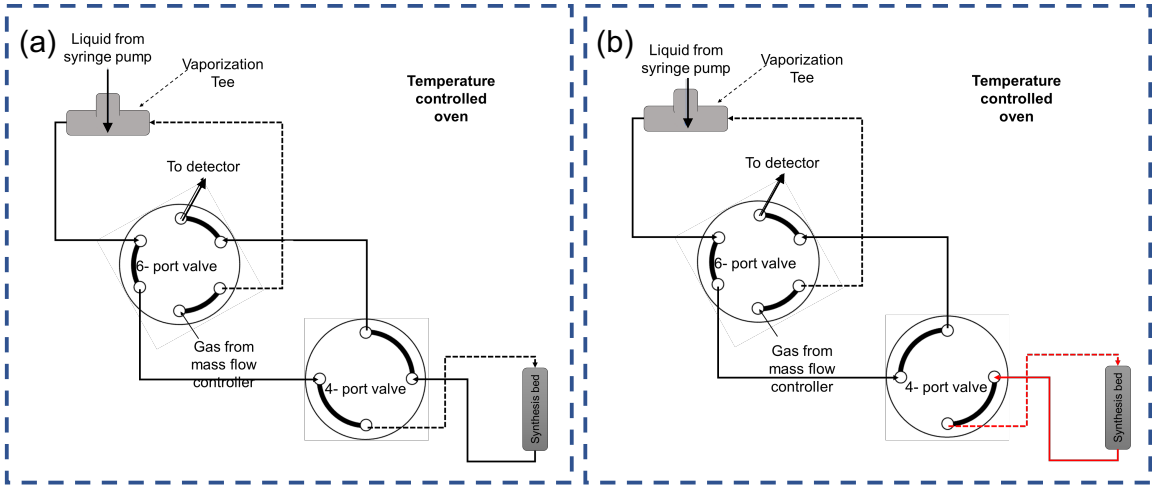

Figure 3.3 Schematic representation of the modified fixed-bed reactor setup with (a) position of the 4-port valve making the synthesis bed an open system, (b) position of the 4-port valve isolating the synthesis bed into a closed system

3.2.7. Characterization

Powder X-ray diffraction (XRD) patterns were collected on a PANalytical X'Pert Pro instrument with Cu-Kα radiation source.

3.3. Results and discussion

3.3.1. Hydrothermal synthesis of silicalite-1

Silicalite-1 was synthesized from an aged gel of composition SiO_2: 0.25 TPAOH: *x* H_2O, in a sealed autoclave at 120 °C for 15 hours. Fig. 3.4. shows the XRD patterns of as-made samples with initial H_2O/Si =1.0 to 7.4. The results show that the rate of crystallization increased with an increase in H_2O/Si. At 15 h, the sample with an initial composition of H_2O/Si = 7.4 exhibits all the peaks corresponding to a fully crystalline MFI framework. In other words, larger amount of water (solvent) present per unit weight of the gel facilitates faster crystallization by aiding in the hydration of silica species.

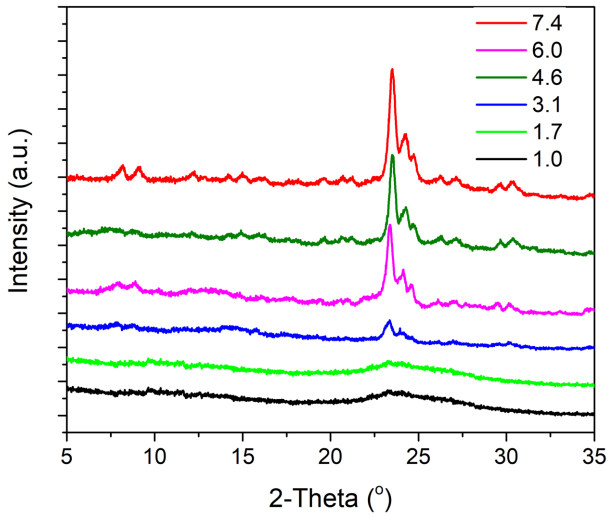

Figure 3.4 XRD patterns of as-made samples starting with initial gels with H_2O/Si varying between 1.0 to 7.4.

Fig 3.5 shows the time progression of the crystallization of gels with H_2O/Si = 1.0, 0.4 and 0.1. It was observed that the gel with H_2O/Si = 1.0 crystallized after ~48 h. However, the gels with H_2O/Si = 0.4 and 0.1 stayed amorphous even after 84 h. These

results indicated that a minimum H_2O/Si of 1.0 is required for crystallization of silicalite-1 to occur using a hydrothermal synthesis method.

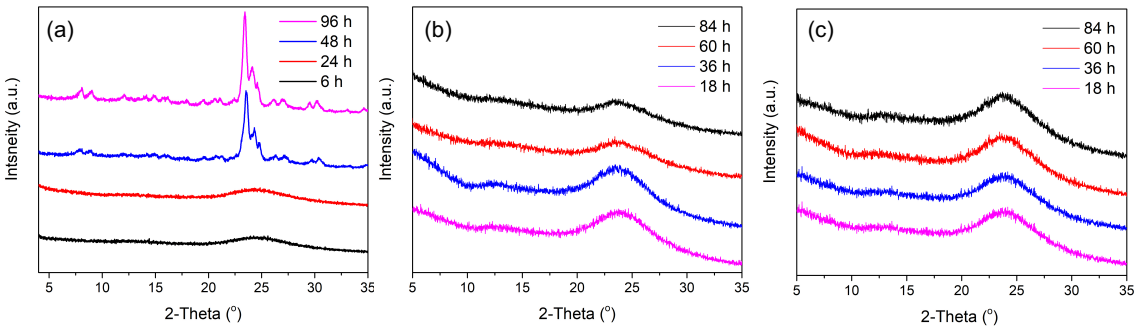

Figure 3.5 XRD patterns showing time progression of crystallization at 120 °C starting from initial gel composition with H_2O/Si of (a) 1.0 (b) 0.4 and (c) 0.1

3.3.2. Synthesis of silicalite-1 with dry gel conversion (DGC)

Silicalite-1 was synthesized using dry gel conversion method starting from an initial gel composition of SiO_2: 0.25 TPAOH: H_2O at temperatures ranging from 90 °C to 150 °C. The amount of dry gel in the autoclave (0.3 g) and the amount of water in the PTFE liner (1.5 mL) is kept constant. Fig 3.6. shows XRD patterns of gel with H_2O/Si – 1.0 at 3 h and 48 h at different temperatures. The results indicate that the rate of crystallization is higher at higher temperature. It is important to note that the gel (with H_2O/Si = 1.0) takes about 48 h to crystallize by hydrothermal synthesis method at 120 °C (shown in Fig. 3.5 (a)), whereas it takes only about 3 h to crystallize by dry gel conversion method at 120 °C (shown in Fig. 3.6 (a)). This indicates that, in the dry gel conversion method, the water in the PTFE liner vaporizes at the crystallization temperature and comes in contact with the dry gel, thus participating in hydration of silica species and facilitating faster crystallization. On the other hand, when the same gel is used in the hydrothermal synthesis

method, the only water available is the water present in the gel itself. Therefore, the crystallization is slower.

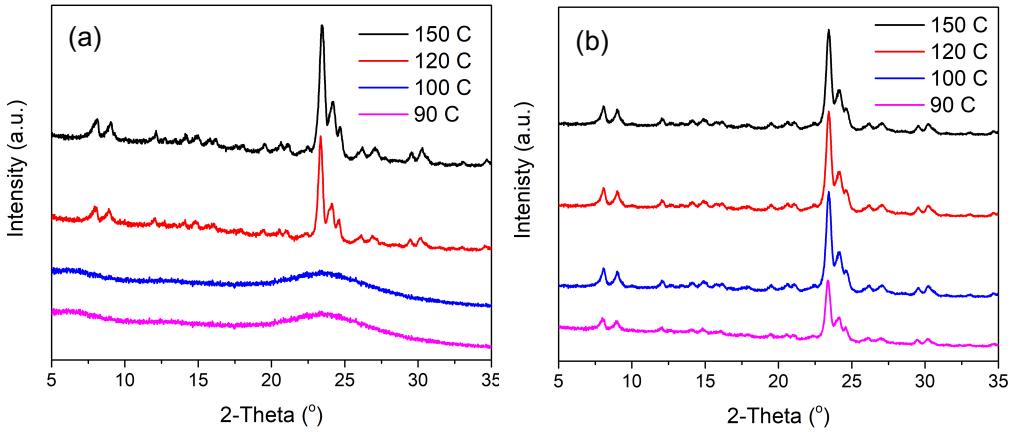

Figure 3.6 XRD patterns of as-made samples at temperatures ranging from 90° C to 150 °C at (a) 3 h and (b) 48 h

3.3.3. Synthesis of silicalite-1 in a fixed-bed reactor at atmospheric pressure

Dry gel with composition SiO_2: 0.25 TPAOH: H_2O was loaded into a fixed bed reactor operating at 120 °C and 1 atm. A mixture of steam and nitrogen, with varying partial pressures of water (0.16 to 0.80) was continuously flown through the reactor. The XRD patterns of the original dry gel and the final sample are shown in Fig. 3.7. The results indicate that syntheses under the given operating conditions result into amorphous samples, which suggests that crystallization does not occur.

However, dry gel with the same composition crystallized at 120 °C in only 3 h in a sealed autoclave, as shown by the data in Fig. 3.6. This poses an important question whether crystallization of silicalite-1 can occur at atmospheric pressure. Kim and coworkers provided evidence to support the premise that in dry gel conversion (DGC)

method, some of the vapor phase water condenses into the micropores of the amorphous dry gel to form a restricted, liquid water phase that then sets up a vapor-liquid equilibrium with the vapor water phase. The autogenous pressure inside the autoclave is sufficient to cause capillary condensation within the micropores of the dry gel. Zeolite crystallization begins at the interior of the dry gel and travels towards the surface of the particles. At any point in time, there is a composite of silicalite-1 crystals and the amorphous dry gel unitl the sample is fully crystalized. This suggests that presence of liquid water inside the micropores of the amorphous gel is necessary to facilitate crystallization.

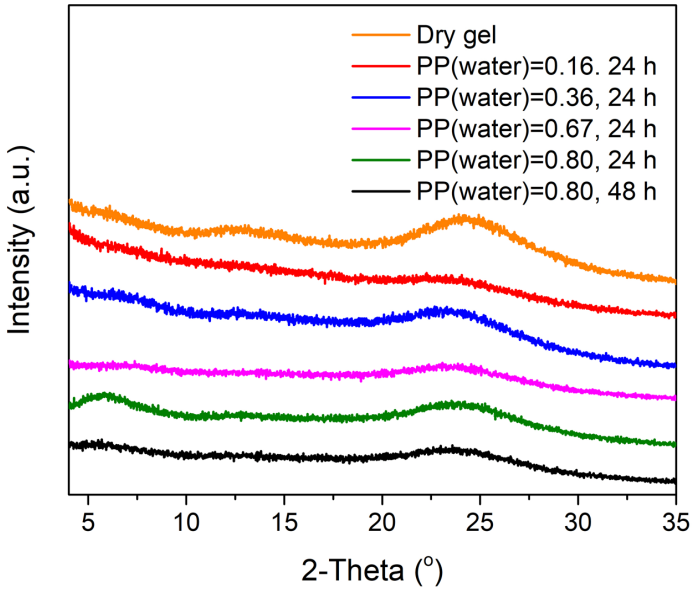

Figure 3.7 XRD patterns of final samples from the fixed-bed reactor subjected to 120 °C and a steam-nitrogen mixture with a partial pressure of water varying from 0.16 to 0.80

The Kelvin equation can be used to study the capillary condensation of water in the micropores of the dry gel. The Kelvin equation is given by:

$$ln\left(\frac{P}{P_o}\right) = -\frac{2\gamma V_m cos\theta}{RTr_k}$$

where V_m is the specific molar volume of water (mol m^{-3}), γ is the surface tension of water (J m^{-3}), θ is the contact angle of water, T is the temperature of the system (K), R is the universal gas constant (J mol^{-1} K^{-1}) and r_k is the pore radius. Po is the saturation pressure of water at temperature (T) and P is the partial pressure of water in vapor phase that is required for capillary condensation to occur in pores with radius r_k. The Kelvin equation was used to determine the partial pressure of water in vapor phase required for condensation to occur in the pores of the dry gel. The pores were assumed to have diameters be in the range of 1 to 4 nm. The data is shown in Fig. 3.8. The maximum partial pressure of water used in our experiments was 0.8 bar. The data shows that at 120 °C, the partial pressure of required for capillary condensation to occur is greater than 0.8 bar for most of the pores. This suggests that under the operating conditions in our experiments, only negligible capillary condensation occurred in the micropores of the dry gel leading to insufficient liquid water available to facilitate crystallization.

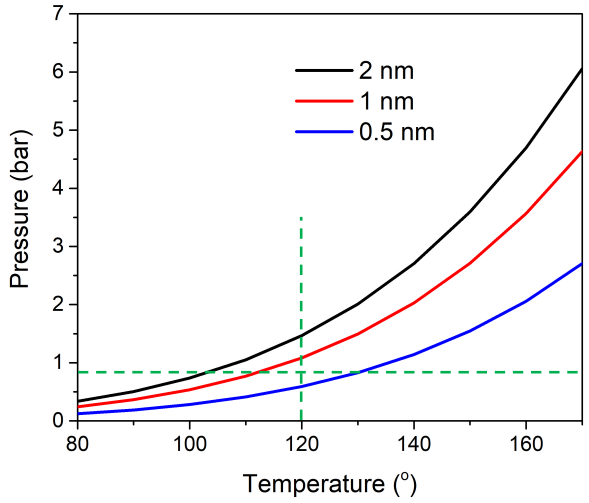

Figure 3.8 Plot of partial pressure of water in vapor phase required for capillary condensation to occur (bar) versus the temperature of the system (°C) for pores of radii 0.5, 1 and 2 nm.

3.3.4. Synthesis of silicalite-1 using fixed-bed reactor as a closed system

Since presence of liquid water is deemed essential for crystallization of zeolite to occur, we proposed that water could be condensed from steam by capturing steam at high temperature and lowering the system temperature for condensation to occur. The XRD for the sample synthesized using this method (lowering the temperature from 120 °C to 90 °C) is shown in Fig. 3.9, which indicates that the final sample after 48 h was amorphous. For 0.3 g of the dry gel, 8.37 mg of water was condensed by lowering the temperature from 120 °C to 90 °C. However, the rate of crystallization at 90 °C is very low, which could be the probable reason for the final sample to be amorphous after 48 h.

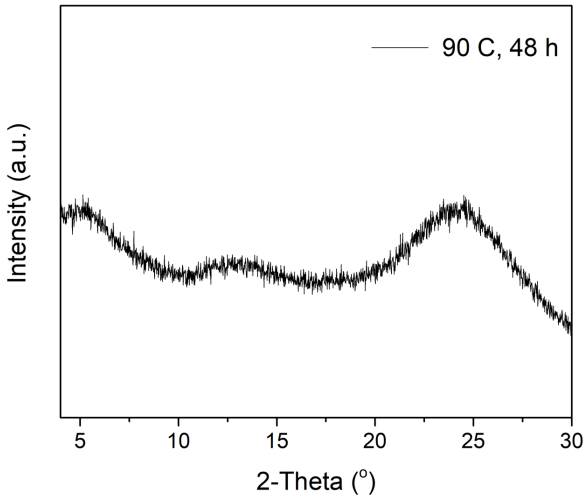

Figure 3.9 XRD pattern of the final sample after 48 h and 90 °C, operating the fixed bed reactor as an open system

3.4. Conclusions

In summary, the crystallization kinetics of silicalite-1 was studied in a sealed autoclave system under autogenous pressure (hydrothermal synthesis and dry gel conversion) and an open fixed-bed reactor system at atmospheric pressure. The rate of

crystallization is higher with higher H_2O/Si ratio in the initial synthesis gel. The rate of crystallization is higher with higher temperature. The results also indicated that at atmospheric pressure, the partial pressure of water in the vapor phase should be sufficient to cause capillary condensation of water in the micropores of the amorphous dry gel. The presence of a small quantity of liquid water inside the micropores of the dry gel is considered necessary for crystallization to occur.

CHAPTER 4

EXFOLIATION OF TWO-DIMENSIONAL ZEOLITES FOR HYDROGEN SELECTIVE MEMBRANES

4.1. Background

4.1.1. Need for energy-efficient CO_2 capture technologies in electricity generation

About one-third of the electricity generation in the United States comes from traditional pulverized coal-fired power plants.[109] Carbon dioxide emissions to the atmosphere in the United States were 6.5 billion metric tons in 2017, which formed 82% of the total greenhouse gas emissions. About one-third of these emissions originate from coal-fired electricity generation (Fig. 4.1.).[110] These emissions will need to be mitigated in order to reduce the impact of projected climate change within this century. Since coal is expected to remain a major player in the global electricity generation mix through at least 2030, there is a need to develop new technologies for economical production of electricity from coal that minimize the release of CO_2 to the atmosphere. The goal of the Paris Agreement (2016) is to pursue efforts to control CO_2 emissions such that the global temperature rise is limited to 1.5° above pre-industrial levels, recognizing that this would sustainably reduce the risks and impacts of climate change. This has prompted research in recent areas in technologies for carbon dioxide capture and sequestration (CSS). Integrated gasification combined cycle (IGCC) power plants have emerged as a promising technology that can achieve higher efficiencies than the conventional pulverized coal power plants.

When operated with carbon capture, IGCC units enable CO_2 capture with lower penalties in energy efficiency and cost of electricity than the pulverized coal counterparts.[111]

Most of the coal power plants in the United States are pulverized coal (PC) power plants, in which heat is recovered by combusting coal in a boiler as shown in Fig. 4.2. The high pressure steam generated in the boiler drives a steam turbine that generates electricity. Carbon dioxide is captured from the flue gases generated from the boiler using a amine-based absorption process. This is called post-combustion capture of CO_2. The concentration of CO_2 at the entrance of the amine scrubber is only about 14%, and hence this process decreases the overall plant efficiency.

In a newer technology, called integrated gasification combined cycle (IGCC), coal is gasified to syngas (a mixture of CO and H_2) instead of being combusted. Syngas is then upgraded to CO_2 and producing more hydrogen by a moderately exothermic, equilibrium-limited reaction called water-gas-shift (WGS) reaction as shown in Fig. 4.3. The WGS reaction is given below:

$$CO + H_2O \rightarrow CO_2 + H_2O \quad \Delta H^{o}_{298\,K} = -41.1\ \text{kJ mol}^{-1}$$

The equilibrium of the WGS reaction is favored at low temperatures and is unaffected by operating pressure. This increases the concentration of CO_2 in the flue gas stream to about 40%, making its recovery easier and more efficient. The current mature technologies for carbon-capture include a physical solvent processes (Selexol), which are not environmentally friendly and are expensive. After CO_2 capture, the hydrogen-rich fuel is then sent to a combustion turbine, which generates electricity. This approach is called pre-combustion CO_2 capture.

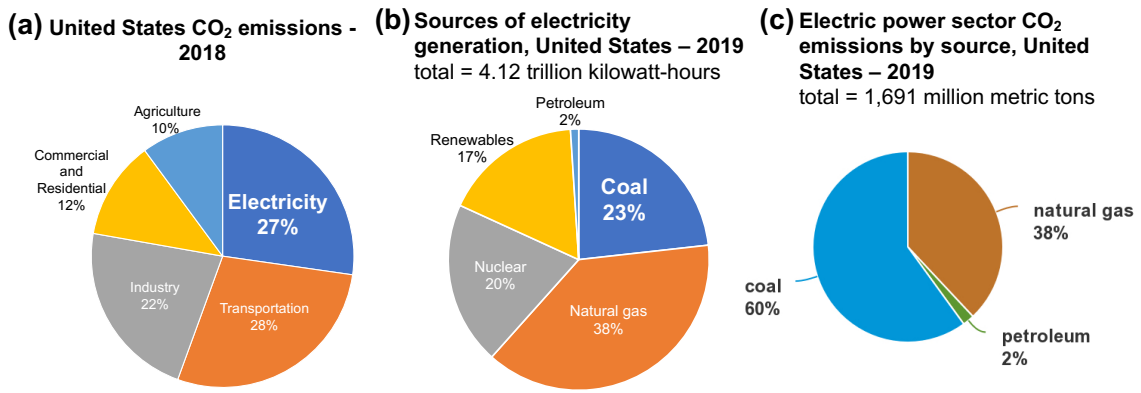

Figure 4.1 (a) Carbon dioxide emissions in the United States (2018), (b) Sources of electricity generation from the United States (2019), (c) Electricity power sector emissions by source in the United States (2019) Data from the U.S. Energy Information Administrations (EIA)

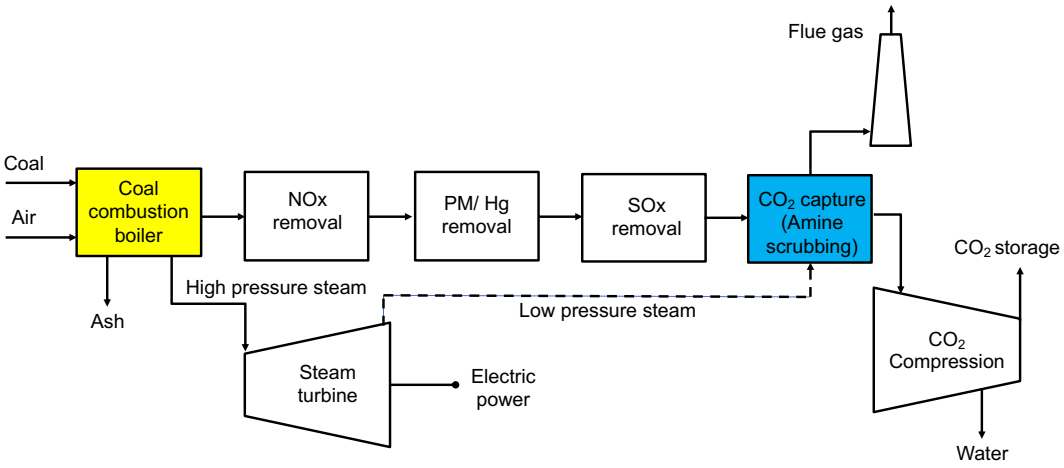

Figure 4.2 Post-combustion CO_2 capture in a pulverized coal (PC) power plant

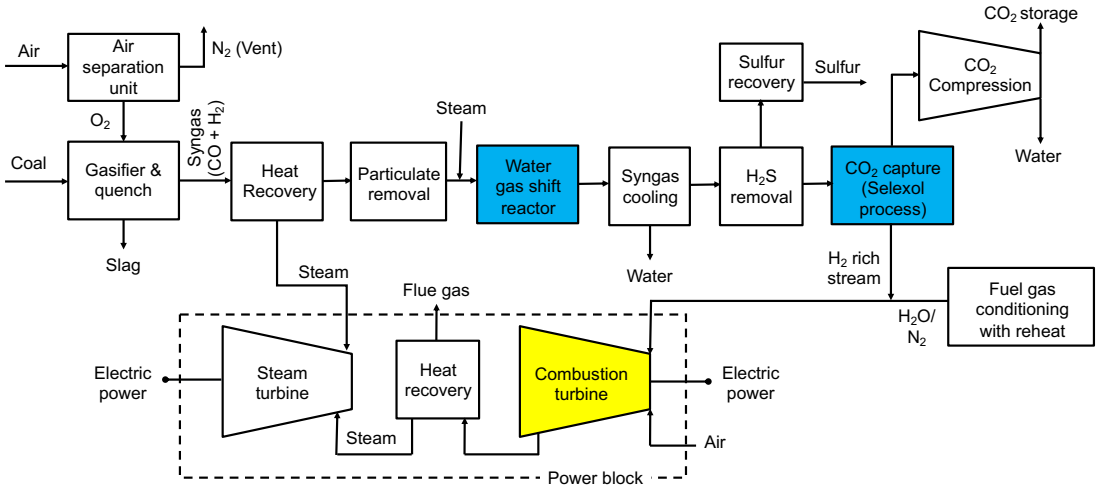

Figure 4.3 Modified integrated gasification combined cycle (IGCC) with pre-combustion CO_2 capture unit

4.1.2. Water gas shift membrane reactor (WGSMR)

Today's commercially available pre-combustion CO_2 capture technologies (Selexol process) cost around \$60/ton to capture CO_2. The goal of Department of Energy's (DOE) research efforts is to reduce this cost to \$30/ton of CO_2. Also, the Selexol process is energy-intensive and requires recycling/ disposal of solvents and hence not environmentally friendly. A WGS membrane reactor (WGSMR)[112] could replace the option of CO shift conversion followed by a CO_2 removal unit (using solvent Selexol). A WGSMR consists of a hydrogen-selective membrane, and thus can shift the equilibrium of the WGS reaction toward the product, caused by the continuous removal of hydrogen through the membrane (Fig. 4.4. and 4.5.). A membrane reactor typically consists of two concentric cylinders separated by a selective membrane, one of which acts as a reaction zone and other as a permeation zone. Incorporating a WGSMR has the following advantages: (i) smaller physical size requirement (ii) lower energy consumption. It can also

make the process environmentally friendly (membrane processes, unlike absorption-based processes, do not require treatment and disposal of spent solvents).[113]

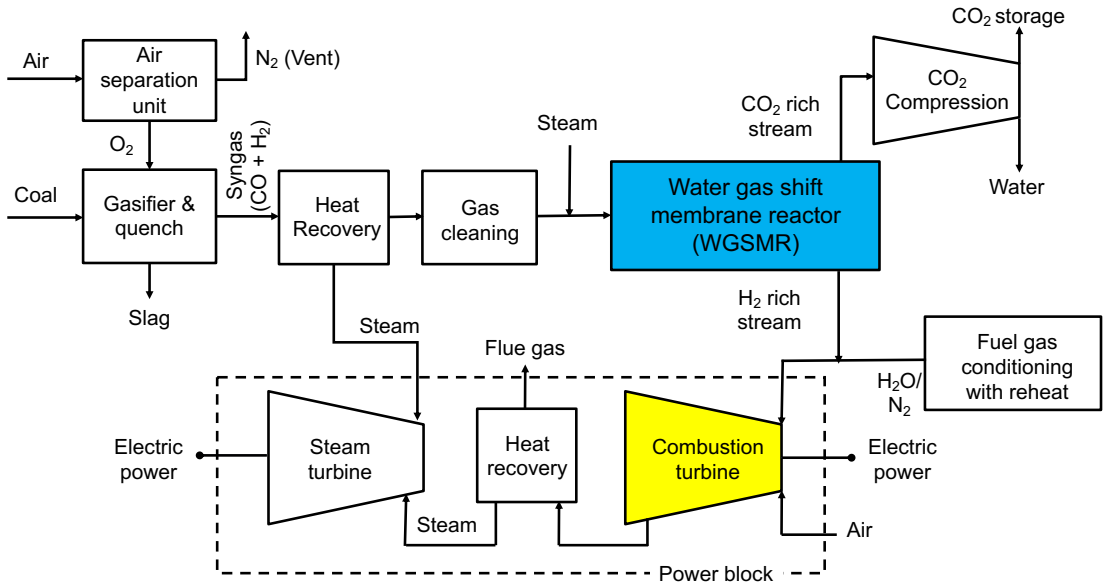

Figure 4.4 Integrated gasification combined cycle (IGCC) with pre-combustion CO_2 capture using a water-gas-shift membrane reactor (WGSMR)

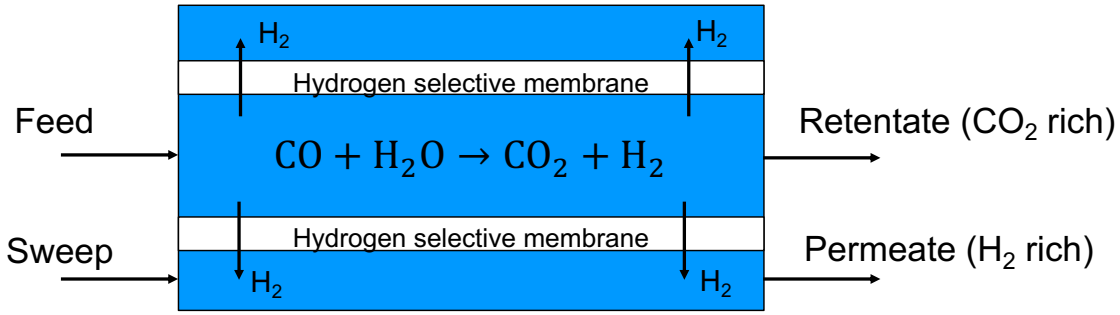

Figure 4.5 Schematic representation of the water gas shift membrane reactor (WGSMR)

4.1.3. Materials for hydrogen selective membranes

A challenge with using hydrogen-selective membranes in the WGS section of a coal-based gasification plant is their stability under high-pressure and high-temperature conditions (250-450°C, 20 bar), and in presence of steam and possibly other trace components such as hydrogen sulfide (H_2S). Typical materials[114–137] used or proposed for hydrogen-selective membranes are:

(a) Dense metals: Typically Pd based. Pd-based materials are the most researched for hydrogen selective membranes. They have nearly infinite selectivity for hydrogen. However, they are expensive, poisoned by H_2S even at low concentrations, undergo phase transformations and are subject to hydrogen embrittlement.

(b) Dense polymers: They are inexpensive, however, they have low H_2 selectivity and not stable at high temperature.

(c) Amorphous silica: They have high cost and hydrothermally unstable.

(d) Porous carbons: They have low selectivity, brittle, and are subject to oxidative degradation at high temperatures.

(e) Zeolites: They are crystalline aluminosilicates with well-ordered micropores (3-15 Å), and can act as molecular sieves. Their framework consists of TO_4 tetrahedra, where T =Si or Al (Fig. 4.7.). Zeolites with different framework types are named using three-letter codes by International Zeolite Association (IZA). Examples are—BEA, FAU, LTA, MWW, MFI, etc. Zeolite-based, molecular sieve membranes are a promising alternative for this application, since they have a potential for high selectivity, high flux and to be hydrothermally stable.

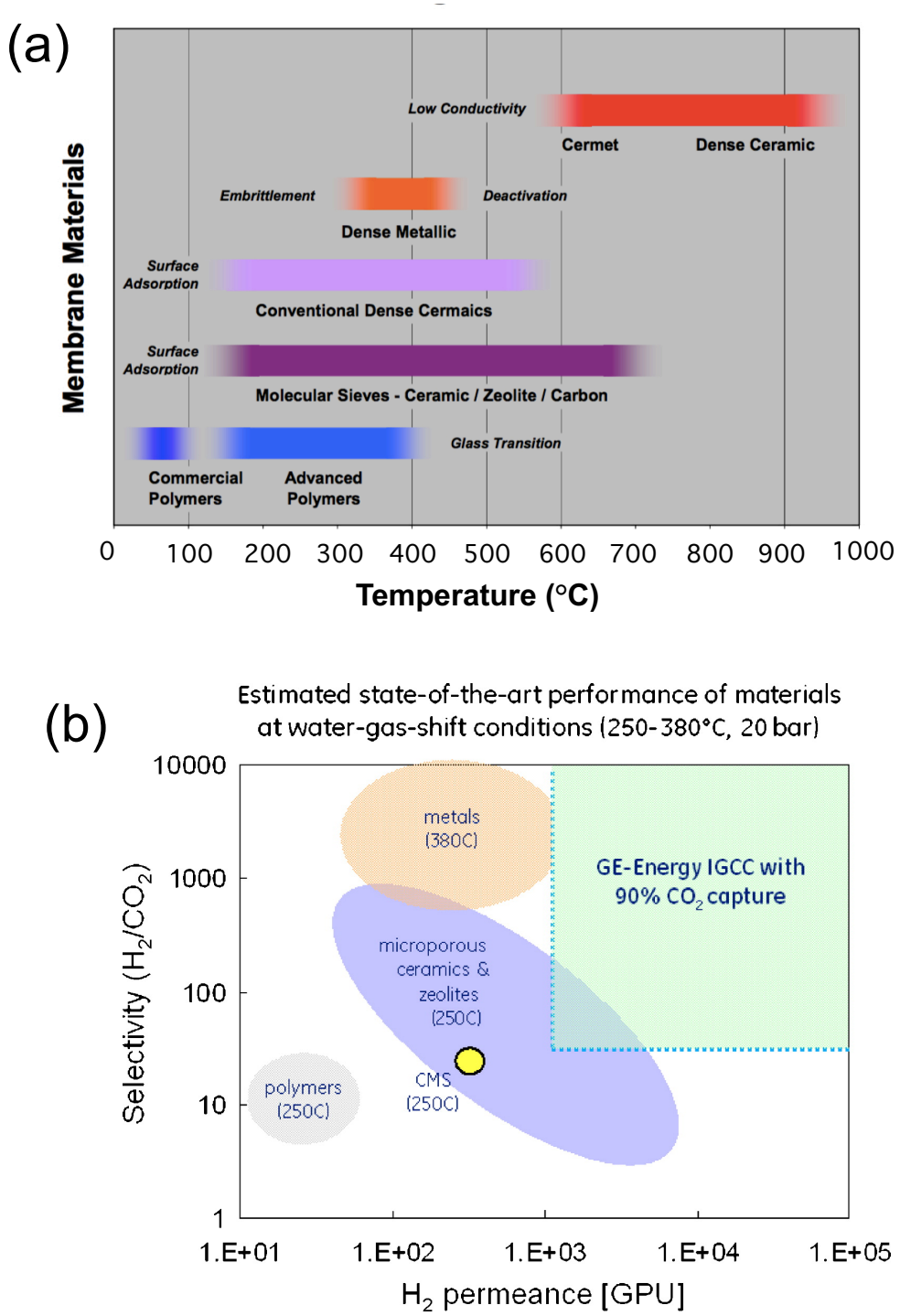

Figure 4.6 (a) Stability of various materials for hydrogen-selective membranes (b) membrane performance target for IGCC carbon dioxide capture, and estimated material performance capabilities

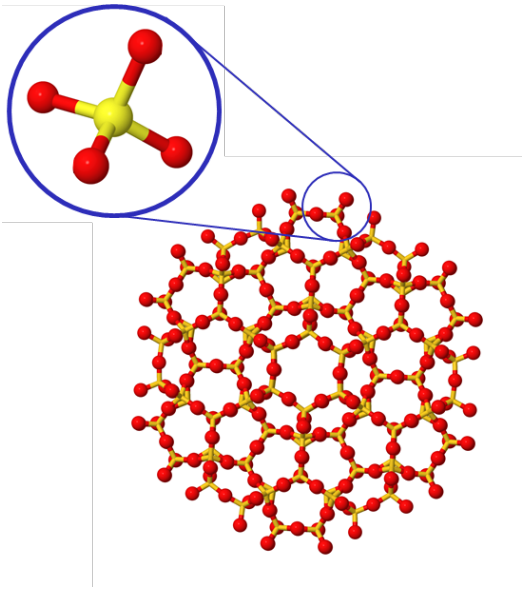

Figure 4.7 Zeolite framework depicting TO_4 tetrahedra (Yellow = Si or Al; Red = O)

4.1.4. Two-dimensional zeolites (2DZs)

Most of the synthetic zeolites are synthesized via solvothermal synthesis by use of different reaction conditions, reactants, and organic structure directing agents (OSDA). The reaction proceeds either directly to 3D zeolites (in most cases) or it can proceed via a two-dimensional (2D) layered zeolite precursor. Two-dimensional zeolite layered precursors are a new class of porous materials with the framework propagating only in two dimensions.[138–142] Out of the 237 zeolite framework types recognized by the International Zeolite Association (IZA), only about 5% have found to produce 2D forms, although it may be that many more zeolites, can yield a 2D form in one way or another.[138] The 2D layered precursor produces the standard 3D zeolite by topotactic condensation induced by calcination. But they could also be modified into other types of structures, particularly expanded ones, by swelling or pillaring. They could also be exfoliated into 2D nanosheets,

which can be only 2-4 nm thick (Fig. 4.8). The onset of this new paradigm is linked to the first synthesis of MCM-22(P) (Mobil Composition of Matter number 22), a 2DZ layered precursor with MWW framework in the year 1994 by Mobil researchers.[143]

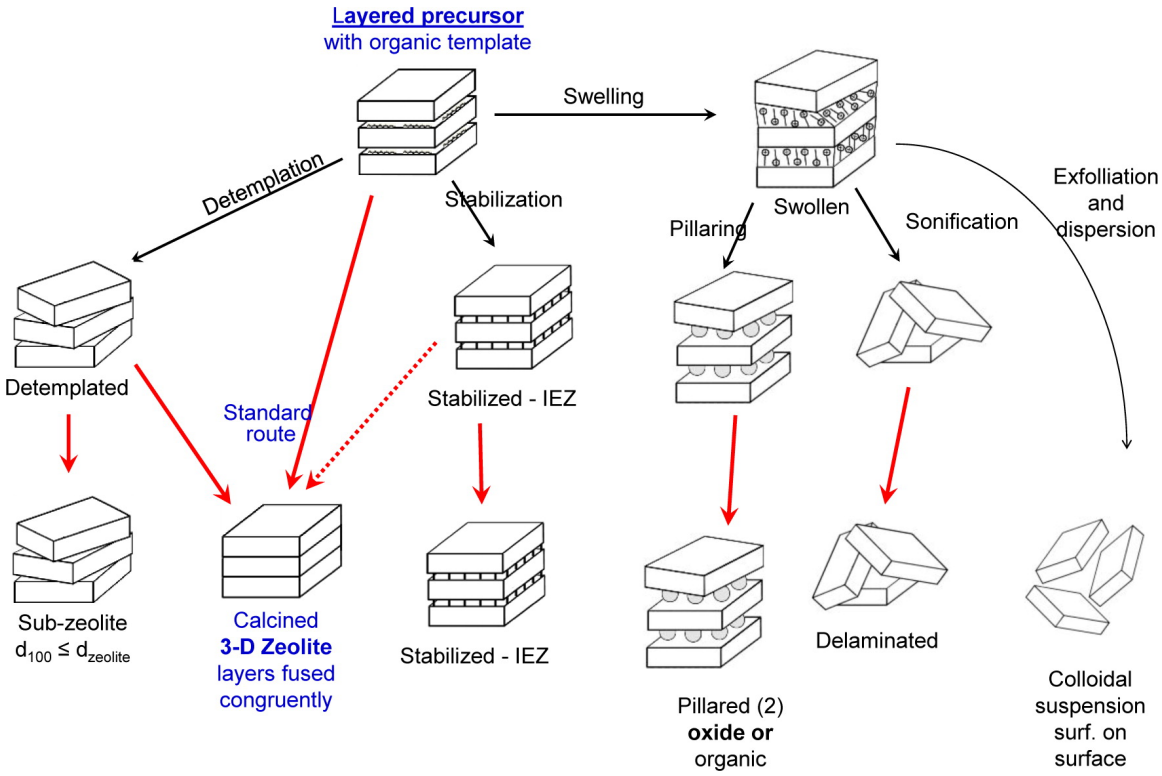

Figure 4.8 Schematic representation of possible post-synthetic modifications of 2D zeolite layered precursors. 2DZ layered precursors can be swollen, delaminated, exfoliated or directly calcined.[138]

4.1.5. Zeolite membranes for high-flux separations in industrial processes

Zeolites can act as molecular sieves, and continuous zeolite films grown on porous supports bear great potential to replace the currently used energy-intensive separation methods used in industry.[144,145] For their successful applications in industry, these films should be grown satisfying the following requirements:[146] (a) they should be grown with channels vertically oriented with respect to the substrate planes from the top to the bottom

of the films to maximize the permeance (b) they should be grown as thin as possible to maximize the permeance (c) they should be grown pinhole-free to maximize the separation factor (d) they should be grown in such a way that they do not form cracks during calcination to remove organic templates from the template bearing zeolite films (e) they should be grown economically by saving chemicals, simplifying procedures, and replacing the typically used alumina supports with less expensive ones (f) they should be grown environmentally-friendly by not producing any wastes. High permeance results into smaller membrane area required, and thus reduces the capital cost. Higher separation factor reduces the operation costs.[147,148]

Although a lot of progress has been made on the synthesis and application of zeolite membranes and coatings in the recent years,[7] so far only one type of zeolite membrane has been commercialized. LTA membranes are used in the dehydration of different solvents because of their strong hydrophilicity and suitable pore size. There is still no gas separation process worldwide in operation using zeolite membranes.

4.1.6. High flux MFI membranes

Most of the research in the past two decades has been focused on growing films from silicalite-1, a zeolite with MFI framework. This framework has 10 membered ring (10 MR) straight channels running along the b-axis, that have a dimeter of about 0.55 nm, suitable for xylene isomer separation, which is currently done using distillation in industry (Fig. 4.9). A critical factor for the practical application of the silicalite-1 films is the percentage of straight channels that are open from the top to the bottom of the film (since it controls the flux).[149] Since direct growth of zeolite films on porous substrates leads to

randomly-oriented films,[150] films are grown by first depositing oriented seed crystals on a support and then growing a continuous film using secondary growth. Randomly oriented films reduce permeance through the membranes, but also have an intrinsically high propensity to crack formation during the calcination step owing to the complex thermal expansion coefficients of the grains.[151] Therefore, preservation of the preferred orientation of the seed crystals during secondary growth is important (Fig. 4.10). Preferred orientation during gel-based secondary growth is ensured using appropriate structure directing agents and other principles.[152–165]

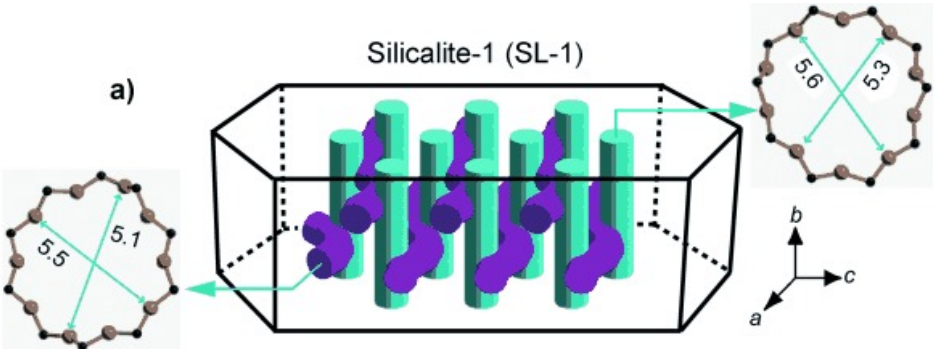

Figure 4.9 Schematic of silicalite-1 crystal depicting 10MR channels along the b-axis

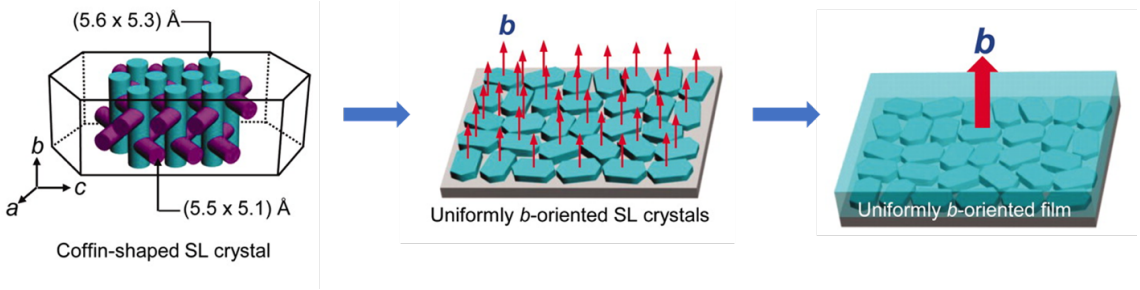

Figure 4.10 Secondary growth of b-oriented silicalite-1 crystals into a uniformly b-oriented film[149]

A breakthrough in the field was achieved when Ryoo and coworkers synthesized a 2DZ layered precursor with MFI framework, called 'multilamellar MFI', using structure directing agents, capable of dual-templating.[166] The di-quaternary ammonium portion of the surfactant templates the MFI layer pore structure, whereas the long tail serves as a space-filler between the MFI layers (Fig. 4.11). Multilamellar MFI was successfully exfoliated into 2D MFI nanosheets (~3.5 nm thick)[167] by melt-compounding the layered precursor with polystyrene in a twin-screw extruder.[168] Density gradient centrifugation was used to purify these nanosheets (remove the polymer and the unexfoliated material) to form high-purity 2DZ nanosheet suspensions (Fig. 4.11).[169]

The high-purity suspensions of 2DZ nanosheets in organic solvents can be used to make coatings of the nanosheets on porous supports by vacuum filtration. The nanosheets are better than the seed crystals used in the past, to make continuous zeolite films, since the nanosheets are very thin (2-4 nm) and molecularly-sized small diffusion lengths. The nanosheets, remain at the support surface and form oriented coatings since they deposit with their short dimension perpendicular to the support surface. However, the deposits contain nm-sized pinhole defects, which should be eliminated to reduce the non-selective paths in a separation membrane. This is accomplished by mild secondary growth aiming to close the defects while keeping the overall membrane thickness at the minimum, as well as preserving the preferred orientation of the film. Although a hypothetical ideal membrane would be single-layer-thick (Fig. 4.12), overall film thickness increases during secondary growth and the state-of-the-art MFI films are ~100 nm thick.[170]

Although zeolite membranes can lead to substantial energy savings, high costs per unit area of the membrane ($5000 to $10,000 per square meter for an assembled module)

lead to long payback time (e.g. 10 years), which have limited the implementation of zeolite membranes in industry. Major share of this cost is imposed by the underlying support. Unless costs per unit area decrease, a 10-fold increase in flux compared to the current state-of-the-art is the only way forward.[171] Since layer thickness is 2-3 nm, films as thin as 10 nm should be feasible, provided that compact-enough layers can be deposited. In order for this to be achieved, efforts to increase the nanosheet aspect ratio is needed. Large aspect ratio nanosheets can enable good overlap pf nanosheets, minimizing gaps.[7]

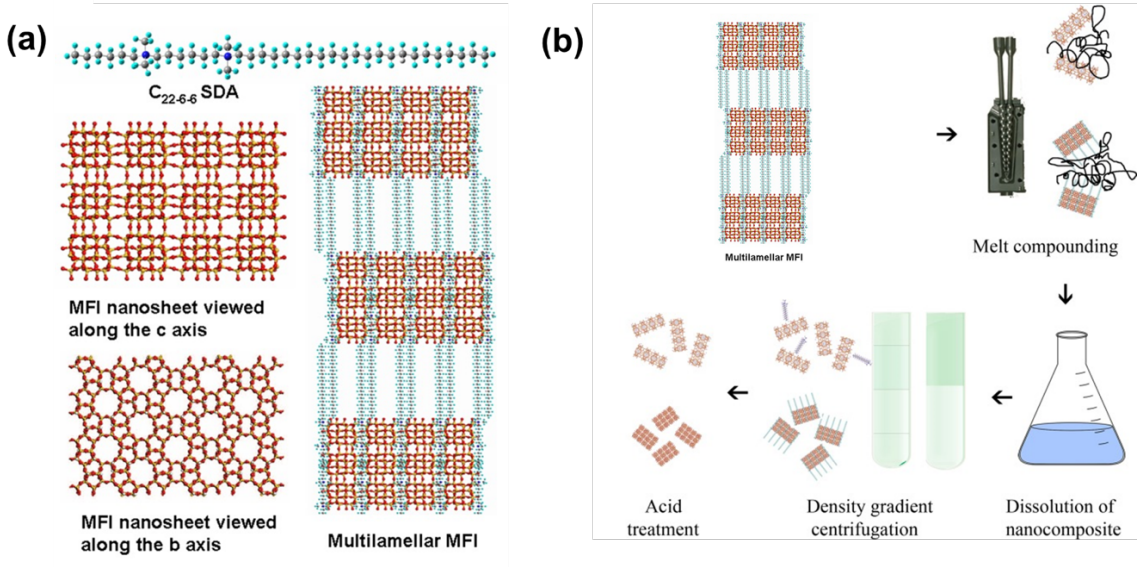

Figure 4.11 (a) The dual templating structure directing agent and multilamellar MFI structure, (b) schematic depiction of the method to prepare high purity MFI nanosheet suspension

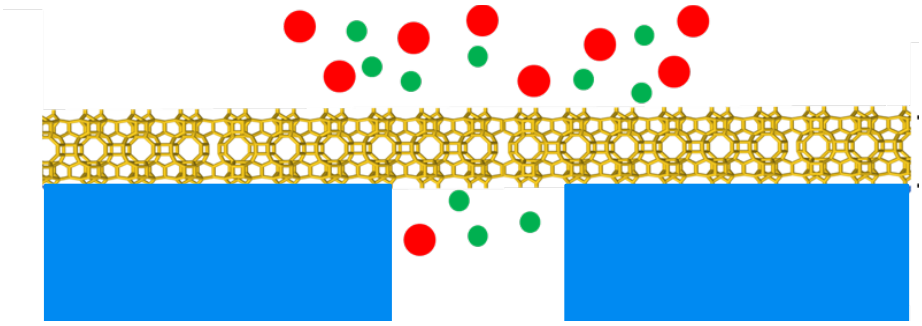

Figure 4.12 Ideal single-layer thick membrane offering highest permeance

Further work has been done to improve the selectivity of xylene isomer separation using MFI membranes by synthesizing large aspect ratio MFI nanosheets by bottom-up approach,[172,173] and using novel deposition methods to make more compact films[174–177] A life scale assessment of the industrial scaling of zeolite membrane manufacturing was done, which proved that the use of silica/alumina supports and gel-based secondary growth technique had the most environmental impact. MFI nanosheets without any organic structure directing agents (that can disperse well in water) were prepared by treating the nanosheets with Piranha solution (a mixture of H_2SO_4 and H_2O_2). These SDA-free nanosheets could be used to make coatings on porous polymer (polybenzimidazole) supports, which have less environmental impact.[178]

Use of gels for secondary growth of films has been a common tradition. However, gel-based secondary growth needs gel preparation and aging steps, washing the films with copious amounts of water, neutralization of mother liquors for disposal and large amounts of chemical requirement. A gel-free secondary growth method would be highly desirable. Such a method was developed, which allowed use of minimal chemicals and also finer control of the orientation of the film during secondary growth.[146] Sintered silica fiber (SSF)

supports, which provide mechanical strength, were used to make MFI membranes, which improved the selectivity and flux of the xylene isomer separation.[179]

4.1.7. MCM-22(P): a promising material for hydrogen-selective membranes

MCM-22(P) is an aluminosilicate zeolite, with MWW (MCM-tWenty-tWo, Mobil Composition of Matter with sequence number twenty-two) framework type, containing micropores oriented parallel to the layer's basal plane and defined by ten interconnected SiO_4 tetrahedra, which form ten-membered rings (10MR).[143,180–185] Perpendicular to the layers, the pores are hourglass shaped with twelve-membered rings (12MR) at the entrance and six membered ring (6MR) central constrictions (Fig. 4.9). The diameter of the 6 MR aperture is about 0.3 nm, whereas the kinetic diameters of H_2 and CO_2 are 0.289 nm and 0.330 nm respectively, suggesting that only hydrogen can pass through the aperture. Simulation studies of hydrogen transport through sodalite (SOD) zeolite, which also contains similar 6MR apertures, indicate the ability of hydrogen to pass through the 6MR aperture.[186] Thus, MCM-22(P) has a potential to be used as a material for fabricating hydrogen-selective membranes. It has also shown potential in corrosion-protection applications.[187] Long-term steam stability studies indicated that aluminosilicate MCM-22(P) and its pure silica analog ITQ-1[188] (after treatment with $SiCl_4$), retained ~60% and ~70% of their microporosity after 84 days of steaming (10 barg, 95% water) at a temperature of 350°C.[189] This study bolsters optimism that MWW-based zeolite materials can be used as hydrogen-selective membranes in WGSMR.

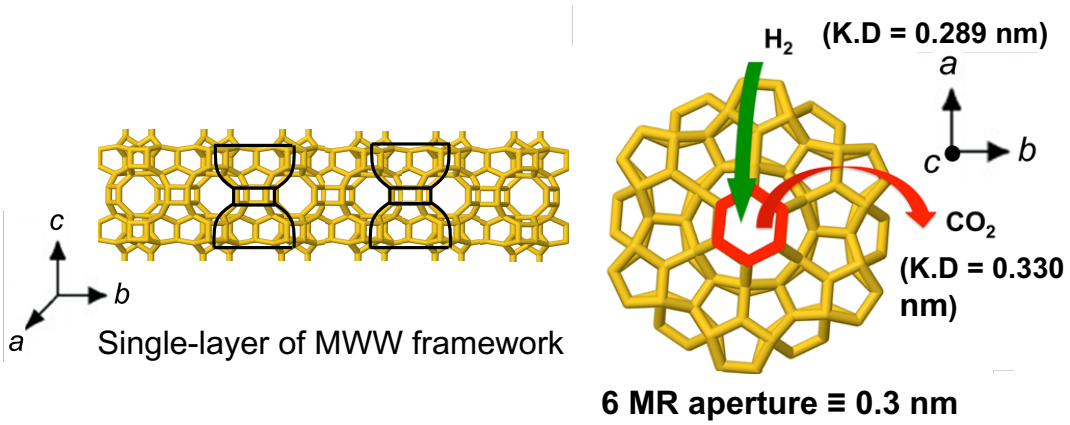

Figure 4.13 Schematic of a single layer of MCM-22(P) showing hour glass shaped pores with 12-membered ring (12MR) at the entrance and six-membered ring (6MR) central constriction

4.1.8. Swelling, delamination and exfoliation of MCM-22(P)

The 2DZ layered precursor MCM-22(P) was swollen at high pH and high temperature, using a quaternary ammonium surfactant to increase its interlayer spacing.[190–192] The swollen zeolite could further be delaminated by subjecting it to ultrasound treatment (Fig. 4.14). The delaminated zeolite was called ITQ-1, which exhibited high surface area (~700 m^2/g). This opened a new avenue towards using MWW layered materials for a variety of applications.

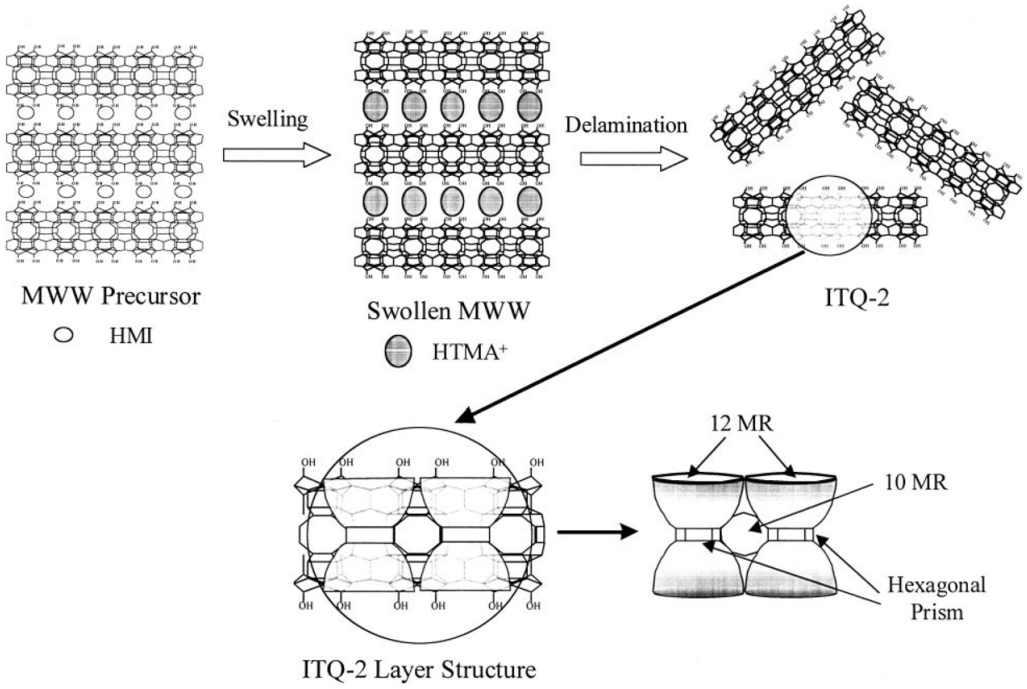

Figure 4.14 Delamination of MCM-22(P) by first swelling the zeolite followed by ultrasound treatment[190]

A room temperature swelling process was later developed, which could preserve the crystalline microstructure of the MWW layers.[193] The swollen material was also exfoliated by melt-compounding it with polystyrene in a twin-screw extruder (Fig. 4.15). Above the transition temperature of polystyrene, the extrusion process provides a shear force which leads to the exfoliation of the material. Single-layer thick (~2.5 nm) MWW nanosheets were obtained.[168] However, this exfoliation method faces the challenges of high temperature operation (150-200°C), low yield and a potential for damaging the lateral size of the nanosheets due to high shear forces (which is undesirable, since high-aspect ratio nanosheets are required for compact nanosheet coatings). Hence, a more facile, efficient exfoliation technique, that can produce high aspect ratio nanosheets is highly desired.

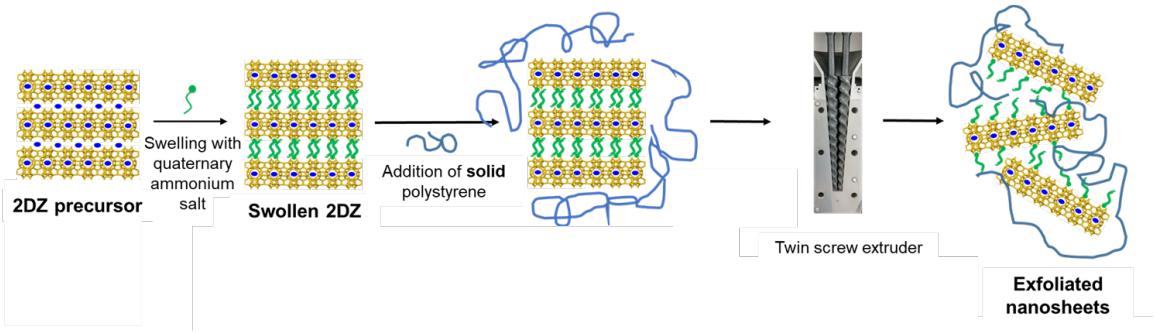

Figure 4.15 Schematic depiction of exfoliation of MCM-22(P) by melt blending with polystyrene at high temperature

4.1.9. MWW membranes

Although substantial work has been done in developing exfoliation and purification techniques, secondary growth and deposition methods to make high quality MFI coatings, research on MWW coatings is still in its nascent stage. MCM-22/silica flake coatings were made by layer-by-layer deposition and tested for H_2/N_2 separation.[187,194] MWW nanosheet coatings were also made by Varoon and coworkers using the nanosheets obtained by melt-blending exfoliation. These nanosheets were deposited on α-alumina supports by vacuum filtration, subjected to gel-based secondary growth and tested for H_2/He separation.[168] However, misoriented growth on the top of the seed layer of nanosheets was observed after secondary growth (Fig. 4.16). As mentioned earlier, it is difficult to control the orientation of the film when a gel-based secondary growth method is used, and preservation of preferred orientation during secondary growth is required for high permeance and to avoid crack-formation in the coating during calcination.

The current challenge is to develop a facile method for exfoliation of MCM-22(P), or its pure silica analog ITQ-1(P), which can yield high aspect-ratio MWW nanosheets.

The other challenge is to form compact and uniform coatings of these nanosheets on a porous support and control the orientation of this film during secondary growth.

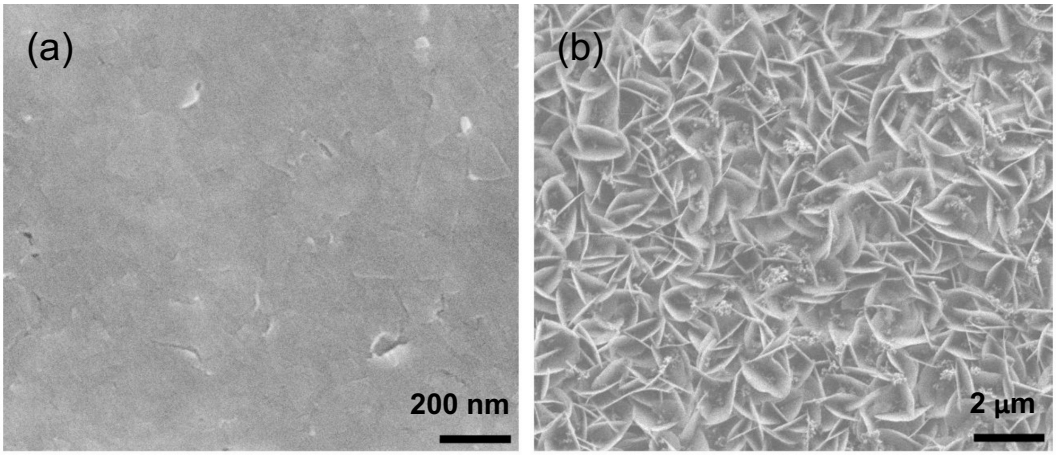

Figure 4.16 (a) SEM image of MWW nanosheet coating on porous α-alumina support, (b) SEM image of the MWW film after gel-based secondary growth. The image shows misoriented crystal growth.

4.1.10. Inspiration from the exfoliation of clay

Many methods have been established for separation of organo-clay stacks into discrete clay sheets.[195] These procedures include: sol-gel template synthesis,[196,197] in situ intercalative polymerization,[198–200] emulsion polymerization,[201,202] and melt compounding.[203–207] Sun and coworkers utilized a unique low energy technique, called 'self-exfoliation'.[208] Surface modified organo-clay, when embedded in a matrix of telechelic polybutadiene, exfoliated by itself without requiring any additional energy input via shearing or sonication. Both hydroxyl and carboxyl functional groups were shown to provide full exfoliation of the composite through appropriate annealing conditions.[209] The clay was surface modified with octadecyltrimethyl ammonium chloride counterions. A polybutadiene (M_n= 4,200 g/mol) end-terminated with carboxyl or hydroxyl groups (which hydrogen bond to the clay surface) was used. As the intercalation/exfoliation proceeded in

time, the viscosity and relaxation times of the composite steadily increased. Within minutes, the self-exfoliation caused a transformation from a viscoelastic liquid with suspended clay particles to a viscoelastic solid with exfoliated clay sheets.[210,211] The exfoliation mechanism definitely required bonding between the polymer and clay.[212] Without such bonding, when embedding the organo-clay in polybutadiene without functional end groups, the clay maintained its original spacing (no intercalation or exfoliation) and showed minimal mechanical reinforcement. Clay exfoliation, which is a balance between several phenomena, has been shown to be effective in temperature ranges of 40-100°C with an optimum near 80°C.[210] Annealing temperatures must be high enough for the entropic telechelic polybutadiene to overcome the enthalpic energy barrier of clay stacking and to maintain high molecular mobility, but low enough to maintain the strength of hydrogen bonds between polymer and clay surfaces. Once the exfoliation was achieved, it remained stable within the polymer matrix at all accessible temperatures. Important for the success of the clay self-exfoliation process were several other conditions: polybutadiene is miscible with the counter ion's alkyl chain, its molecular weight is large enough to have molecular conformation controlled by entropy, but its molecular weight is small enough to guarantee high molecular mobility and a high density of functional end groups.[213] We were inspired by this earlier research on clay exfoliation and its fundamental understanding through a molecular model opened up the possibility of applying the same technique to 2D layered zeolites, to develop a facile exfoliation method.

In this study, we report the liquid exfoliation of layered MWW precursors with and without aluminum using commercially available liquid hydroxyl-terminated polybutadiene (HTPB). The specific interaction between HTPB macromolecules and the zeolite layered

precursors is utilized to allow HTPB to intercalate the precursors and, finally, exfoliate them into monolayers. This process successfully achieved the self-disassembly of ITQ-1, a pure silica layered precursor with MWW framework, in a liquid phase. Since no shearing force was applied during the exfoliation process, damage to the lateral size of the ITQ-1 nanosheets was kept at a minimum. The resulting ITQ-1 nanosheets of a high aspect ratio were transferred to an organic solvent where it formed a stable suspension. The exfoliation process for MCM-22, the aluminosilicate analog of ITQ-1, was also successful, but requires additional shearing. It was found that the presence of aluminum in the framework is unfavorable for the exfoliation. Also, the nature of the organic structure directing agent (OSDA) in the interlayer spacing plays an important role in the exfoliation process possibly by affecting the interaction between the polybutadiene and zeolite precursors. An uniform coating of ITQ-1 nanosheets on a sintered silica fiber (SSF) support was achieved by vacuum filtration. A successful gel-free secondary growth was performed on this coating by preserving its preferred orientation.

4.2. Experimental details

4.2.1. Synthesis of MCM-22(P)

MCM-22 precursor, MCM-22(P), was synthesized using a reported method.[193] 0.072 g of sodium aluminate (Sigma Aldrich) and 0.248 g of sodium hydroxide (Fisher Scientific) were dissolved in 31.10 g of distilled water. 1.91 g of hexamethyleneimine (HMI) (Sigma Aldrich) and 2.36 g of fumed silica (Cab-O-Sil M5) were then added to the mixture. The resulting gel composition was SiO_2: 0.5 HMI: 0.022 $NaAlO_2$: 0.158 NaOH: 44 H_2O. The mixture was stirred at room temperature for 5 h, followed by hydrothermal

synthesis in a Teflon-lined stainless steel autoclave with a rotation of 8 rpm at 135 °C for 11 days. The obtained crystalline product was collected by centrifugation and repeatedly washed by distilled water until the pH of supernatant solution was reduced to 9.

4.2.2. Synthesis of ITQ-1(P)

ITQ-1 layered precursor, ITQ-1(P), was synthesized using a reported method.[168] 0.389 g of sodium chloride (Fisher) was dissolved in 21.12 g of distilled water. 7.04 g of 25 wt.% aqueous solution of trimethyladamantammonium hydroxide (TMAdaOH) (SACHEM Inc.), 1.024 g of hexamethyleneimine (HMI) (Sigma Aldrich) and 2.00 g of fumed silica (Cab-O-Sil M5) were then added to the mixture. The resulting gel composition was SiO_2: 0.25 TMAdaOH: 0.31 HMI: 0.20 NaCl: 44 H_2O. The mixture was stirred at room temperature for 5 h, followed by hydrothermal synthesis in a Teflon-lined stainless steel autoclave with a rotation of 16 rpm at 150 °C for 11 days. The obtained crystalline product was collected by centrifugation and repeatedly washed by distilled water until the pH of the supernatant solution was reduced to 9.

4.2.3. Synthesis of ITQ-1-Al(P)

For the synthesis of ITQ-1-Al(P), 0.35 g of sodium chloride (Fisher) and 0.054 g of sodium aluminate (Sigma Aldrich) were dissolved in 21.12 g of distilled water. 7.04 g of 25 wt.% aqueous solution of trimethyladamantammonium hydroxide (TMAdaOH) (SACHEM Inc.), 1.024 g of hexamethyleneimine (HMI) (Sigma Aldrich) and 2.00 g of fumed silica (Cab-O-Sil M5) were then added to the mixture. The resulting gel composition was SiO_2: 0.25 TMAdaOH: 0.31 HMI: 0.02 $NaAlO_2$: 0.18 NaCl: 44 H_2O. The mixture was stirred at room temperature for 5 h, followed by hydrothermal synthesis in a Teflon-lined

stainless-steel autoclave with a rotation of 16 rpm at 150 °C for 11 days. The obtained crystalline product was collected by centrifugation and repeatedly washed by distilled water until the pH of the supernatant solution was reduced to 9.

4.2.4. Swelling of MCM-22(P), ITQ-1(P) and ITQ-1-Al(P)

The zeolite precursors were swollen with cetyltrimethylammonium bromide (CTAB) at room temperature following a reported procedure.[193] 9.0 g of aqueous slurry of the zeolite precursor (20 wt.% solids) was mixed with 35.0 g of an aqueous solution of 29 wt.% CTAB (Research Organics Inc.) and 11.0 g of an aqueous solution of 40 wt.% tetrapropyl ammonium hydroxide (Alfa Aesar). The mixture was stirred at room temperature for 16 h. The particles were then recovered by 15 cycles of centrifugation and washing with distilled water so that the pH of the supernatant solution was gradually reduced to 9. The resulting swollen material was dried overnight in an oven at 70 °C.

4.2.5. Exfoliation of MCM-22(S)

Hydroxyl-terminated polybutadiene, HTPB, average M_n =2800 g/mol from Sigma Aldrich, was used in the exfoliation process. 10 wt% MCM-22(S) was first gently hand-mixed for 1 min with HTPB using a spatula. The MCM-22(S)/HTPB was subjected to chaotic flow treatment in a planetary mixing system (FlackTek SpeedMixer DAC 150). The combination of gravitational forces in different planes enables efficient shearing and mixing of the suspension. The chaotic flow is achieved by adding four cylindrical ceramic pebbles (h = 10.0 mm, r = 4.80 mm) into the zeolite/polymer suspension. A rotational speed

of 3000 rpm was used in 2 min cycles followed by a 1 min cooling. The MCM-22(S)/HTPB mixture was subjected to 36 min of chaotic flow treatment.

4.2.6. Exfoliation of ITQ-1(S)

10 wt% ITQ-1(S) was added to HTPB and gently hand-mixed for 1 minute using a spatula.

4.2.7. Synthesis of ITQ-1(P) in fluoride medium

ITQ-1(P) was synthesized by first preparing a dry gel. 24.66 g of tetraethoxysilane (Alfa Aesar) was added to 6.25 g of 25 wt% trimethyladamantammonium hydroxide, TMAdaOH (SACHEM Inc.). The mixture was stirred at room temperature to evaporate water. The composition of the dry gel was SiO_2: 0.25 TMAdaOH: 0.9 H_2O. 1.18 g of hexamethyleneimine, HMI (Sigma Aldrich) and 1.02 g of water and NaCl (amount determined by the desired final gel composition) was added to 5 g of this dry gel. 0.8 g of hydrofluoric acid (48% aqueous, Alfa Aesar) was added to this mixture. The final gel composition was SiO_2: 0.5 HF: 0.25 TMAdaOH: 0.31 HMI: x NaCl: 3 H_2O. The amount of NaCl was varied such that x = 0, 0.05, 0.1, 0.2. The gel was transferred to a Teflon-lined stainless-steel autoclave and hydrothermal synthesis was carried out with a rotation of 16 rpm at 150°C for 11 days. The obtained crystalline product was collected by centrifugation and repeatedly washing with distilled water until the pH of the supernatant solution was reduced to 9. The sample was swollen by the method described earlier.

4.2.8. Synthesis of MCM-56(P)

MCM-56(P) was synthesized using a reported procedure.[214] 0.212 g of sodium hydroxide (NaOH, Sigma Aldrich) and 0.3275 g of sodium aluminate ($NaAlO_2$, Sigma Aldrich) were added to 14.4 g of DI water and allowed to dissolve. 3 g of fumed silica (Cab-O-Sil, M5) and 1.4875 g of hexamethyleneimine (HMI, Sigma Aldrich) were added to this solution under stirring. The final gel composition was SiO_2: 0.04 Al_2O_3: 0.093 Na_2O: 0.3 HMI: 16 H_2O. The gel was then transferred to a Teflon liner of a stainless-steel autoclave. Hydrothermal synthesis was carried out with a rotation of 16 rpm at 145 °C for various time durations ranging from 36 to 72 h. The obtained crystalline product was collected by centrifugation and repeatedly washing with distilled water until the pH of the supernatant solution was reduced to 9. The sample was swollen by the method described earlier.

4.2.9. Synthesis of 500 nm and 50 nm Stöber silica particles

500 nm and 50 nm Stöber silica particles were synthesized using a reported procedure. Tetraethyl orthosilicate (TEOS, 99%, Alfa Aesar), ammonia solution (32 wt%, Millipore), water and ethanol (200 proof, Fisher) were mixed in a stoichiometric proportion. For the synthesis of 500 nm particles, 473.4 g of EtOH were mixed with 81.99 g of TEOS in beaker A. 473.4 g of EtOH, 160.9 g of H_2O and 272.2 g of NH_3 solution were mixed in beaker B. Contents of each beaker were stirred after 10 min. After this, contents of beaker A were added to beaker B at a rate of 40 mL min^{-1}. After stirring for 3 h, the Stöber silica particles were precipitated by centrifugation. For the synthesis of 50 nm particles, 111.3 g of EtOH and 17.2 g of TEOS were mixed in beaker A. 111.3 g of EtOH,

78.2 g of H_2O and 2.1 g of NH_3 solution were mixed in beaker B. The contents of each beaker were stirred for 10 min. After this, contents of beaker A were added to beaker B instantaneously. After stirring for 3h, the Stöber silica particles were precipitated by centrifugation. Both particles were dried in a 70 °C oven overnight.

4.2.10. Synthesis of sintered silica fiber (SSF) supports

Sintered silica fiber (SSF) supports were prepared by a reported procedure.[179] Silica fibers (quartz wool) were purchased from Technical Glass Products (FQ wool, 4 μm fine wool). Since silica fibers are fluffy material, their compaction leads to a disk with a non-uniform density. To obtain a uniform disk, the silica fibers were powdered using a hydraulic press (MTI Corporation) in a die with diameter 22 mm and pressing force of 15 MPa for 60 sec. 1.7 g of quartz powder was mixed with 12 drops of 0.5 wt% solution of polyvinyl alcohol (PVA, 98-99% hydrolyzed, low molecular weight, Alfa Aesar) in water. PVA acts as a binder and provides mechanical strength to the supports. After mixing, the quartz powder was pressed in the die with pressing force of 15 MPa for 30 sec. The support is then heat treated at 1100 °C for 4 h, with heating and cooling rates of 2 °C min^{-1} and 4 °C min^{-1} respectively. Then, the SSF supports were polished with a SiC grinding paper (CarbiMet, 600 grit, P1200, Buehler). The polished supports were then washed with DI water and then used for coating layers of Stöber silica particles.

To coat the support with 500 nm Stöber silica particles, the SSF supports were washed with DI water. Excess DI water was removed using a dry tissue paper (Kimwipe), thereby leaving the supports in a partially wet state. Following this, the surface of the supports was manually rubbed with Stöber silica particles. A Teflon tape was used as a

smooth surface for this and subsequent rubbing steps. Post-rubbing, the supports were dried at 70 °C for 4h, and heat treated for 1100 °C for 3 h, with heating and cooling rates of 2 °C min^{-1} and 4 °C min^{-1} respectively. The rubbing process for each support was repeated 7 times to reduce the surface roughness.

The 500 nm silica-modified SSF supports were then coated with a layer of 50 nm Stöber silica particles by a similar rubbing process. In this case, rubbing was carried out only once. Post-rubbing, the supports were dried at 70 °C for 4h, and heat treated for 400 °C for 3 h, with heating and cooling rates of 2 °C min^{-1} and 4 °C min^{-1} respectively.

4.2.11. Coating of nanosheets on SSF supports

To prepare the ITQ-1 nanosheet suspension, 0.3 g of ITQ-1(S)/HTPB mixture was dissolved in 5 mL toluene. The solution was centrifuged at 5000 rpm for 10 min. The supernatant was collected and used for coating the SSF supports. 10 mL of the suspension was coated on a SSF support by vacuum filtration. The nanosheet-coated supports were dried at 150 °C for 6 h and then heat treated at 500 °C for 6 h with both heating and cooling rates of 1 °C min^{-1}.

4.2.12. Gel-free secondary growth

The ITQ-1 nanosheet-coated support was used for gel-free secondary growth. For this, the ITQ-1 nanosheet coated supports were first impregnated with an aqueous solution of 0.3 M TMAdaOH and 0.3 M HMI. The impregnation was carried out by simply soaking the nanosheet-coated support in the solution for 1 min. Post-soaking, excessive solution on the surface of the supports was removed by gently placing the periphery of the support on

a dry tissue paper. The gel-free growth was performed by sealing the impregnated support in a Teflon-lined stainless-steel autoclave (50 mL volume), followed by heating at 150 °C for 48 h. Calcination of the secondary grown films was carried out at 450 °C for 4 h with both heating and cooling rates of 0.5 °C min^{-1}.

4.2.13. Synthesis and exfoliation of multilamellar MFI

Multilamellar MFI (ml-MFI) was synthesized using a reported procedure.[168] $[C_{22}H_{45}\text{-}N^{+}(CH_3)_2\text{-}C_6H_{12}\text{-}N^{+}(CH_3)_2\text{-}C_6H_{13}]Br_2$, $C_{22\text{-}6\text{-}6}Br_2$, was synthesized by alkylation of N,N,N',N'-tetramethyl-1,6-hexanediamine (TCI Chemicals) with 1-bromodocosane (TCI chemicals) at 70 °C. The resultant product was alkylated by 1-bromohexane (Alfa Aesar) at 85 °C. $C_{22\text{-}6\text{-}6}Br_2$ was ion-exchanged with Amberlyst A-26(OH) resin (Alfa Aesar) to obtain $C_{22\text{-}6\text{-}6}(OH)_2$. Ml-MFI was synthesized by hydrolyzing tetraethyl orthosilicate (Alfa Aesar) in presence of $C_{22\text{-}6\text{-}6}(OH)_2$ and distilled water to obtain a gel composition of 100 SiO_2: 15 $C_{22\text{-}6\text{-}6}(OH)_2$: 4000 H_2O: 400 C_2H_5OH. The gel was stirred at room temperature for 24 h and then transferred to a Teflon-lined stainless steel autoclave. Crystallization was carried out at 150 °C for 5 days. The product obtained by centrifugation was washed with distilled water until the pH of supernatant solution was reduced to 9, and then dried overnight in an oven at 70 °C.

For exfoliation, hydroxyl-terminated polybutadiene, HTPB, average M_n =2800 g/mol from Sigma Aldrich, was used. 10 wt% ml-mFI was first gently hand-mixed for 1 min with HTPB using a spatula. The MCM-22(S)/HTPB was subjected to chaotic flow treatment in a planetary mixing system (FlackTek SpeedMixer DAC 150). The combination of gravitational forces in different planes enables efficient shearing and

mixing of the suspension. The chaotic flow is achieved by adding four cylindrical ceramic pebbles (h = 10.0 mm, r = 4.80 mm) into the zeolite/polymer suspension. A rotational speed of 3000 rpm was used in 2 min cycles followed by a 1 min cooling. The ml-MFI/HTPB mixture was subjected to 36 min of chaotic flow treatment.

4.2.14. Characterization

Small-angle X-ray (SAXS) scattering data was obtained using a SAXSLAB's Ganesha instrument with a Cu-Kα radiation source at a sample-to-detector distance of 441 mm. Powder X-ray diffraction patterns were collected on a PANalytical X'Pert Pro instrument with a Cu-Kα radiation source in the 2θ range of 4° to 32°. Transmission electron microscope (TEM) images of the zeolite nanosheets were measured with a JEOL JEM-2200FS instrument at 200 kV. 0.3 g of the zeolite/polybutadiene mixture after exfoliation was dissolved in 5 mL of toluene and centrifuged for 10 min at 6000 rpm. The supernatant was collected for TEM observation. To prepare the TEM samples, a drop of the supernatant was deposited on a copper grid (Lacey carbon film, Cu 300 mesh, Electron Microscopy Sciences), and dried in air. Scanning electron microscope (SEM) images were collected using FEI Magellan 400 XHR-SEM operated at 3.0 kV. The samples were sputter-coated with platinum before imaging. Atomic force microscopy (AFM) measurements on the nanosheets were performed on an Asylum Research Cypher ES (Oxford instruments) using a non-contact cantilever (Budget Sensors Tap300Al-G; k = 40 N/m, f= 300 kHz) in tapping mode. To prepare the samples, a drop of the nanosheet suspension in toluene was deposited on a mica disc (MTI Corporation, 9.9 mm diameter). The polymer was removed from the sample by calcining at 540 °C for 6 h in air flow with

a flow rate of 472 mL/min. NMR experiments were run in a MAS solid-state Bruker 600 MHz with ^{13}C direct polarization frequency with a rotor spinning rate of 6 kHz at ambient temperature. About 20 - 30 mg of the samples were packed into a 4 mm ZrO_2 rotor with a Kel-F cap. Frequency were tuned to 151.2 MHz for ^{13}C. NMR experiments were run with a $\pi/2$ rf pulse with 4 μs duration to ^{13}C frequency, with 2 s recycle delay. 512 scans were typically enough to ensure all peaks were sufficiently resolved. Peak deconvolutions and relative peak areas were obtained using OriginPro 2017. Rheological measurements were performed on a stress-controlled Malvern Kinxeus Pro+ with a 20-mm parallel plate fixture. Time resolved mechanical spectroscopy (TRMS) was performed at 25ºC with continual frequency sweeps (ω = 1-100 rad/s) for 4 hours. After having reached a stable steady state, small amplitude oscillatory shear (SAOS) master curves were constructed from frequency sweeps at a strain amplitude of 0.2% from -10 ºC to 40 ºC in 10 ºC increment. Finally, shear orientation of the exfoliated sheets was performed by applying a shear rate 5 s^{-1} for 5 min.

4.3. Results and discussion

4.3.1. Exfoliation of MCM-22(P)

MCM-22(P) is the aluminosilicate 2DZ layered precursor with MWW framework. MCM-22(P) with a layered structure was synthesized using hexamethyleneimine as a structure directing agent. The SAXS scattering profile of the synthesized MCM-22(P) sample shows (001) and (002) diffraction peaks from a lamellar phase indicating that the material exhibits a layered structure (Fig. 4.17a). MCM-22(S) was synthesized by swelling MCM-22(P) using cetyltrimethyl ammonium bromide (CTAB) under mild conditions. The

SAXS scattering profile shows a shift of the (001) diffraction peak to a lower angle, indicating that the swelling caused an increase in the interlayer d-spacing to 4.6 nm (Fig. 4.17a). This result supports that the CTAB molecules diffuse into the MCM-22(P) layers increasing the interlayer spacing. Meanwhile, the diffraction peaks associated with the crystalline MWW framework were not changed during the swelling process as shown in the XRD pattern (Fig. 4.17a), indicating that the crystalline structure of MCM-22 sheets was retained. The observations are consistent with the previous report on swelling of MCM-22(P) using CTAB.[193] For the exfoliation of the layered zeolite precursors, MCM-22(S) was mixed with HTPB and subjected to a chaotic flow for 36 min. After the flow treatment, the resultant sample transformed from a dispersion of visual aggregates to a transparent solution (Fig. 4.18). The (001) diffraction peak disappeared from the SAXS profile of the resultant suspension, indicating the successful exfoliation of MCM-22(S) (Fig. 4.17a).[215] It is important to note that the (100) diffraction peak, the characteristic peak of the MWW framework, remains unaffected after both the swelling and chaotic flow steps, confirming the retention of the crystalline structure of the zeolite. The SEM images of MCM-22(P) and MCM-22(S) are shown in Fig. 4.19. The scheme for the exfoliation of MCM-22(P) is summarized in Fig. 4.20.

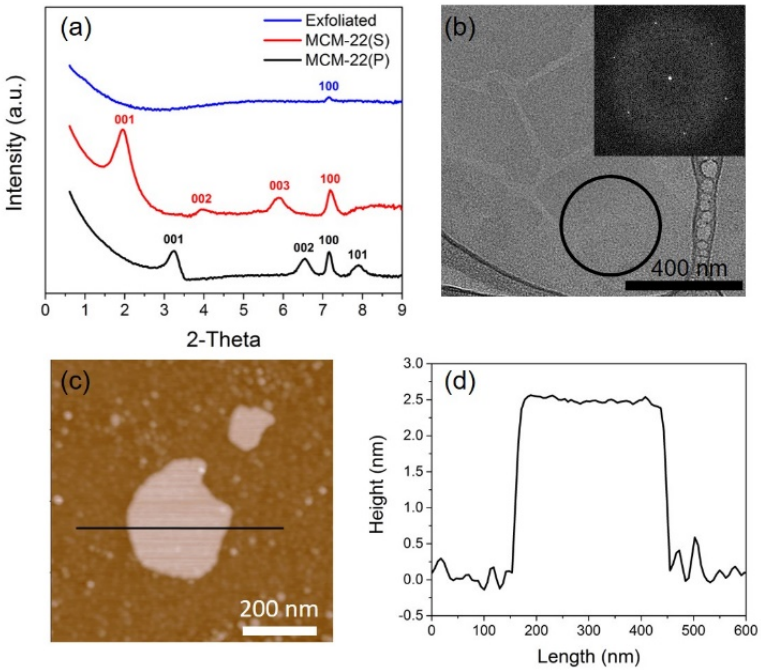

Figure 4.17 (a) SAXS profiles of MCM-22(P), MCM-22(S) and MCM-22(S)/HTPB mixture after 36 min of chaotic flow treatment, (b) TEM image of MWW nanosheet obtained and (inset) the Fast Fourier Transform (FFT) of the nanosheet, (c) an AFM (tapping mode) topographic image of MWW nanosheet of mica disc and (d) line profile analysis of the topographic height along the line scan of the MWW nanosheet shown in (c).[215]

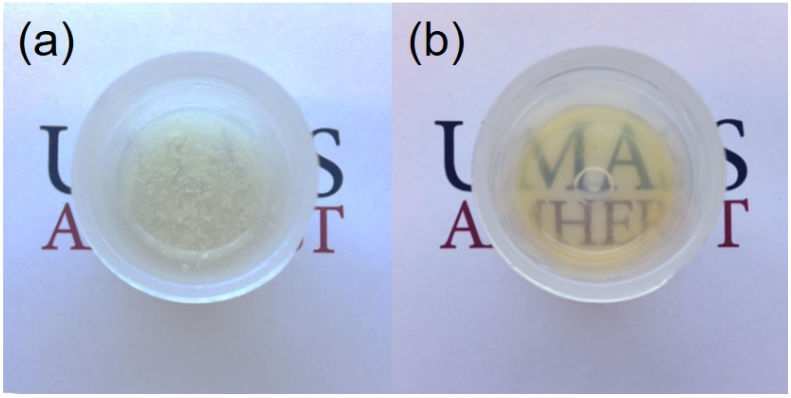

Figure 4.18 MCM-22(S)/HTPB mixture (a) after manually mixing for 1 min and (b) after 36 min of chaotic flow treatment.

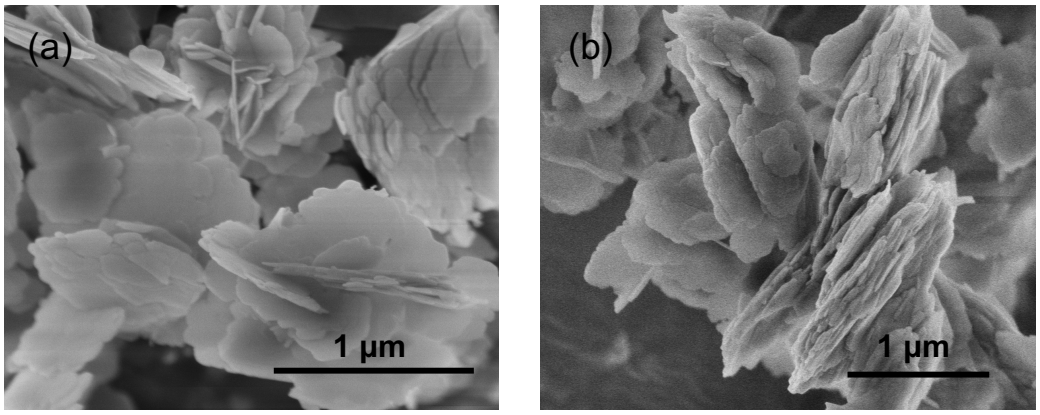

Figure 4.19 SEM images of (a) MCM-22(P) and (b) MCM-22(S)

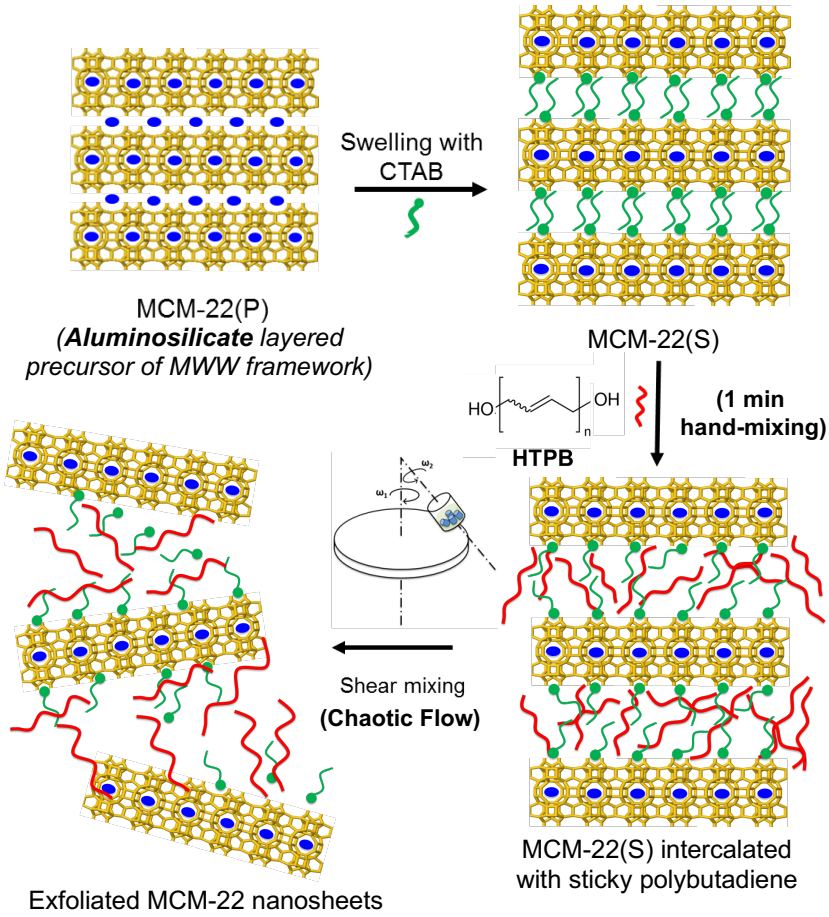

Figure 4.20 Schematic depiction of exfoliation of MCM-22(P) using HTPB

The exfoliated MCM-22(S) was dispersed in toluene for further characterization. The dispersion was then centrifuged to isolate the exfoliated nanosheets from the partially exfoliated ones. After the centrifugation, the supernatant containing the fully exfoliated nanosheets was collected and used for TEM and AFM characterization. TEM image of the purified solution shows the presence of 2D nanosheets with a crystalline structure (Fig. 4.17b). The thickness of the nanosheets was characterized using AFM which showed a uniform nanosheet thickness of 2.5 ± 0.3 nm (Fig. 4.17c and d), which is consistent with the previously reported thickness of MWW nanosheets, suggesting that the sheets are single-layer thick.[193]

It was found that the end-groups of the liquid polybutadienes play a critical role in the exfoliation of MCM-22(S). HTPB (hydroxyl group), CTPB (carboxyl group) and PB (non-functionalized) were used for the exfoliation of MCM-22(S), respectively. SAXS profiles of the resultant suspensions after the chaotic flow treatment is shown in Fig. 21a. It was found that PB was completely ineffective in exfoliating MCM-22(S), whereas CTPB is only able to intercalate MCM-22(S) increasing its d-spacing to about 9.8 nm. HTPB was found to be the most effective as evidenced in the complete disappearance of the (001) peak after 36 min of the chaotic flow treatment. The end-groups of liquid polybutadienes affect both intercalation and exfoliation processes. This might be due to different interactions between the end-groups of the polymer chain and the polar surface of the zeolite or the organic modifier (i.e. CTAB). There are mainly two dominant interactions critical for the intercalation and exfoliation of the 2D zeolite precursors, polar interaction between the end-groups of polybutadiene and the head group (trimethylammonium cation, $N(CH_3)_3^+$) of CTAB, and hydrogen bonding formed either between polybutadiene and

CTAB or between the end-groups of polybutadiene and the oxygen basal plane as well as silanol groups of the zeolites. Polybutadiene without any functional end-groups (i.e. PB) fails to interact with the zeolite and CTAB, thus cannot contribute to the intercalation and exfoliation processes. Both HTPB and CTPB are end-functionalized with polar end groups and thus are able to hydrogen bond, unlike PB. A similar effect has been previously reported in the case of exfoliation of montmorillonite organoclay, for which only end-functionalized polybutadiene was able to exfoliate the clay.[209] In the case of zeolites, we observed that HTPB is more effective than CTPB for the exfoliation of MCM-22(S). This may stem from the difference in polarity between hydroxyl and carboxyl end groups, with carboxyl groups having a stronger ability to hydrogen bond. This would indicate that CTPB interacts more strongly with the head group of CTAB than with the zeolite surface. On the other hand, HTPB, with a less polar end-group, preferentially interacts with the zeolite surface by hydrogen bonding. When the polymer strongly attaches itself to the zeolite layers, it can push the layers apart effectively, resulting in the exfoliation of the zeolites during the flow treatment. The intercalation may relate to the gyration radius of the polymers and the polymer's configuration within the interlayer spacing of the zeolite, and requires further study.

The effect of flow treatment time on the exfoliation was also studied. Interestingly, the SAXS results (Fig. 4.21b) show a shift of the (001) diffraction peak to a lower angle after mixing MCM-22(S) with HTPB for 1 min without any flow treatment. This suggests that the mild mixing is sufficient for the intercalation of MCM-22(S) with HTPB, thereby increasing the interlayer d-spacing to about 9.4 nm. Increasing the chaotic flow treatment

time leads to a decrease in the intensity of the (001) diffraction peak, finally resulting in the complete disappearance of the peak at 36 min.

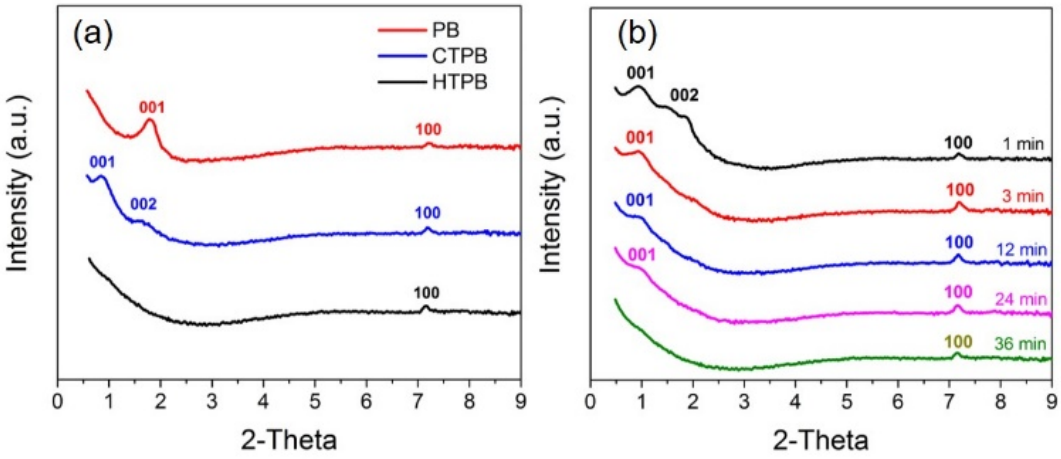

Figure 4.21 (a) SAXS profiles of mixtures of MCM-22(S) with HTPB, CTPB and PB, after 36 min of chaotic flow treatment, (b) SAXS profiles of MCM-22(S)/HTPB mixture after 1 min of gentle hand-mixing and at various durations of chaotic flow treatment from 3 min to 36 min.

To compare the effectiveness of sonication treatment with flow treatment, 10 wt% of MCM-22(S) was mixed in HTPB and subjected to sonication in a bath sonicator. The SAXS results (Fig. 4.22) reflect a decrease in the (001) peak intensity after 5 h of sonication, as compared to that after 2 h of sonication. This suggests that sonication is also effective in exfoliating the layered zeolite precursors, but requires a longer time than flow treatment.

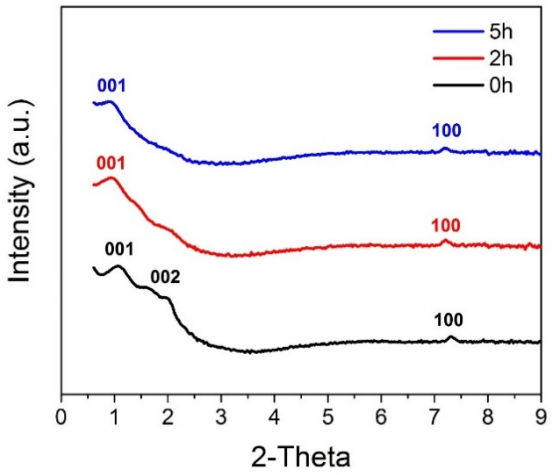

Figure 4.22 SAXS profiles of MCM-22(S)/HTPB mixture of 1 min of hand-mixing and no sonication (0 h) ad after 2 h and 5 h of sonication

4.3.2. Exfoliation of ITQ-1(P)

ITQ-1(P) was synthesized by hydrothermal synthesis using hexamethyleneimine (HMI) and trimethyladamantammonium hydroxide (TMAdaOH) as the organic structure directing agents. The SAXS pattern of the synthesized ITQ-1(P) revealed (001) and (002) diffraction peaks indicating that the material exhibits a layered structure (Fig. 4.23a). ITQ-1(P) was swollen using CTAB under mild conditions to synthesize ITQ-1(S). During swelling, the CTAB molecules diffuse into the inter-layer spacing of ITQ-1(P), increasing the spacing. This is supported by the SAXS pattern, which shows a shift of the (001) peak to a lower angle, indicating an increase in the d-spacing to 3.7 nm. For exfoliation, the swollen precursor, ITQ-1(S) was hand-mixed with HTPB for 1 minute. It was observed that the (001) diffraction peak disappeared from the SAXS profile, indicating the successful exfoliation of ITQ-1(S). It is important to note that the (100) diffraction peak, a characteristic peak of the MWW framework, remains unaffected after this step. This

confirms the retention of the crystalline structure of the zeolite after exfoliation. The SEM images of ITQ-1(P) and ITQ-1(S) are shown in Fig. 4.24. The exfoliation scheme is summarized in Fig. 4.25.

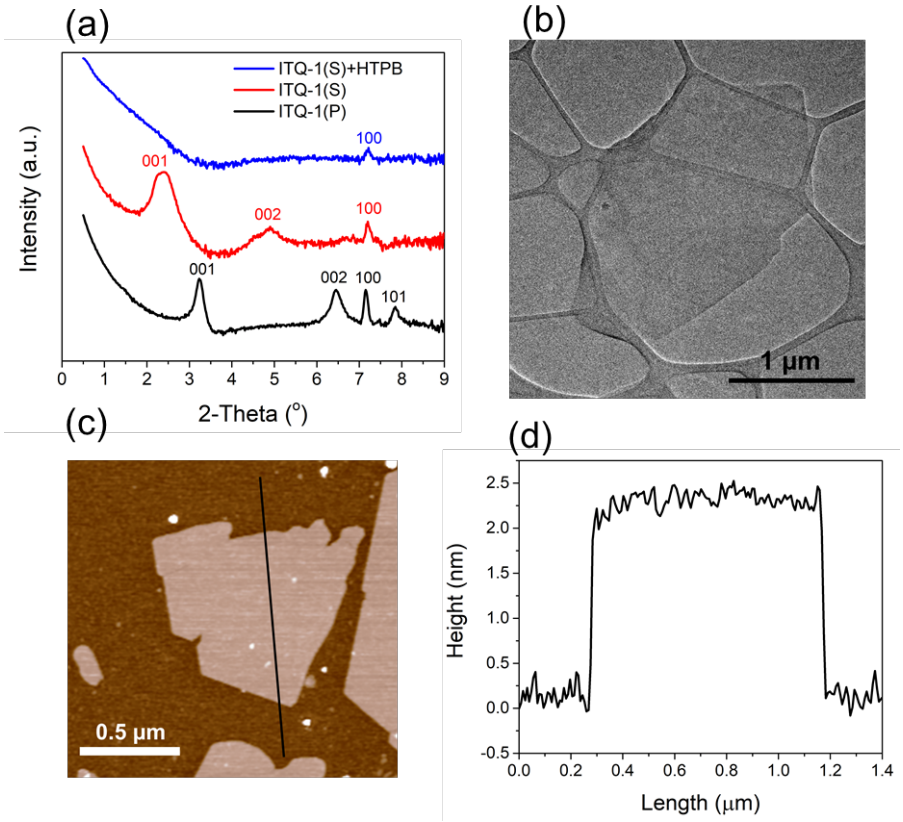

Figure 4.23 (a) SAXS profiles of ITQ-1(P), ITQ-1(S) and ITQ-1(S)/HTPB after 1 min of manual mixing, (b) TEM image of ITQ-1 nanosheets, (c) AFM (tapping mode) topographic image of ITQ-1 nanosheets supported on a mica disc, (d) line profile analysis of the topographic height along the line scan of the ITQ-1 nanosheet shown in (c)

The exfoliated ITQ-1(S)/HTPB mixture was dispersed in toluene and centrifuged to separate the exfoliated nanosheets from the unexfoliated ones. After centrifugation, the supernatant containing the exfoliated nanosheets was collected and used for TEM and AFM characterization. TEM images show the presence of exfoliated nanosheets (Fig. 4.23b). The thickness of the nanosheets was characterized using AFM, which showed a

uniform thickness of 2.4 ± 0.2 nm (Fig. 4.23 c and d), which is consistent with the reported thickness of MWW nanosheets, suggesting that the sheets are single-layer thick.[193] Using thermogravimetric analysis, it was found that 57% of the nanosheets are either single layer thick or partially exfoliated. ITQ-1 self-disassembles and does not require additional shear force for exfoliation.

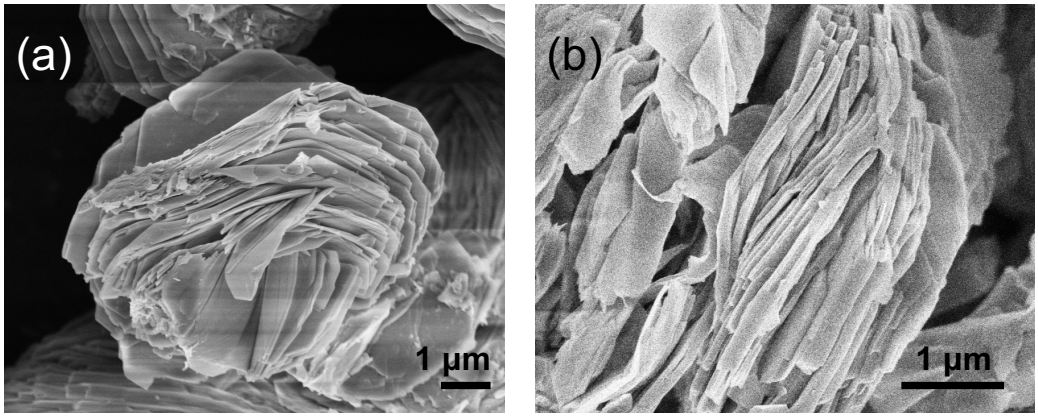

Figure 4.24 SEM image of (a) ITQ-1(P) and (b) ITQ-1(S)

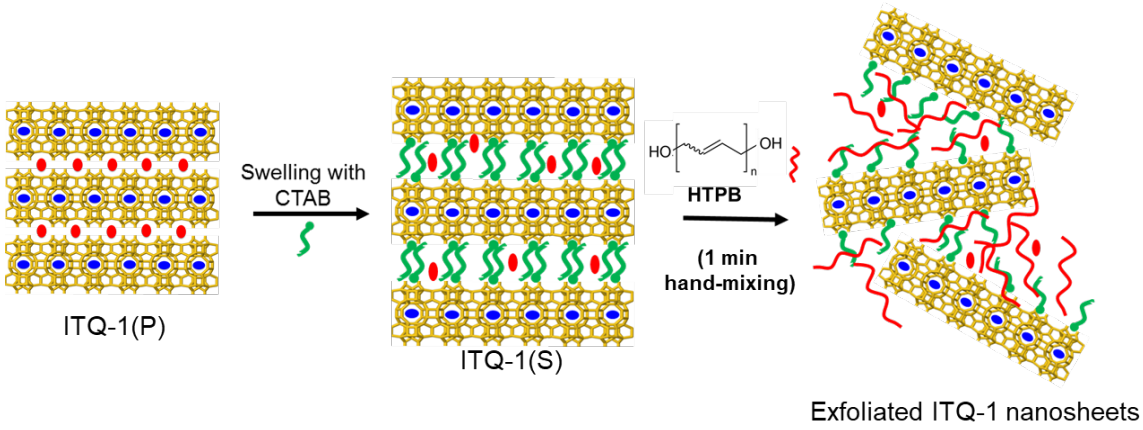

Figure 4.25 Schematic for the exfoliation of ITQ-1(P) using HTPB

The size of the ITQ-1 nanosheets is about 1 μm× 1 μm, which is much larger than the ones obtained by Varoon and coworkers[168] through melt-compounding of ITQ-1(S) with polystyrene at high temperature in a twin-screw extruder (Fig. 4.26). The self-disassembly process at room temperature reduced the probability of size-reduction of the nanosheets during exfoliation, resulting into relatively larger nanosheets. On the other hand, in the melt-blending process, the large shear forces and high energy input in the twin screw extruder results into lateral size reduction of the nanosheets.

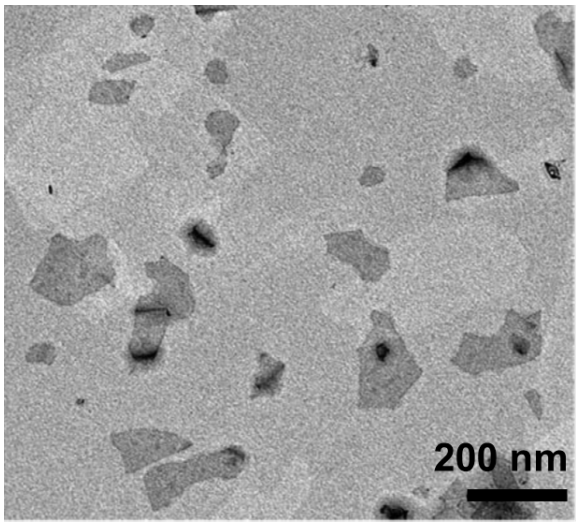

Figure 4.26 ITQ-1 nanosheets obtained by Varoon and coworkers after exfoliation using melt-blending[168]

MCM-22(S). the aluminosilicate analog of ITQ-1(S), could only be intercalated with HTPB, when hand mixed for 1 minute. Exfoliation required the mixture to be subjected to 36 min of chaotic flow treatment (Fig. 4.17a). The average size of the MCM-22 nanosheets is about 0.4 μm×0.4 μm (Fig. 4.27a), whereas the average size of the ITQ-1

nanosheets is about 1 μm× 1 μm (Fig. 4.27b), which indicates that the chaotic flow treatment plays a role in reduction of the lateral size of the nanosheets.

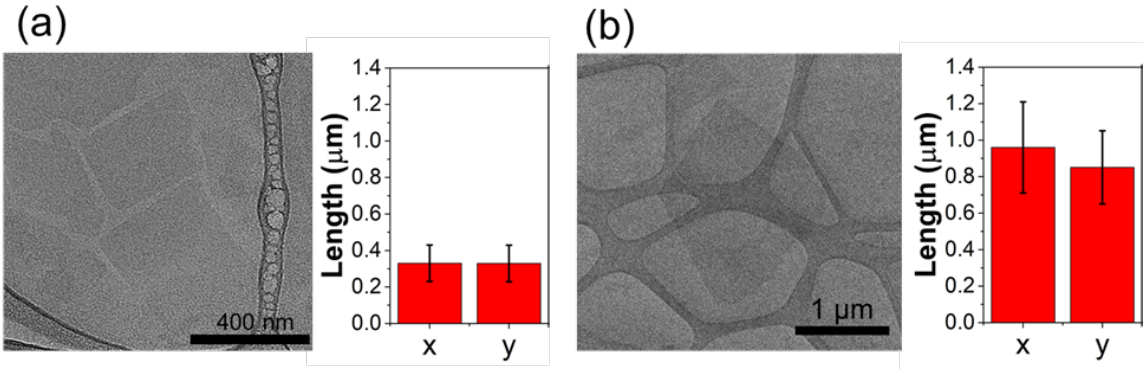

Figure 4.27 (a) TEM image of MCM-22 nanosheet and the average size of a nanosheet of x and y directions, (b) TEM image of ITQ-1 nanosheet and the average size of a nanosheet of x and y directions

4.3.3. Differences between MCM-22(P) and ITQ-1(P)

MCM-22(P) and ITQ-1(P) are both layered precursors of MWW framework, however, the two zeolites show distinctly different exfoliation behavior. Upon mixing with HTPB, ITQ-1(S) self-disassembles, whereas MCM-22(S) is only intercalated and requires further chaotic flow treatment (shear force) for exfoliation. The distinct exfoliation behavior may be due to the presence of the Al in the framework and/or the nature of the OSDA present in the interlayer spacing of the zeolites. MCM-22(P) is an aluminosilicate zeolite, whereas ITQ-1(P) is pure silica. In case of MCM-22(P), the OSDA present in the interlayer spacing is HMI, whereas in the case of ITQ-1(P), it is TMAdaOH.

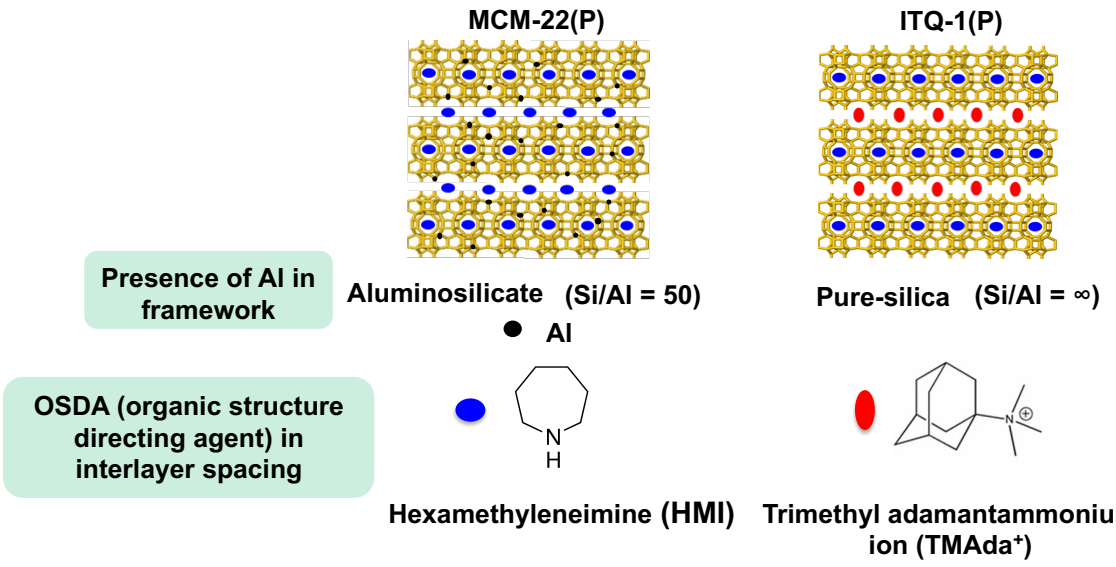

Figure 4.28 Schematic representation of the differences between MCM-22(P) and ITQ-1(P)

4.3.4. Effect of framework aluminum on exfoliation

In order to decouple the effects from the presence of aluminum in the framework and that from the OSDA, ITQ-1-Al(P), an aluminosilicate with MWW framework (Si/Al=50), was synthesized using both HMI and TMAdaOH as the structure directing agents. The presence of aluminum in the framework was confirmed using Inductively Coupled Plasma (ICP) and ^{27}Al MAS NMR. ITQ-1-Al(S) was obtained by swelling the precursor using CTAB under mild conditions. The SEM images of the precursor and swollen samples are shown in Fig. 4.29.

On hand-mixing ITQ-1-Al(S) with HTPB for one minute, the (001) peak shifts to a lower angle with a reduced intensity (Fig. 4.30), indicating intercalation of HTPB in in the interlayer spacing, which is similar to the case of MCM-22(S). Upon hand-mixing for another ten minutes, there is no change in the (001) peak position or intensity. The

existence of a low intensity (001) peak indicates that the layered precursor is only partially exfoliated, suggesting that the presence of aluminum in the framework is unfavorable for exfoliation. This result is in agreement with studies on the role of aluminum in the framework on the delamination of MCM-22(P) to ITQ-2.[216,217] It was observed that the delamination process is favored by decreasing the aluminum content in the parent material. A higher charge density at higher Al contents of the framework implied stronger interactions between the zeolite layers.

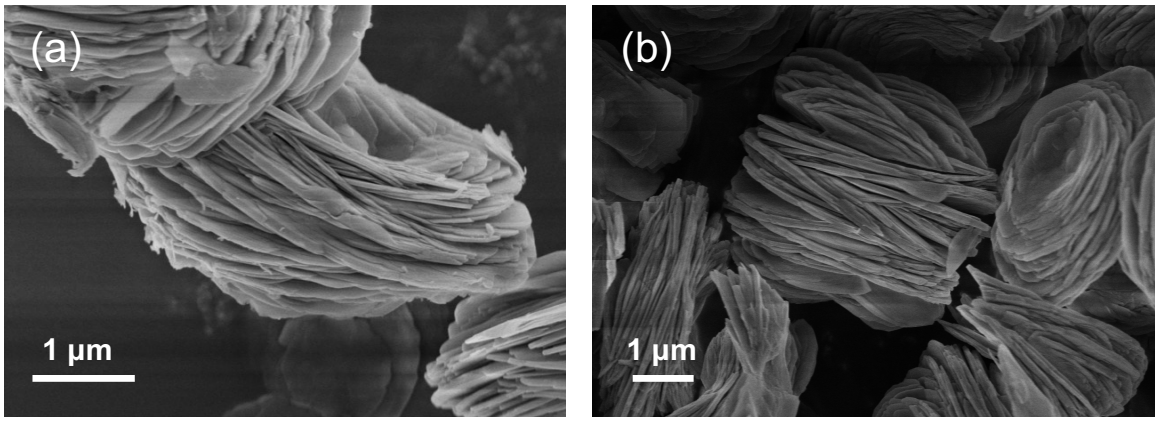

Figure 4.29 SEM images of (a) ITQ-1-Al(P) and (b) ITQ-1-Al(S)

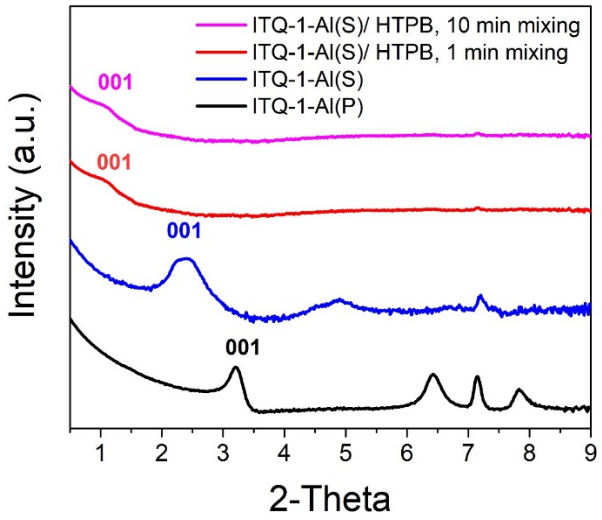

Figure 4.30 SAXS profiles of ITQ-1-Al(P), ITQ-1-Al(S) and ITQ-1-Al(S)/HTPB after 1 min of hand mixing and 10 min of hand mixing

4.3.5. Effect of interlayer OSDA on exfoliation

To study the effect of OSDAs present in the interlayer spacing of the 2DZ precursors on exfoliation, it is first essential to examine if the OSDA is retained in the interlayer spacing after the swelling treatment. To analyze this, ^{13}C MAS NMR was performed on the zeolite samples before and after the swelling treatment. The data is shown in Fig. 4.31. MCM-22(S) shows several peaks in the range from 10 ppm to 60 ppm. The two peaks at 48 ppm and 27 ppm are from the C_1 and C_3 carbons of HMI, respectively,[218] and other peaks are from the surfactant CTAB. HMI is present in the 10 MR sinusoidal channel (intralayer) as well as in the interlayer spacing of MCM-22(P).[218] The amount of HMI in MCM-22(P) and MCM-22(S) was calculated from the areas of peaks at 27 ppm and 48 ppm corresponding to HMI. It was found that the HMI in MCM-22(S) is 4.3 wt%, which is nearly equal to the amount of HMI present in the 10 MR sinusoidal channel. This result suggests that the HMI present in the interlayer spacing is washed off after the

swelling treatment. However, the HMI located in the 10 MR sinusoidal channel cannot be diffused out from the 10 MR windows during swelling.

In ITQ-1(P), peaks from HMI and $TMAda^+$ were observed. The peaks at 30 ppm corresponds to C_4, 35.5 ppm to C_3, C_2 and 48 ppm to C_1 of $TMAda^+$.[218] In ITQ-1(P), it has been reported that HMI is present in the 10 MR sinusoidal channel (intralayer) and $TMAda^+$ ions stabilize the 12 MR cups (interlayer).[218] The amount of HMI in ITQ-1(S) after swelling treatment is the same as before, suggesting that swelling step cannot remove HMI from ITQ-1(S),likely because HMI is located in the 10 MR sinusoidal channel and cannot diffuse out. The amount of $TMAda^+$ in ITQ-1(P) and ITQ-1(S) was calculated from the peak at 35.5 ppm corresponding to $TMAda^+$. It was found that 42% of the $TMAda^+$ in the interlayer spacing was removed from the sample during the swelling treatment.

Unlike ITQ-1(S), in the case of ITQ-1-Al(P), which contains aluminum, all the $TMAda^+$ stays in the interlayer space of the sample after swelling, indicating that $TMAda^+$ is more difficult to be removed from the interlayer spacing when aluminum is present in the framework. These results suggest that the exfoliation of both ITQ-1(S) and ITQ-1-Al(S) is more effective (requires less or no shear force) than MCM-22(S), which suggests that the presence of $TMAda^+$ ions in the interlayer spacing might favor exfoliation.

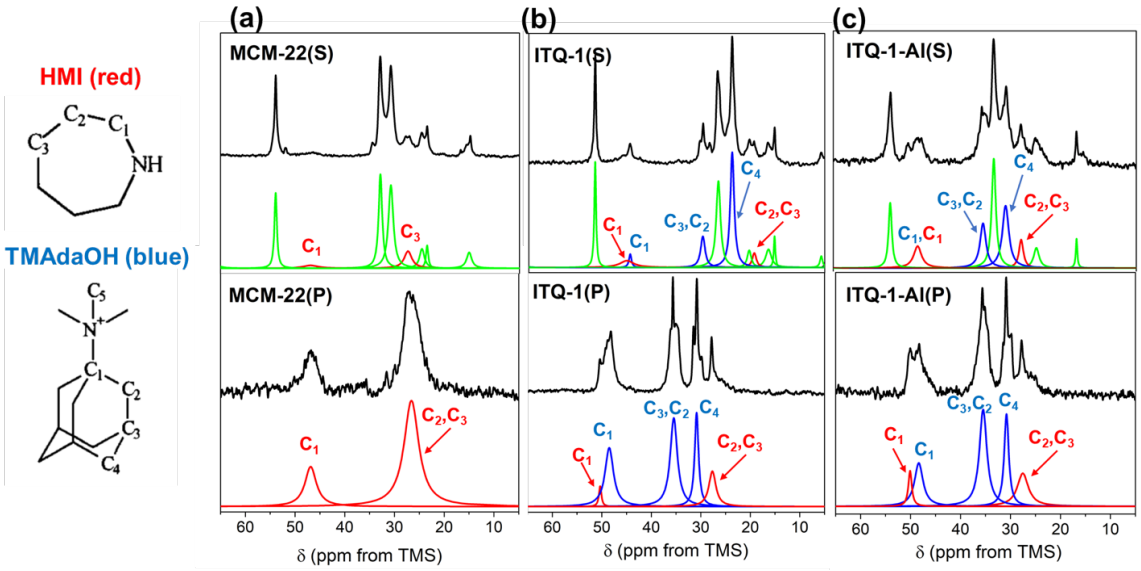

Figure 4.31 (a) ^{13}C MAS NMR spectra of MCM-22(P) and MCM-22(S). The peaks at 27 ppm and 48 ppm correspond to HMI. Comparison of the HMI peak areas from MCM-22(P) and MCM-22(S) indicate that all the HMI in the interlayer spacing is washed off after the swelling treatment. (b) ^{13}C MAS NMR spectra of ITQ-1(P) and ITQ-1(S). The 27.7 ppm peak corresponds to C_3 from HMI. The 35.5 ppm peak corresponds to C_2 from TMAda$^+$. Comparison of the ITQ-1(S) and ITQ-1(P) spectra indicate that 58% of TMAda$^+$ is retained in the interlayer spacing after the swelling treatment. (c) ^{13}C MAS NMR spectra of ITQ-1-Al(P) and ITQ-1-Al(S). Comparison of the ITQ-1(S) and ITQ-1(P) spectra indicate that all of TMAda$^+$ is retained in the interlayer spacing after the swelling treatment.

4.3.6. Rheology experiments to study zeolite-polymer interactions

The zeolite-polymer composite's rheological properties can be used to investigate the intercalation and exfoliation processes. To monitor the structure evolution, the linear viscoelastic properties were measured with small amplitude oscillatory shear (SAOS). ITQ-1(S) was gently mixed into the HTPB polymer matrix and the composite was immediately loaded into the rheometer before any major intercalation/exfoliation occurred. The gentle mixing had two purposes, maintaining the size of the fragile zeolite nanosheets and avoiding exfoliation to take place before measurement. The structure of the composite

evolved slow enough to be able to load the samples into the rheometer and so that the structure development could be observed by time resolved rheometry[219,220] at low Mutation Number values. The evolving dynamic moduli from the repeated frequency sweeps are shown as a function of time for ITQ-1(S)/HTPB (Fig. 4.32).

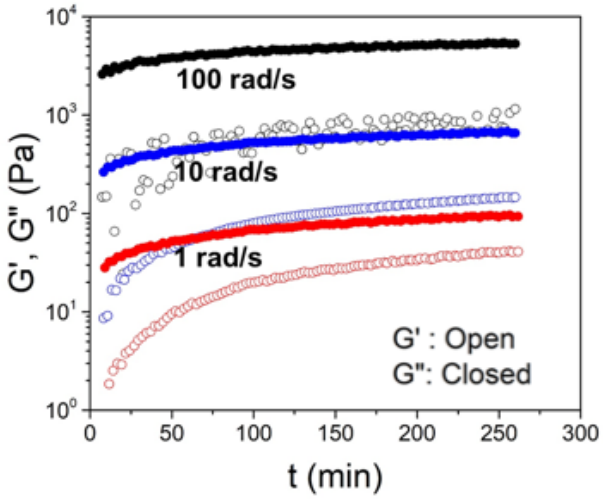

Figure 4.32 Frequency sweeps as a function of time to show the modulus growth of ITQ-1(S) when mixed with HTPB

An initial steep growth in G' indicates that the intercalation/exfoliation occurs in the composite. This rapid growth occurs even at room temperature. After approximately 1.5 hours, the time-dependent moduli tend to level off as a consequence of the structure reaching a steady-state. SAXS result suggests that the sample is exfoliated at this stage (Fig. 4.23a). Rheology data along with the SAXS data clearly indicates that the polymer HTPB interacts favorably with the zeolite..

Once the composite samples had reached a steady-state, a master curve was generated by performing SAOS frequency sweeps over a range of temperatures. Two

polymers were chosen to study their interactions with the zeolite nanosheets; hydroxyl-terminated polybutadiene (HTPB), having hydroxyl end-groups, and polybutadiene (PB) without end functional groups. The samples at steady state are considered equivalent to the samples obtained by 1 minute of hand-mixing the polymer with the zeolite. Fig. 4.33 compares SAOS master curves of three samples, ITQ-1(S)/PB, ITQ-1(S)/HTPB with neat PB and neat HTPB respectively. It was found that the addition of ITQ-1(S) to PB only had a negligible effect on G' and G''; ITQ-(S)/PB master curves match that of the neat PB. This indicates that PB does not interact with the zeolite, which is also confirmed by the unchanged (001) peak position in the SAXS data (Fig. 4.34). This is strongly contrasted by the linear viscoelastic (LV) response of ITQ-1(S)/HTPB; the composites moduli exceed the values of moduli for neat HTPB .This indicates that HTPB interacts favorably and strongly with the zeolite. This is confirmed by SAXS data. The disappearance of the (001) peak (Fig. 4.34) indicates that ITQ-(S) exfoliates in HTPB. These observations suggest that the polymer end group plays an important role in exfoliation of the zeolite. We hypothesize that a polymer with an end functional group attaches itself to the zeolite surface firmly and is able to push the layers apart effectively.

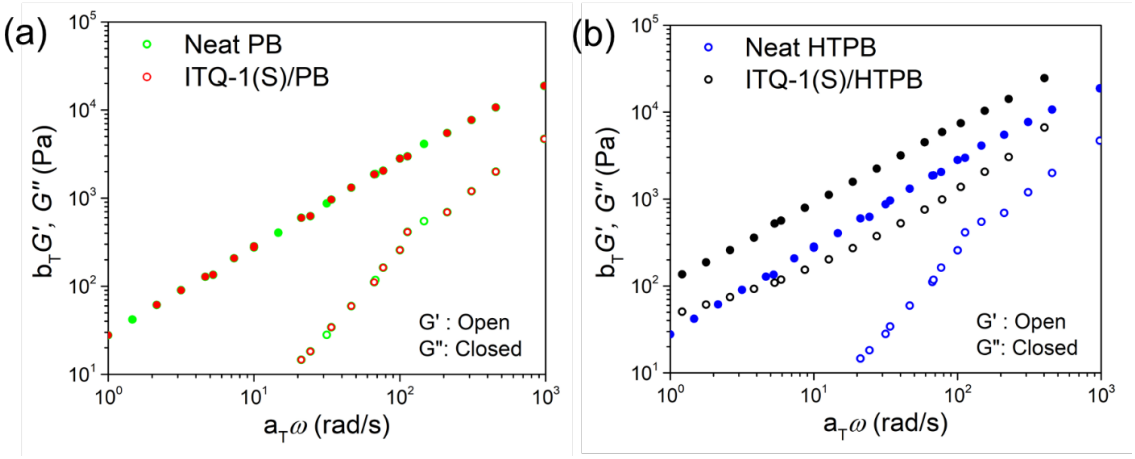

Figure 4.33 SAOS master curves for (a) ITQ-1(S)/PB and neat PB and (b) ITQ-1(S)/HTPB and neat HTPB

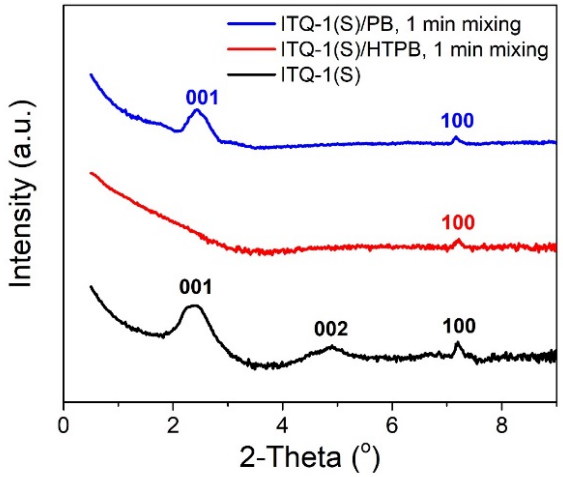

Figure 4.34 SAXS profiles of ITQ-1(S), ITQ-1(S)/HTPB and ITQ-1(S)/PB. HTPB, when mixed with ITQ-1(S), leads to exfoliation of the zeolite as indicated by the disappearance of the (001) peak. On the other hand, when PB is mixed with ITQ-1(S), it does not intercalate the zeolite.

A large shear strain was imposed on the ITQ-1(S)/HTPB composite (obtained after 1 min of hand-mixing) to determine if the structure was sensitive to shear. The LV responses of the ITQ-1(S)/HTPB composite before and after application of the shear are compared in Fig. 4.35a. We assume that hand-mixing of ITQ-1(S) in the polymer results

in a composite in which the ITQ-1 sheets are dispersed close to random. This is the initial condition of the sample for the large shear strain experiment. A decrease in the moduli was observed in SAOS after application of shear (Fig. 4.35a). This indicates a significant drop in the connectivity (particle-particle or polymer-polymer interactions) presumably due to shear orientation. The shear-oriented sample was left in the rheometer for over 2 hours and no recovery in modulus was observed. We speculate that the sheets are oriented parallel to the shear planes (Fig. 4.35b).[221] Such alignment is beneficial for applications requiring sheets that are oriented in a particular direction.

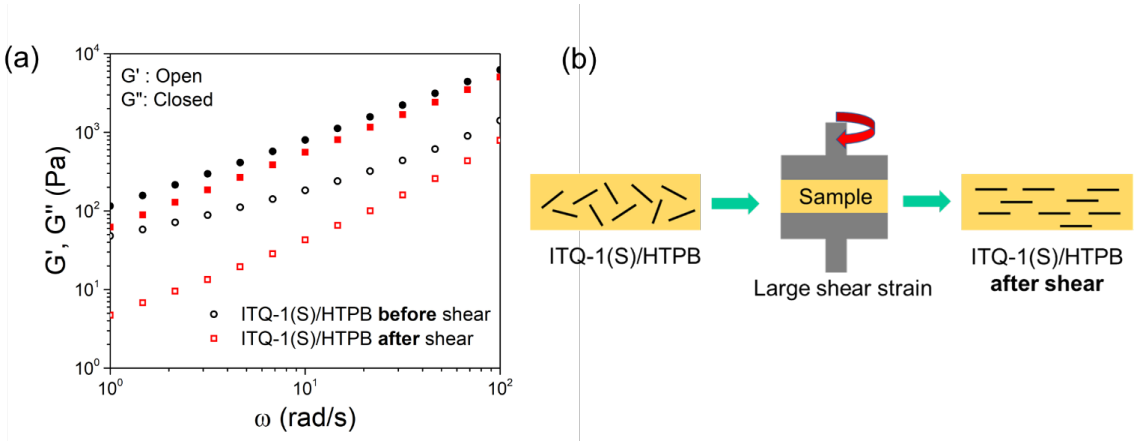

Figure 4.35 (a) SAOS master curves of ITQ-1(S)/HTPB composites before and after application of a large shear strain.

4.3.7. Synthesis and exfoliation of MCM-56(P)

MCM-56 is considered to be a unilamellar zeolite with MWW topology comprising layers stacked disorderly without interlayer connectivity, except for possible incidental silanol condensations.[222–227] It crystallizes as a distinct intermediate during the preparation

of the three dimensional MCM-49 (high Al-MWW) and must be intercepted at the right time in the course of synthesis. If quenched prematurely or too late, the MCM-56 monolayers end up contaminated with either unreacted amorphous solid or partially condensed (MCM-49), respectively.

Fig. 4.36 shows XRD profiles at various time intervals during the synthesis of MCM-49 at 150 °C. A relatively sharp peak near 2θ of 7.1° is assigned to (100) peak of the MWW framework. The XRD of MCM-56 is characterized by a broad band between 2θ of 8° and 10° without a dip, which is an indication of initial disorder in monolayer packing at shorter crystallization times. The emerging dip at longer crystallization times is an indication of the formation of a multilayer 3D structure, MCM-49. XRD of the sample intercepted after 42 h of synthesis has characteristics of MCM-56 (Fig. 4.36). The sample at 47 h shows a dip in the broad band between 8° and 10°, and hence is characterized as MCM-49.

The as-made precursor sample, MCM-56(P) was swollen using surfactant CTAB at room temperature. The SEM images of the precursor and the swollen sample are shown in Fig. 4.37. SAXS profiles of the precursor and swollen samples are shown in Fig. 4.38. Both samples show a (100) peak characteristic of the MWW framework structure, indicating that the structure was retained after the swelling treatment. The MCM-56(S) sample shows a peak at a lower angle ~1.8 ° indicating a swollen sample.[226]

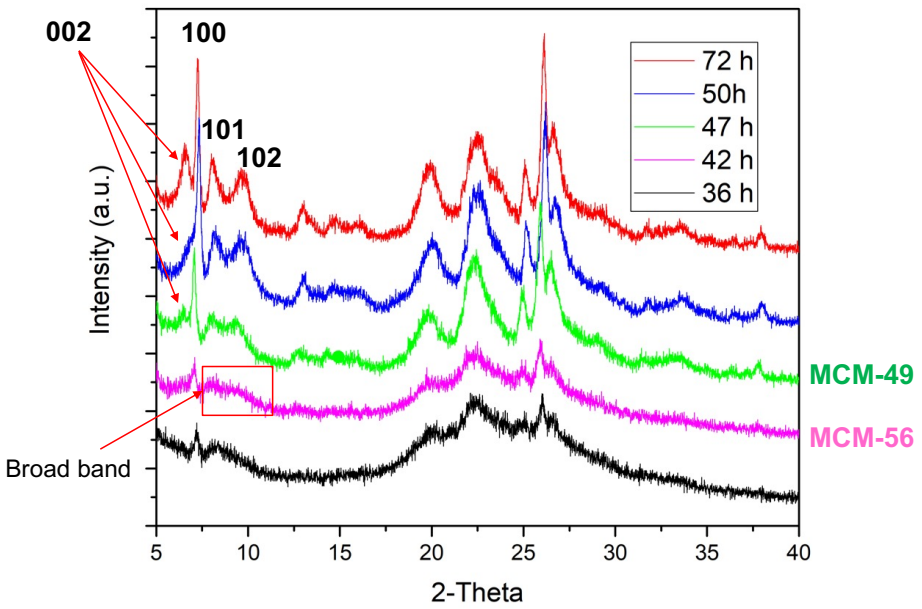

Figure 4.36 XRD patterns for MCM-56 synthesis at different time intervals

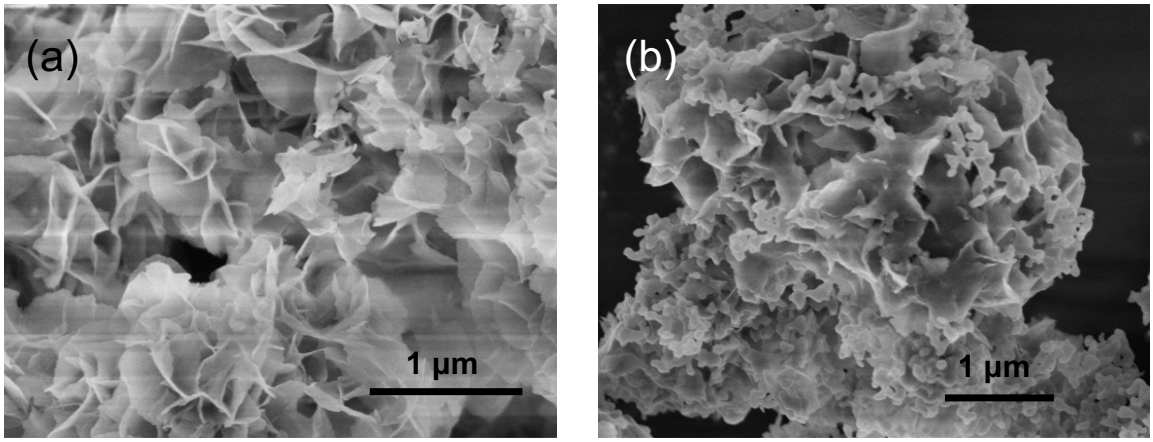

Figure 4.37 SEM images of (a) MCM-56(P) and (b) MCM-56(S)

The swollen sample was hand-mixed with HTPB for 1 min. The SAXS profile shows a weak (001) peak at ~1.3°. This indicates that HTPB intercalates the swollen zeolite, however, since the (001) peak has not fully disappeared, it indicates that only partial exfoliation occurred. The intensity of the (001) peak in this case is much lower than the case where MCM-22(S) is hand-mixed with HTPB for 1 min (Fig. 4.21b).

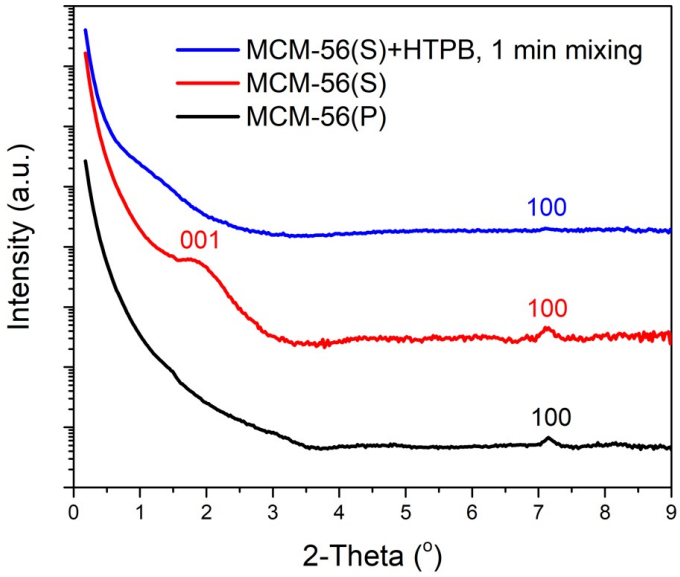

Figure 4.38 SAXS profiles of MCM-22(P), MCM-22(S) and MCM-22(S)/HTPB after 1 min of hand-mixing

The results indicate that MCM-56(S) gets more readily exfoliated than MCM-22(S). The reason probably lies in the fundamental difference in the nature of their layer surface and interlayer linking. The surface of MCM-56(P) has ≡Al—OH^-Na^+ moieties, producing weak connections, whereas the surface of MCM-22(P) is populated by pyramidal ≡Si—OH which form interlayer hydrogen bonding (Fig. 4.39b).[226] The formation of MCM-56 occurs as the effective content of Al increases above 5-6 and the extra Al atoms cannot be accommodated in the layer but must populate the surface. This has a chemical consequence, since replacement of ≡Si—OH on the surface with ≡Al—OH generates a negative charge (Al^{3+} replacing Si^{4+}) and requires presence of a cation for neutrality producing ≡Al—OH^-Na^+ moieties. The different surface populations of MCM-56(P) and MCM-22(P), ≡Al—OH^-Na^+ and ≡Si—OH respectively, suggests that the former moieties form a rather weak interlayer bond, during MCM-56 synthesis, thwart attachment of

additional layers causing disorder and monolayer structure. The weak connection between the MCM-56 layers could be the reason for its better exfoliation than MCM-22(P). However, both MCM-22(P) and MCM-56(P) do not self-exfoliate like ITQ-1(P) owing to the presence of framework Al in both.

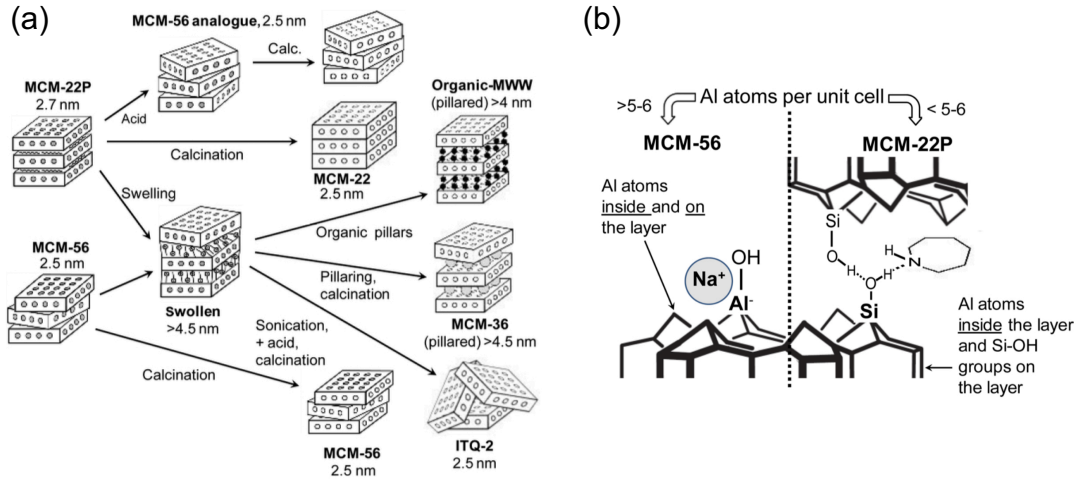

Figure 4.39 (a)Principal transformations reported for MCM-22(P) and MCM-56(P) with representative interlayer d_{001} spacing distances from XRD. Filled pores indicate presence of SDA molecules. (b) difference between the surface sites of MCM-56(P) and MCM-22(P)[226]

4.3.8. Synthesis of ITQ-1(P) in fluoride medium

Several studies have shown that synthesizing zeolites in fluoride medium instead of alkaline medium, leads to larger zeolite crystal size.[228–232] The synthesis of ITQ-1(P) in fluoride medium has not been reported in literature. We hypothesized that synthesizing ITQ-1(P) in fluoride medium could result in larger crystals, which on swelling and exfoliation could yield larger nanosheets.

ITQ-1(P) synthesized in fluoride medium with a gel composition of SiO_2: 0.5 HF: 0.25 TMAdaOH: 0.31 HMI: 3 H_2O yielded larger crystals than the one synthesized using alkaline medium (Fig. 4.40).

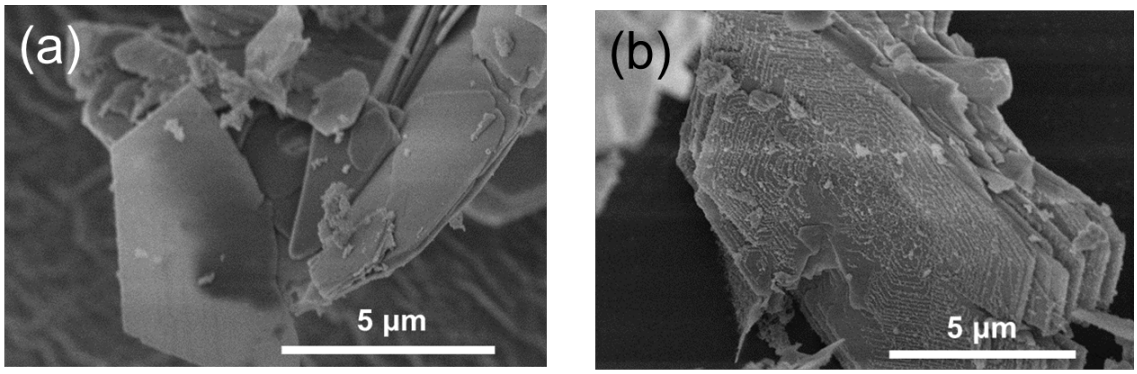

Figure 4.40 SEM images of ITQ-1(P) synthesized in fluoride medium

The first step towards exfoliating a layered precursor is to swell it. ITQ-1(P) synthesized in fluoride medium was subjected to swelling treatment using CTAB at room temperature. The SAXS pattern of the sample subjected to swelling is shown in Fig. 4.41a. A low intensity peak is observed at a lower 2θ angle (1.75°), corresponding to a d-spacing of 2.5 nm. However, a strong peak is observed at 2θ =3.22°, corresponding to a d-spacing of 1.3 nm (which is the original d-spacing of the ITQ-1(P) sample). This indicates that the swelling was not completely successful. On the other hand, the ITQ-1(P) sample synthesized in alkaline medium could be successfully swollen by subjecting it to the same swelling treatment (Fig. 4.23a).

Kim and coworkers studied the mechanism of room temperature swelling of MCM-22(P) and reported that Na^+ ions present in the layered precursor exchange for CTAB molecules, allowing the diffusion of CTAB molecules in the interlayer spacing and causing the subsequent swelling.[233] The synthesis of ITQ-1(P) in alkaline medium included the

addition of Na^+ ions to the synthesis gel, whereas in the fluoride medium synthesis, Na^+ ions are not added. We hypothesized that, since Na^+ ions are required for swelling, lack of Na^+ in ITQ-1(P)-fluoride sample could be the possible reason for unsuccessful exfoliation. Thus, we hypothesized that addition of Na^+ ions in the synthesis gel of ITQ-1(P)-fluoride could facilitate the subsequent swelling.

The synthesis recipe was modified, and varying amounts of sodium was added. The XRD patterns shown in Fig. 4.42 indicate that the crystallinity of the sample decreases with increase in the Na content. The samples with varying amounts of Na were subjected to room temperature swelling treatment with CTAB. The SAXS data is shown in Fig. 4.41. It was found that when the sodium content in the precursor sample was increased, the intensity of the peak at $2\theta = 1.75°$increased in the swollen sample, whereas the intensity of the peak at $2\theta = 3.22°$ decreased. This suggests that a larger fraction of the sample could be effectively swollen by increasing the sodium content of the precursor sample.

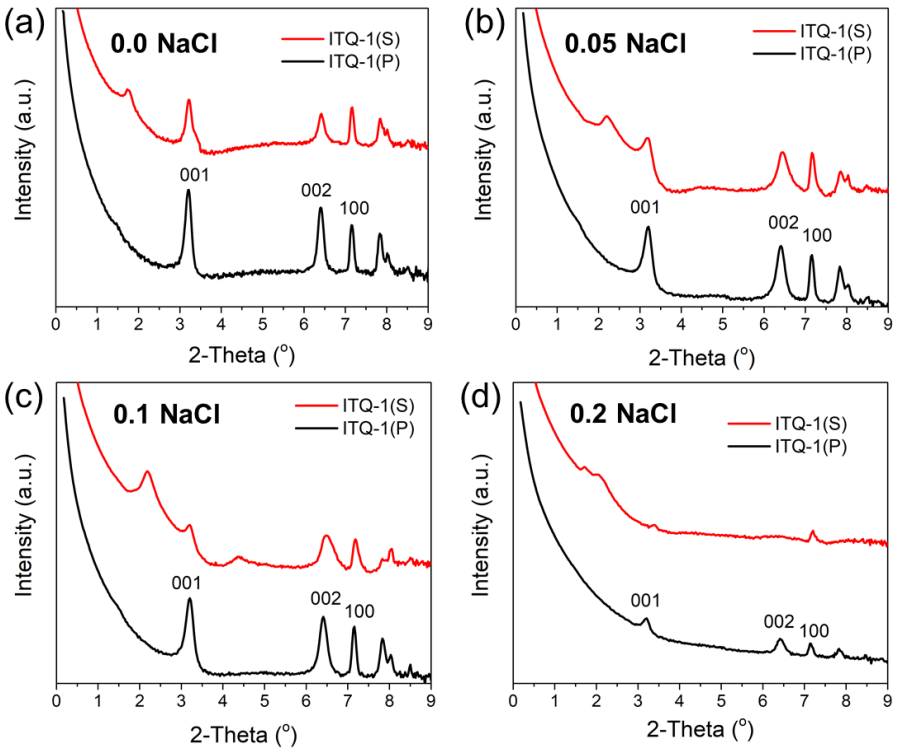

Figure 4.41 (a)-(d) SAXS profiles of the precursor (ITQ-1(P)) and swollen (ITQ-1(S)) samples for precursor samples with varying sodium contents

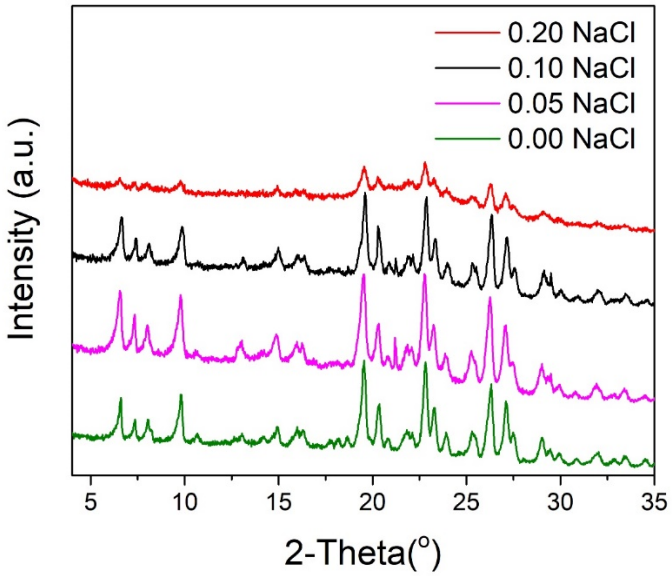

Figure 4.42 XRD patterns of ITQ-1(P) synthesized in fluoride medium with varying sodium contents

However, the swollen samples when hand-mixed with HTPB for 1 min could not be successfully exfoliated to large nanosheets. The reason could be attributed to the high hydrophobicity of the sample. Zeolites synthesized in fluoride medium have lesser defects and are more hydrophobic than their alkaline medium counterparts. Understanding the swelling and exfoliation mechanism of the samples synthesized in fluoride medium needs further work.

4.3.9. Fabrication of sintered silica fiber (SSF) supports

The first step towards preparing a MWW membrane is the uniform deposition of ITQ-1 nanosheets on a support. The polymer needs to be removed so that the nanosheets can be used for preparing coatings on porous supports. Removal of HTPB by heat treatment leads to curling and agglomeration of the nanosheets, deteriorating their ability to pack and

orient into a thin film. Thus, the liquid polymer is removed by dissolving it in toluene. A suspension of ITQ-1 nanosheets in toluene was prepared by washing the ITQ-1(S)/HTPB mixture with toluene. The solution was centrifuged and the supernatant containing majorly exfoliated ITQ-1 nanosheets was collected. This suspension was used as a coating-suspension. The suspension of nanosheets needs to be deposited on a porous support to make a uniform and oriented coating.

Porous alumina supports have been traditionally used for preparing molecular sieving zeolite membranes. Pham and coworkers reported that the fabrication of Stöber silica supports requires less energy and time, than that for porous alumina supports, because sintering of the amorphous silica beads into the disk-shaped supports requires a lower temperature (1020°C) and shorter period of time (2 h) than that for crystalline alumina powder (800°C, 24 h and 1240°C, 2 h).[146] Agrawal and coworkers reported that the Stöber silica supports do not exhibit high mechanical strength and often break during vacuum-assisted filter coating and assembly in a membrane module.[234] Moreover, both the Stöber silica and alumina supports exhibit permeances that become rate limiting for thin zeolite films. Therefore, high-aspect-ratio silica fibers, commonly known as quartz wool, were used to prepare relatively inexpensive sintered silica fiber (SSF) supports.[234] The SSF supports were prepared by sintering silica fibers followed by polishing. Sintering of large diameter silica fibers (1-10μm) led to large pores (~2 μm). As a result, the SSF supports exhibited more than an order of magnitude higher permeance than the Stöber silica supports. SSF-supported membranes were easy to handle and did not break during processing and module assembly.

Therefore, we fabricated and used SSF supports for our coatings. The bare SSF supports were coated with 500 nm Stöber silica particles to reduce their surface roughness. This was carried out by manually rubbing of 500 nm silica particles on the surface of the SSF supports. They were then coated with a thin layer of 50 nm silica particles by manual rubbing, which reduced the surface roughness further (Fig. 4.43). The support was subsequently used as a base for the nanosheet coating. The SEM images of the bare SSF support, support after coating with 500 nm particles and the one after coating with 50 nm particles is shown in Fig. 4.44. The suspension of ITQ-1 nanosheets in toluene was used to coat a film on the SSF support modified with 500 nm and 50 nm particles, using vacuum filtration. The amount of suspension used was tuned to ensure full, uniform coverage of the support. The SEM images of a coated SSF support are shown in Fig. 4.45.

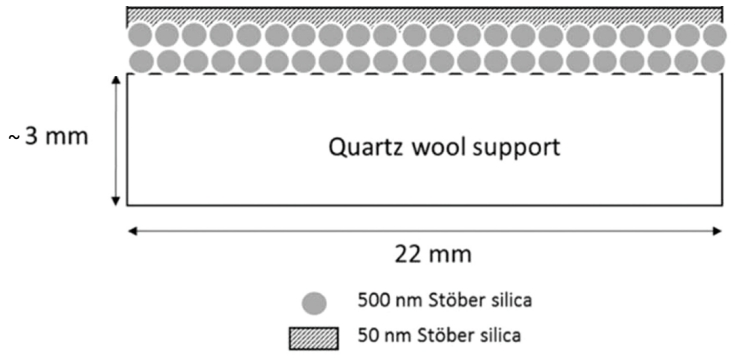

Figure 4.43 Schematic depiction of a SSF support coated with 500 nm and 50 nm Stöber silica particles

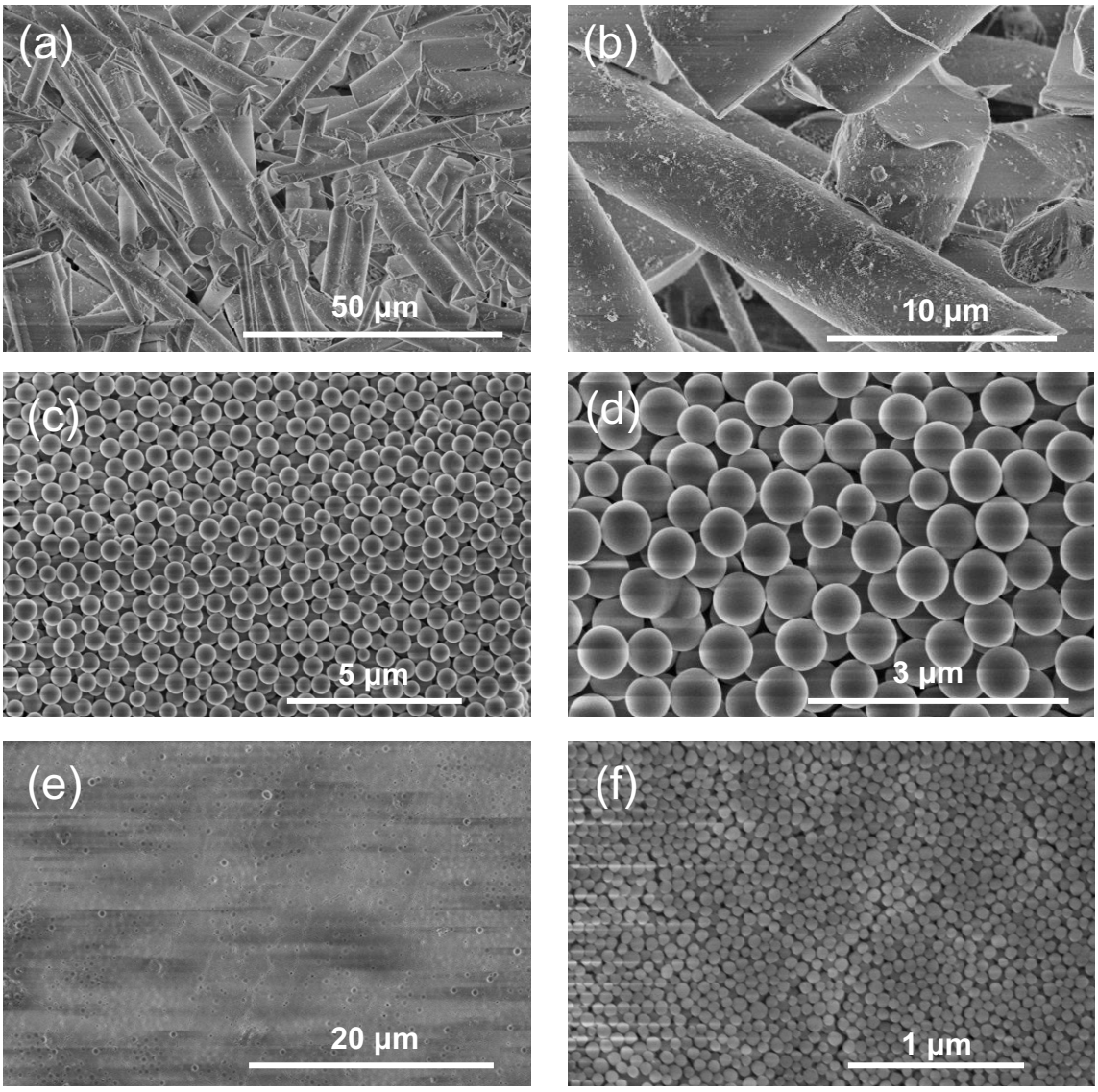

Figure 4.44 SEM images of (a), (b) bare SSF support, (c), (d) SSF support coated with 500 nm Stöber silica particles, (e), (f) SSF support coated with 50 nm Stöber silica particles

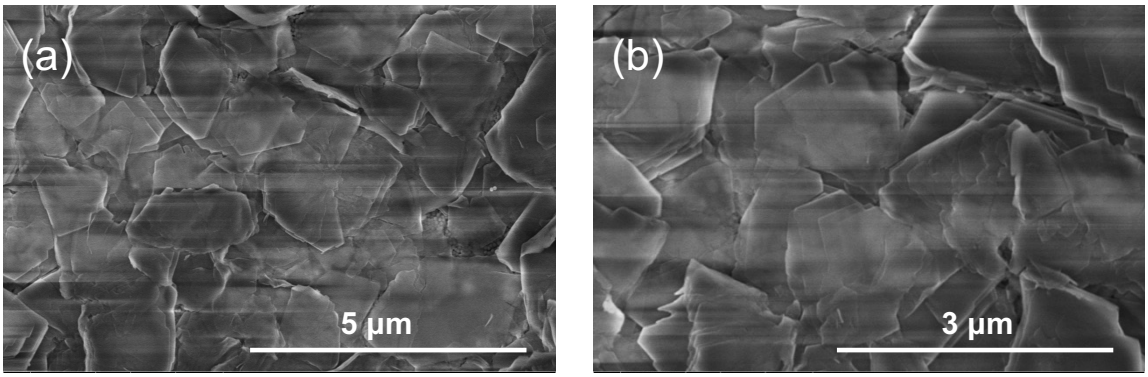

Figure 4.45 (a), (b) SEM images of ITQ-1 nanosheet coating over a SSF support modified with 500 nm and 50 nm Stöber silica particles

4.3.10. Gel-free secondary growth

After a uniform oriented layer of nanosheets is deposited on a porous support, a mild secondary growth is required to fill the pinhole defects that exist in the film. Preserving the preferred orientation of the film during secondary growth is the most important to maximize flux. Traditionally, a gel-based method has been used for the secondary growth of zeolite nanosheet seed layer. In a gel-based method, a support coated with a nanosheet seed layer is immersed in a silica gel containing the structure directing agent (SDA). It is then heated to a desired temperature in a sealed stainless-steel autoclave (Fig. 4.46a) The gel-based method is extremely sensitive to the concentration of the SDA in the silica gel. Misoriented crystal growth is highly likely, and thus it is difficult to preserve the preferred orientation of the film during secondary growth.[156] Varoon and coworkers performed a gel-based secondary growth on an ITQ-1 nanosheet seed layer deposited on α-alumina support.[168] The coated alumina support was immersed in an aged gel consisting of TMAdaOH and HMI (the organic structure directing agents required for the synthesis of ITQ-1(P)), and subjected to hydrothermal treatment. It was observed that

misoriented growth took place on the top of the seed layer (Fig. 4.16). A randomly oriented film is not desired because it reduces permeance and is also prone to crack formation during calcination, and also reduces the permeance through the membrane.

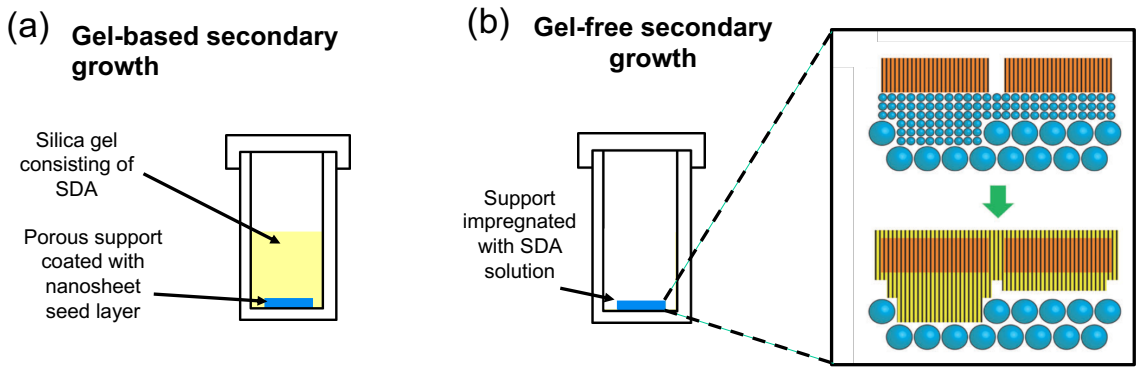

Figure 4.46 Schematic depiction of (a) gel-based secondary growth, (b) gel-free secondary growth

A gel-free growth method, on the other hand, offers fine control over the preferred orientation of the film during secondary growth. Agrawal and coworkers used the gel-free secondary growth method on a MFI seed layer deposited on SSF supports.[179] In a gel-free method, the nanosheet-coated SSF supports (modified with 500 nm and 50 nm Stöber silica particles) are impregnated with SDA solution. The support is then placed in sealed autoclave and heated to the desired temperature. During this process the 50 nm silica particles act as a sacrificial silica source for crystal growth. The SDA impregnated in the support moves upward by capillary force and aids in the crystal growth. A schematic of the secondary growth mechanism is shown in Fig. 4.46b.

A gel-free secondary growth on a seed layer of MWW nanosheets has not yet been reported. We performed a gel-free secondary growth on a seed layer of ITQ-1 nanosheets on a SSF support by impregnating the support with a SDA solution of TMAdaOH and

HMI. The SEM images of the fil after secondary growth are shown in Fig. 4.47. The results indicate that uniform growth occurred and misoriented crystals are not seen. This suggests that the preferred orientation of the film is preserved during secondary growth.

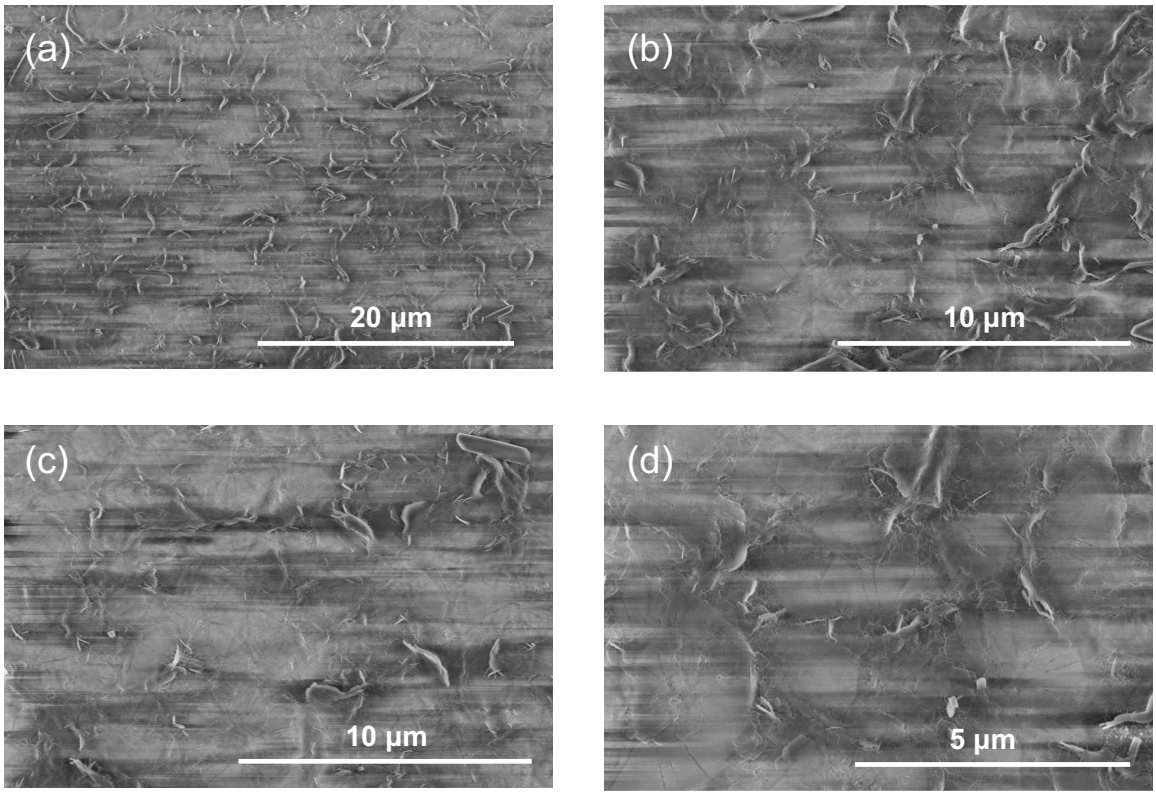

Figure 4.47 SEM images of ITQ-1 film after gel-free secondary growth of a seed layer on a SSF support modified with 500 nm and 50 nm Stöber silica particles

4.3.11. Synthesis and exfoliation of multilamellar MFI

The exfoliation method was also effective in exfoliating ml-MFI. ml-MFI was synthesized using $C_{22\text{-}6\text{-}6}(OH)_2$ as the organic structure directing agent. A 10 wt% mixture of ml-MFI with HTPB was subjected to 36 min of chaotic flow. The SAXS profile on the mixture does not show a complete disappearance of the (001) peak (Fig. 4.48). This suggests that a

certain amount of ml-MFI was not exfoliated. This is expected because of the highly intergrown nature of the ml-MFI material as reported in the previous studies[168,169].

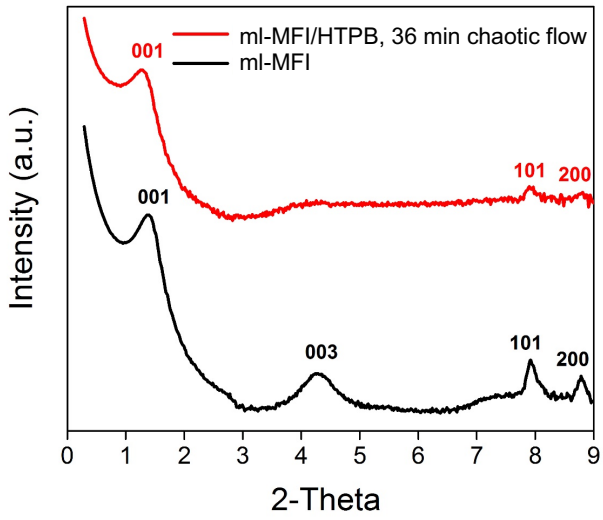

Figure 4.48 SAXS profiles of ml-MFI and ml-MFI/HTPB after 36 min of chaotic flow treatment

To separate the exfoliated 2D zeolite nanosheets, the ml-MFI/HTPB mixture was dispersed in toluene and centrifuged. The supernatant containing the exfoliated zeolite nanosheets was collected and used for TEM imaging. TEM characterization and the selected area electron diffraction pattern show the presence of MFI nanosheets with high crystallinity (Fig. 4.50). The thickness of the nanosheets was characterized using AFM, which showed a uniform nanosheet thickness of 3.4 ± 0.2 nm (Fig. 4.50), which is consistent with the previously reported thickness of a single-layer MFI nanosheet, which is 1.5 unit cells thick.[168]

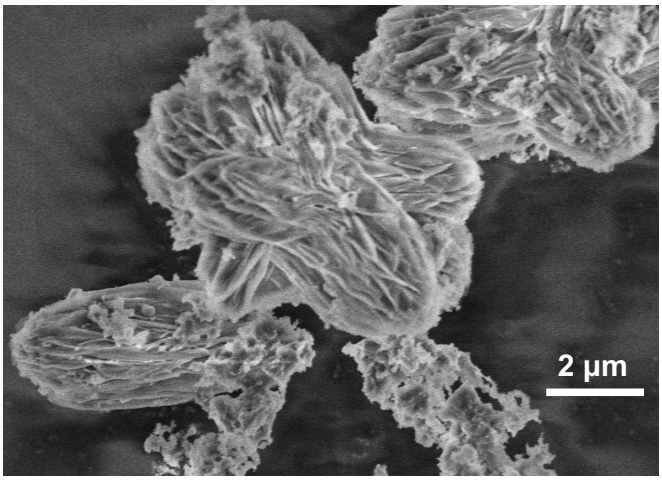

Figure 4.49 SEM image of ml-MFI

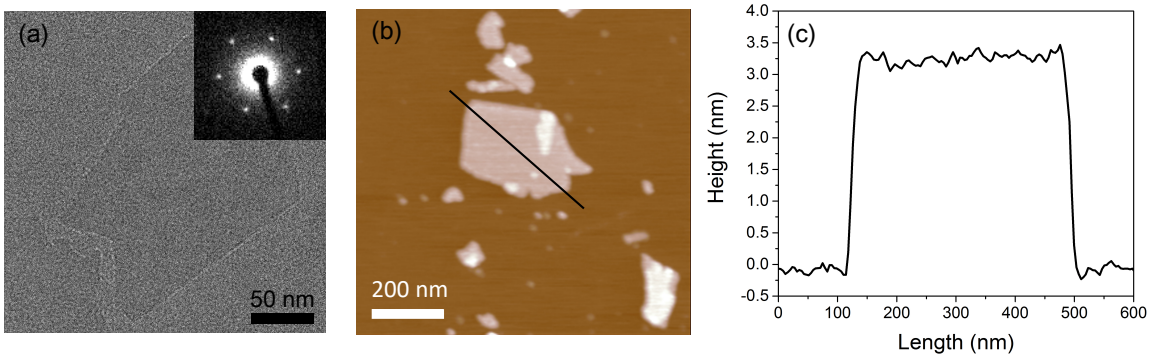

Figure 4.50 (a) TEM image of the MFI nanosheet and (inset) the electron diffraction pattern of the nanosheet, (b) AFM topographic image of the nanosheet on a mica disc, (c) line profile analysis of topographic height of the line scan of the MFI nanosheet shown in (b)

4.3.12. Conclusions

In conclusion, liquid exfoliation of layered MWW precursors with and without aluminum using commercially available liquid hydroxyl-terminated polybutadiene (HTPB) was studied. A successful self-disassembly of ITQ-1, a pure silica layered precursor with MWW framework, in a liquid phase was achieved. This exfoliation resulted in high aspect ratio ITQ-1 nanosheets since no shear force was applied during the process.

The exfoliation process for MCM-22, the aluminosilicate analog of ITQ-1, was also successful, but requires an additional shear force. It was found that the presence of aluminum in the framework is unfavorable for the exfoliation. Also, the nature of the organic structure directing agent (OSDA) in the interlayer spacing plays an important role in the exfoliation process possibly by affecting the interaction between the polybutadiene and zeolite precursors. An uniform coating of ITQ-1 nanosheets on a sintered silica fiber (SSF) support was achieved by vacuum filtration. A successful gel-free secondary growth was performed on this coating by preserving its preferred orientation.

CHAPTER 5

CONCLUSIONS AND FUTURE DIRECTIONS

5.1. Conclusions

Glucose can be obtained in high yield by the hydrolysis of cellulose in LiBr molten salt hydrate (MSH) with a small amount of inorganic acid. A biphasic reaction system is often used to convert glucose to 5-hydroxymethylfurfuryl (HMF) in MSH with parallel extraction of HMF to an organic phase However, direct separation of sugars from MSH without converting them into other chemicals is still highly desired because of their value and additional conversion pathways that sugars provide. In the first part of this thesis, adsorption of glucose on Norit SX Ultra activated carbon and ox-BP2000 carbon black in presence of LiBr molten salt hydrate was studied. The results indicated that the adsorption capacity was dependent on the surface area of the carbon material. Increase in LiBr MSH concentration has a negative effect on adsorption capacity. This might be due to adsorption of salt ions on the adsorption sites leading to reduction in the adsorption capacity. We hypothesized that a 3DOm carbon with graphitic pore walls (sp^2 carbon structure) can be synthesized by selectively controlling the deposition of carbon on a colloidal silica nanoparticle template. Such a graphitic 3DOm carbon can provide a large polycyclic aromatic domain size for increasing glucan adsorption from MSH. A three-dimensionally ordered mesoporous carbon (3DOm (*Eth*)) was synthesized using lanthanum-embedded silica nanoparticles as the template and ethylene as the carbon source. Its textural properties and carbon structure were compared with 3DOm (*Fur*) carbon synthesized conventionally

with furfuryl alcohol as the carbon source. The results indicated that 3DOm (*Eth*) is denser, more graphitic and has negligible micropores as compared to 3DOm (*Fur*).

Zeolites are normally synthesized under hydrothermal conditions in a sealed autoclave, which involves the use of a large amount of water as a solvent leading to high autogenous pressures, and safety and environmental issues due to the generation of large amounts of contaminated water. Recent research on solvent-free synthesis of zeolites, poses a question whether autogenous pressure is required for crystallization of zeolites or whether zeolites can be synthesized at atmospheric pressure. A solvent-free synthesis can lead to reduction in recycling/waste costs and that the separation of the solvent from the product is not required. In addition, an atmospheric pressure synthesis can lead to potential capital savings from a reduction in the need for pressure vessels. In the second part of this thesis, the crystallization kinetics of silicalite-1 was studied in a sealed autoclave system under autogenous pressure (hydrothermal synthesis and dry gel conversion) and an open fixed-bed reactor system at atmospheric pressure. The rate of crystallization is higher with higher H_2O/Si ratio in the initial synthesis gel. The rate of crystallization is higher with higher temperature. The results also indicated that at atmospheric pressure, the partial pressure of water in the vapor phase should be sufficient to cause capillary condensation of water in the micropores of the amorphous dry gel. The presence of a small quantity of liquid water inside the micropores of the dry gel is considered necessary for crystallization to occur.

Two-dimensional layered zeolite precursor with MWW framework is an excellent candidate for fabrication of hydrogen-selective membranes that can be used in an IGCC power plant for pre-combustion CO_2 capture. The MWW framework contains six-

membered ring apertures (~0.3 nm) that can allow the passage of H_2 but restrict the passage of CO_2. The current challenge is to develop a facile method for exfoliation of MCM-22(P), or its pure silica analog ITQ-1(P), which can yield high aspect-ratio MWW nanosheets. The other challenge is to form compact and uniform coatings of these nanosheets on a porous support and control the orientation of this film during secondary growth. In the third part of this thesis, liquid exfoliation of layered MWW precursors with and without aluminum using commercially available liquid hydroxyl-terminated polybutadiene (HTPB) was studied. A successful self-disassembly of ITQ-1, a pure silica layered precursor with MWW framework, in a liquid phase was achieved. This exfoliation resulted in high aspect ratio ITQ-1 nanosheets since no shear force was applied during the process. The exfoliation process for MCM-22, the aluminosilicate analog of ITQ-1, was also successful, but requires an additional shear force. It was found that the presence of aluminum in the framework is unfavorable for the exfoliation. Also, the nature of the organic structure directing agent (OSDA) in the interlayer spacing plays an important role in the exfoliation process possibly by affecting the interaction between the polybutadiene and zeolite precursors. An uniform coating of ITQ-1 nanosheets on a sintered silica fiber (SSF) support was achieved by vacuum filtration. A successful gel-free secondary growth was performed on this coating by preserving its preferred orientation.

5.2. Suggested future directions

Three-dimensional graphene architectures with periodic mesopores are of topical interest because of the possibility of combining the characteristics of graphene with a three-dimensional porous structure. In the first part of this thesis, the morphology of 3DOm

carbon from lanthanum-embedded silica nanoparticles and ethylene as the carbon source can be tuned by changing the concentration of lanthanum ions on the silica template, to achieve larger graphitic domains. The carbon can be synthesized in bulk quantities using a scaled-up fixed bed reactor and it can be used to measure glucose adsorption isotherms. 3DOm carbon with graphitic pore walls can also be used for other applications like electrodes in batteries, for hydrogen storage, catalysis, etc.

In the second part of this thesis, the experiments to synthesize silicalite-1 in a fixed-bed reactor operating at atmospheric pressure should be directed towards using a mixture of amine (like tert-butylamine (TBA), triethylamine (Et_3N) or ethylene diamine (EDA)) and steam, instead of using only steam. Kim and coworkers used a mixture of amine and water in vapor phase transport (VPT) synthesis of ZSM-5.[85] They demonstrated that some of the vapor phase water condenses into the micropores of the amorphous dry gel to form a restricted, liquid-water phase that then sets up a vapor-liquid equilibrium with the amine-water vapor phase to give an amine-water liquid phase in the micropores of the dry gel. When amines adsorb onto the restricted water phase, they protonate and produce OH^- by reaction with water. Thus, amines that are transported via the vapor phase as free amines can protonate in the restricted water environment to yield another source of cations and basicity. The pH of the liquid phase in the micropores of the dry gel somewhat mimics that of the liquid amine-water mixture. Thus, the presence of amine increases the basicity over that of pure water to expand the compositional region from which zeolites can be synthesized. A combination of the use of amine, high partial pressure of water in the vapor phase and a temperature suitable for capillary condensation of vapor to occur in the micropores of the dry gel can pave the way for a successful synthesis of silicalite-1 at

atmospheric pressure. This new method of synthesis can offer control over zeolite properties like hydrophobicity, defects and crystal size. The properties can be compared with the zeolites synthesized by conventional hydrothermal synthesis to gain insight into the synthesis mechanism. The effect of incorporation of heteroatoms on the synthesis can also be studied.

In the third part of this thesis, the high aspect ratio ITQ-1 nanosheets obtained by self-exfoliation in HTPB need to be purified to remove unexfoliated and partially exfoliated particles and the polymer (HTPB) itself. To achieve this, a more rigorous method than one used in our work will be required. The density-gradient centrifugation (DGC) method developed by Agrawal and coworkers can be used.[169] In DGC, particles are separated by exploiting the difference in their sedimentation velocity. This is attained by centrifugation of the particles in a fluid medium with density gradient along the depth of the fluid. The density gradient can be linear (linear increase in density along the depth of the fluid), or nonlinear (by stacking of fluids with dissimilar densities). If centrifugation is carried out for a long enough time to achieve equilibrium, particles with identical density accumulate in corresponding density zones along the depth of the fluid. DGC was first reported as a tool to calculate the molecular weight and partial specific volume of DNA and viruses by isopycnic sedimentation. DGC has been used to separate a variety of cells, cell fractionates, polymeric nanoparticles, carbon nanotubes, spherical core-shell nanoparticles, etc.

The procedure adopted by Agrawal and coworkers to purify MFI nanosheets from MFI/polystyrene composite is shown in Fig. 5.1. The first two steps were used to remove the polymer and the last step (non-linear density gradient) was used to removed partially

exfoliated and unexfoliated particles. A nonlinear density gradient created by simple stacking of fluids with varying density has been proved effective in separating particles based on their size and shape. This technique was used to separate exfoliated MFI nanosheets from unexfoliated particles. Purification was carried out by placing nanosheet suspension in n-octanol (ρ=0.82 g/cc) over density stacks created by chlorobenzene (ρ=1.10 g/cc), dichloromethane (ρ=1.33 g/cc), and chloroform (ρ=1.48 g/cc), followed by a mild-centrifugation at 12,000 g for 30 min. The top fraction in n-octanol contained most exfoliated nanosheets and was used for coatings.

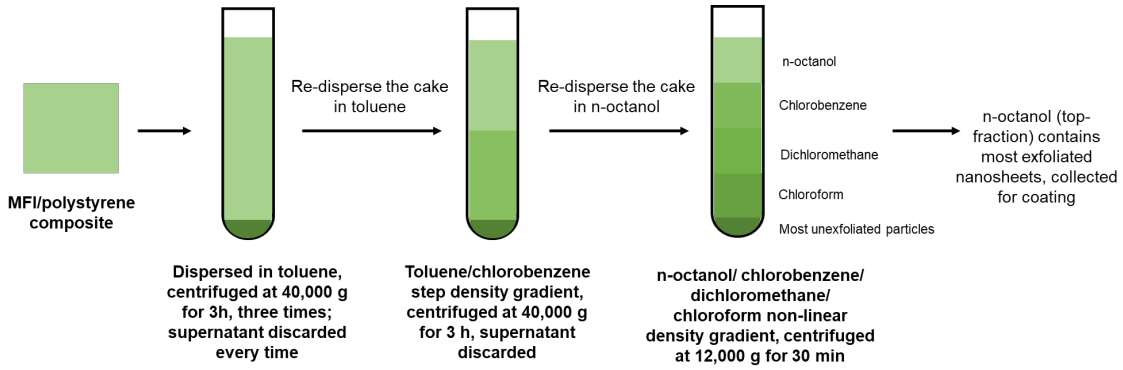

Figure 5.1 Density-gradient centrifugation (DGC) method developed by Agrawal and coworkers[169] to obtain a high-purity suspension of MFI nanosheets

In our case, ITQ-1 nanosheets are dispersed in HTPB (ρ=0.913 g/cc) matrix. The exact same procedure as described above can be applied to the ITQ-1/HTPB composite to obtain a dispersion of ITQ-1 nanosheets in n-octanol. Improvements to this method could be made by finding a better solvent to dissolve HTPB and for dispersing the nanosheets.

Pinhole defects in the coating after gel-free secondary growth can be reduced by tuning the concentration of TMAdaOH and HMI in the SDA solution used to impregnate the support and by tuning the temperature and time used for secondary growth.

A uniform defect-free coating on a SSF support (after calcination) can be loaded onto a membrane module and single-gas permeation measurements can be performed using a setup shown in Fig. 5.2. The permeances can be compared with the permeance of a SSF support without the coating as a control study. The single-gas permeances can also be used to determine the ideal gas selectivity.

$$P = \frac{J}{\Delta p} = \frac{pV}{RTA}\frac{1}{(p^F - p^P)}$$

$$P = permeance$$

$$J = permation\ flux$$

$$R = Universal\ gas\ consatnt$$

$$V = volume\ flowrate\ measured\ by\ bubble\ flow\ meter$$

$$T = permation\ temperature$$

$$A = permation\ area\ of\ the\ membrane$$

$$p = atmospheric\ pressure$$

$$(p^F - p^P) = transmembrane\ pressure\ drop$$

$$Ideal\ selectivity\ \alpha_{ij} = \frac{P_i}{P_j}$$

$$P_i\ and\ P_j\ are\ permeances\ of\ gases\ i\ and\ j\ respectively$$

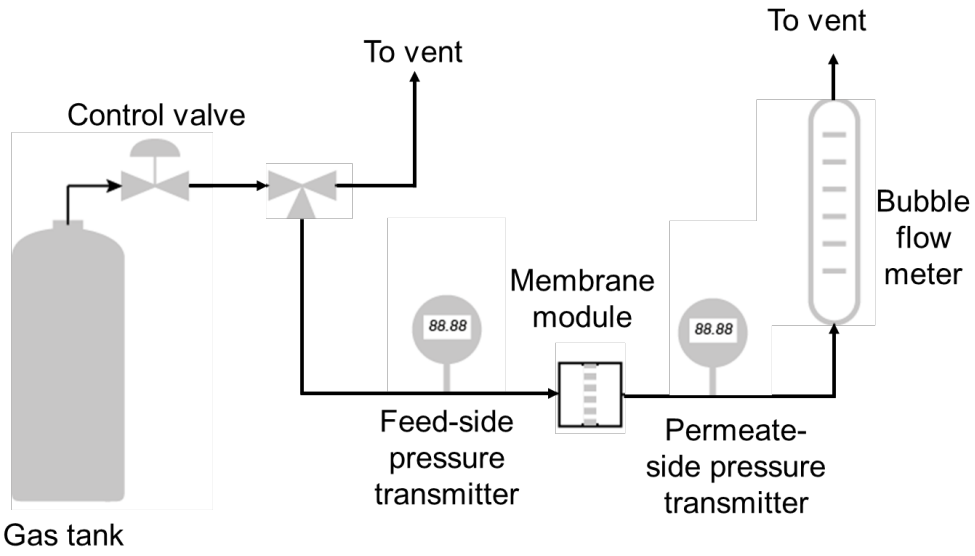

Figure 5.2 Proposed setup for single gas permeance measurements

The membranes can also be tested for binary (H_2/CO_2) separation to determine the flux and separation factor. It is also important to study if the membrane is stable at the operating conditions of a water-gas shift membrane reactor (WGSMR) in an IGCC power plant. Elyassi and coworkers[189] studied the long-term steam stability of ITQ-1 powder at 350 °C and 10 barg with a mixture of 95% H_2O and 5% N_2.

The polymer-zeolite interactions can further be studied using *in-situ* NMR and other techniques. Fundamental understanding of the mechanism can lead to application of this method to other layered materials like AlPOs (aluminum phosphates) and MOFs (metal organic frameworks). The properties of the liquid polymer (like molecular weight, building blocks, viscosity, functional end-groups, etc.) can be tuned to suit the d-spacing and surface morphology of various layered materials.

APPENDIX A

COMPARISON OF RADII OF GYRATION OF THE LIQUID POLYMERS

$$R_g \cong C_\infty N^{\frac{1}{2}} \quad (A.1)$$

Equation A.1 is used to understand the effect of polymer molecular weight on the size and conformation of the polymer, in which R_g is the radius of gyration of the polymer and N is the degree of polymerization.

$$N = \frac{M_n}{M_o} \quad (A.2)$$

Where M_n = Number average molecular weight

M_o = Molecular weight of the monomer unit

$$\frac{(R_g)_{CTPB}}{(R_g)_{HTPB}} = \frac{(C_\infty)_{CTPB}}{(C_\infty)_{HTPB}} \frac{(M_n)_{CTPB}{}^{1/2}}{(M_n)_{HTPB}{}^{1/2}}$$

Assuming the C_∞ for HTPB and CTPB are the same,

$$\frac{(R_g)_{CTPB}}{(R_g)_{HTPB}} = \frac{4200^{1/2}}{2800^{1/2}} = 1.22$$

Table A.1 d-spacing of MCM-22(S) after mixing with various liquid polymers

Polymer	**M_n (g/mol)**	**d-spacing after 1 min mixing without flow treatment (nm)**	**d-spacing after 36 min mixing with flow treatment (nm)**
HTPB	2800	9.4	Exfoliated
CTPB	4200	9.8	9.9
PB	5000	4.7	4.9

The interlayer d-spacing of MCM-22(S) powder is 4.6 nm. PB has no end-groups and does not intercalate the zeolite layer. Thus, PB doesn't change the d-spacing of MCM-22(S), highlighting its inability to intercalate the zeolite. HTPB and CTPB possess functional end-groups that can intercalate the zeolite only after mild mixing. The radius of gyration of CTPB is 1.22 times larger than that of HTPB. Hence, CTPB increases the d-spacing slightly more (9.8 nm) than HTPB (9.4 nm). However, after application of flow treatment, only HTPB is able to exfoliate the zeolite. On the other hand, CTPB increases the interlayer d-spacing only to 9.9 nm on application of flow treatment. This highlights the critical role of the polymer end-groups on exfoliation.

APPENDIX B

^{13}C MAS NMR CALCULATIONS

Calculations for MCM-22(P) and MCM-22(S)

From thermogravimetric analysis (TGA), MCM-22(P) contains 14.6 wt% organics, and MCM-22(S) contains 33.6 wt% organics. The 27 ppm and 48 ppm peaks in the ^{13}C MAS NMR of MCM-22(S) correspond to HMI. The peak areas of these peaks are 12.77% of the cumulative carbon peak areas.

Thus, the amount of HMI in MCM-22(S) = 4.3 wt %

Since two HMI molecules are occluded in a unit cell of MWW, MCM-22(P) contains ~4.4 wt% HMI. Since the HMI present in the 10 MR sinusoidal channels (intralayer) cannot leave the zeolite during swelling, we conclude that all the HMI from the interlayer spacing leaves the zeolite during the swelling treatment.

Calculations for ITQ-1(P) and ITQ-1(S)

In ^{13}C MAS NMR, 27.7 ppm peak corresponds to C_3 peak from HMI and the 35.5 ppm peak corresponds to C_3 and C_2 peak from $TMAda^+$.

$$\frac{\text{Amount of HMI}}{\text{Amount of TMAda}^+} = \frac{\text{Peak area (27.7 ppm peak)}}{\text{Peak area (35.5 ppm peak)}}$$

For ITQ-1(P):

$$\frac{\text{Amount of HMI}}{\text{Amount of TMAda}^+} = \frac{10.6}{36.8} = 0.288$$

For ITQ-1(S):

$$\frac{\text{Amount of HMI}}{\text{Amount of TMAda}^+} = \frac{4.1}{8.2} = 0.5$$

Since HMI is present only in the 10 MR sinusoidal channels of ITQ-1(P), we assume that it cannot leave the zeolite during the swelling treatment. Thus, the change in the ratio of amount of HMI to amount of $TMAda^+$ occurs solely due to the change in amount of $TMAda^+$ during the swelling treatment. Thus, the amount of $TMAda^+$ decreases by 42% post-swelling.

Calculations for ITQ-1-Al(P) and ITQ-1-Al(S)

In ^{13}C MAS NMR, 27.7 ppm peak corresponds to C_3 peak from HMI and the 35.5 ppm peak corresponds to C_3 and C_2 peak from $TMAda^+$.

For ITQ-1-Al(P):

$$\frac{\text{Amount of HMI}}{\text{Amount of TMAda}^+} = \frac{18.15}{36.2} = 0.5$$

For ITQ-1-Al(S):

$$\frac{\text{Amount of HMI}}{\text{Amount of TMAda}^+} = \frac{6.97}{14.75} = 0.46$$

Since HMI is present only in the 10 MR sinusoidal channels of ITQ-1-Al(P), we assume that it cannot leave the zeolite during the swelling treatment. The ratio of amount of HMI to amount of $TMAda^+$ is almost the same for ITQ-1-Al(P) and ITQ-1-Al(S). Thus, the amount of $TMAda^+$ stays the same after the swelling treatment.

BIBLIOGRAPHY

1 Y. Li, L. Li and J. Yu, *Chem*, 2017, **3**, 928–949.

2 H. Zheng, F. Gao and V. Valtchev, *Journal of Materials Chemistry A*, 2016, **4**, 16756–16770.

3 C. S. Cundy and P. A. Cox, *Chemical Reviews*, 2003, **103**, 663–701.

4 C. S. Cundy and P. A. Cox, *Microporous and Mesoporous Materials*, 2005, **82**, 1–78.

5 X. Meng and F. S. Xiao, *Chemical Reviews*, 2014, **114**, 1521–1543.

6 N. Kosinov, J. Gascon, F. Kapteijn and E. J. M. Hensen, *Journal of Membrane Science*, 2016, **499**, 65–79.

7 N. Rangnekar, N. Mittal, B. Elyassi, J. Caro and M. Tsapatsis, *Chemical Society Reviews*, 2015, **44**, 7128–7154.

8 C. Liang, Z. Li and S. Dai, *Angewandte Chemie - International Edition*, 2008, **47**, 3696–3717.

9 J. Wang, H. L. Xin and D. Wang, *Particle and Particle Systems Characterization*, 2014, **31**, 515–539.

10 M. Inagaki, M. Toyoda, Y. Soneda, S. Tsujimura and T. Morishita, *Carbon*, 2016, **107**, 448–473.

11 B. Sakintuna and Y. Yürüm, *Industrial and Engineering Chemistry Research*, 2005, **44**, 2893–2902.

12 H. Nishihara and T. Kyotani, *Advanced Materials*, 2012, **24**, 4473–4498.

13 W. Libbrecht, A. Verberckmoes, J. W. Thybaut, P. van der Voort and J. de Clercq, *Carbon*, 2017, **116**, 528–546.

14 T. Y. Ma, L. Liu and Z. Y. Yuan, *Chemical Society Reviews*, 2013, **42**, 3977–4003.

15 J. Lee, J. Kim and T. Hyeon, *Advanced Materials*, 2006, **18**, 2073–2094.

16 P. W. Chung, M. Yabushita, A. T. To, Y. Bae, J. Jankolovits, H. Kobayashi, A. Fukuoka and A. Katz, *ACS Catalysis*, 2015, **5**, 6422–6425.

17 P. W. Chung, A. Charmot, O. M. Gazit and A. Katz, *Langmuir*, 2012, **28**, 15222–15232.

18 J. N. Chheda, G. W. Huber and J. A. Dumesic, *Angewandte Chemie - International Edition*, 2007, **46**, 7164–7183.

19 G. W. Huber, S. Iborra and A. Corma, *Chemical Reviews*, 2006, **106**, 4044–4098.

20 R. Rinaldi and F. Schüth, *ChemSusChem*, 2009, **2**, 1096–1107.

21 M. Mascal and E. B. Nikitin, *Angewandte Chemie*, 2008, **120**, 8042–8044.

22 R. Rinaldi, R. Palkovits and F. Schüth, *Angewandte Chemie - International Edition*, 2008, **47**, 8047–8050.

23 K. Rajendran, E. Drielak, V. Sudarshan Varma, S. Muthusamy and G. Kumar, *Biomass Conversion and Biorefinery*, 2018, **8**, 471–483.

24 I. P. Samayam, B. L. Hanson, P. Langan and C. A. Schall, *Biomacromolecules*, 2011, **12**, 3091–3098.

25 S. H. Lee, T. v. Doherty, R. J. Linhardt and J. S. Dordick, *Biotechnology and Bioengineering*, 2009, **102**, 1368–1376.
26 X. Liu, Q. Xu, J. Liu, D. Yin, S. Su and H. Ding, *Fuel*, 2016, **164**, 46–50.
27 R. Rinaldi and F. Schüth, *Energy and Environmental Science*, 2009, **2**, 610–626.
28 W. Deng, J. R. Kennedy, G. Tsilomelekis, W. Zheng and V. Nikolakis, *Industrial and Engineering Chemistry Research*, 2015, **54**, 5226–5236.
29 S. Sen, J. D. Martin and D. S. Argyropoulos, *ACS Sustainable Chemistry and Engineering*, 2013, **1**, 858–870.
30 A. Schenzel, A. Hufendiek, C. Barner-Kowollik and M. A. R. Meier, *Green Chemistry*, 2014, **16**, 3266–3271.
31 H. Wang, G. Gurau and R. D. Rogers, *Chemical Society Reviews*, 2012, **41**, 1519–1537.
32 S. Fischer, H. Leipner, K. Thümmler, E. Brendler and J. Peters, *Cellulose*, 2003, **10**, 227–236.
33 B. Medronho and B. Lindman, *Current Opinion in Colloid and Interface Science*, 2014, **19**, 32–40.
34 Z. Jiang, J. Fan, V. L. Budarin, D. J. Macquarrie, Y. Gao, T. Li, C. Hu and J. H. Clark, *Sustainable Energy and Fuels*, 2018, **2**, 936–940.
35 T. P. Thuy Pham, C. W. Cho and Y. S. Yun, *Water Research*, 2010, **44**, 352–372.
36 T. C. R. Brennan, S. Datta, H. W. Blanch, B. A. Simmons and B. M. Holmes, *Bioenergy Research*, 2010, **3**, 123–133.
37 T. vander Hoogerstraete, S. Wellens, K. Verachtert and K. Binnemans, *Green Chemistry*, 2013, **15**, 919–927.
38 C. Garkoti, J. Shabir and S. Mozumdar, *New Journal of Chemistry*, 2017, **41**, 9291–9298.
39 S. Sadula, O. Oesterling, A. Nardone, B. Dinkelacker and B. Saha, *Green Chemistry*, 2017, **19**, 3888–3898.
40 N. Rodriguez Quiroz, A. M. D. Padmanathan, S. H. Mushrif and D. G. Vlachos, *ACS Catalysis*, 2019, **9**, 10551–10561.
41 J. van den Bergh, W. Wiedenhof, D. Siwy and H. Heinerman, *Adsorption*, 2017, **23**, 563–568.
42 T. G. A. Youngs, C. Hardacre and J. D. Holbrey, *The Journal of Physical Chemistry B*, 2007, **111**, 13765–13774.
43 B. Saha and M. M. Abu-Omar, *Green Chemistry*, 2014, **16**, 24–38.
44 J. N. Chheda and J. a Dumesic, *Science*, 2006, **312**, 1933.
45 H. Kobayashi, M. Yabushita, T. Komanoya, K. Hara, I. Fujita and A. Fukuoka, *ACS Catalysis*, 2013, **3**, 581–587.
46 M. Kitano, D. Yamaguchi, S. Suganuma, K. Nakajima, H. Kato, S. Hayashi and M. Hara, *Langmuir*, 2009, **25**, 5068–5075.
47 S. Suganuma, K. Nakajima, M. Kitano, D. Yamaguchi, H. Kato, S. Hayashi and M. Hara, *Journal of the American Chemical Society*, 2008, **130**, 12787–12793.
48 H. P. Boehm, eds. D. D. Eley, H. Pines and P. B. B. T.-A. in C. Weisz, Academic Press, 1966, vol. 16, pp. 179–274.
49 H. P. Boehm, *Carbon*, 1994, **32**, 759–769.

50 A. Charmot, P. W. Chung and A. Katz, *ACS Sustainable Chemistry and Engineering*, 2014, **2**, 2866–2872.
51 M. Yabushita, K. Techikawara, H. Kobayashi, A. Fukuoka and A. Katz, *ACS Sustainable Chemistry and Engineering*, 2016, **4**, 6844–6851.
52 H. Kobayashi, M. Yabushita, J. Y. Hasegawa and A. Fukuoka, *Journal of Physical Chemistry C*, 2015, **119**, 20993–20999.
53 M. Yabushita, H. Kobayashi, J. Y. Hasegawa, K. Hara and A. Fukuoka, *ChemSusChem*, 2014, **7**, 1443–1450.
54 W. Fan, M. A. Snyder, S. Kumar, P. S. Lee, W. C. Yoo, A. v. McCormick, R. Lee Penn, A. Stein and M. Tsapatsis, *Nature Materials*, 2008, **7**, 984–991.
55 P. Dornath, H. J. Cho, A. Paulsen, P. Dauenhauer and W. Fan, *Green Chemistry*, 2015, **17**, 769–775.
56 P. Dornath, S. Ruzycky, S. Pang, L. He, P. Dauenhauer and W. Fan, *Green Chemistry*, 2016, **18**, 6637–6647.
57 H. Lee, K. Kim, S. H. Kang, Y. Kwon, J. H. Kim, Y. K. Kwon, R. Ryoo and J. Y. Park, *Scientific Reports*, 2017, **7**, 1–9.
58 S. K. Lee, H. Park, J. W. Yoon, K. Kim, S. J. Cho, G. Maurin, R. Ryoo and J. S. Chang, *ACS Applied Materials and Interfaces*, 2020, **12**, 28484–28495.
59 K. Kim, T. Lee, Y. Kwon, Y. Seo, J. Song, J. K. Park, H. Lee, J. Y. Park, H. Ihee, S. J. Cho and R. Ryoo, *Nature*, 2016, **535**, 131–135.
60 K. Kim, Y. Kwon, T. Lee, S. J. Cho and R. Ryoo, *Carbon*, 2017, **118**, 517–523.
61 J. S. Lee, S. H. Joo and R. Ryoo, *Journal of the American Chemical Society*, 2002, **124**, 1156–1157.
62 T. W. Kim, I. S. Park and R. Ryoo, *Angewandte Chemie - International Edition*, 2003, **42**, 4375–4379.
63 P. Dornath and W. Fan, *Microporous and Mesoporous Materials*, 2014, **191**, 10–17.
64 M. Kruk, M. Jaroniec and Y. Bereznitski, *Journal of Colloid and Interface Science*, 1996, **182**, 282–288.
65 N. Rajabbeigi, R. Ranjan and M. Tsapatsis, *Microporous and Mesoporous Materials*, 2012, **158**, 253–256.
66 M. Yabushita, K. Techikawara, H. Kobayashi, A. Fukuoka and A. Katz, *ACS Sustainable Chemistry and Engineering*, 2016, **4**, 6844–6851.
67 C. Moreno-Castilla, M. A. Ferro-García, J. P. Joly, I. Bautista-Toledo, F. Carrasco-Marín and J. Rivera-Utrilla, *Langmuir*, 1995, **11**, 4386–4392.
68 Q. Liu, Q. Ma, S. Sabnis, W. Zheng, D. G. Vlachos, W. Fan, W. Li and L. Ma, *Green Chemistry*, 2019, 5030–5038.
69 M. Chevalier, F. Robert, N. Amusant, M. Traisnel, C. Roos and M. Lebrini, *Electrochimica Acta*, 2014, **131**, 96–105.
70 C. Hontoria-Lucas, A. J. López-Peinado, J. de D. López-González, M. L. Rojas-Cervantes and R. M. Martín-Aranda, *Carbon*, 1995, **33**, 1585–1592.
71 G. Y. Gor, M. Thommes, K. A. Cychosz and A. v. Neimark, *Carbon*, 2012, **50**, 1583–1590.
72 K. A. Cychosz, X. Guo, W. Fan, R. Cimino, G. Y. Gor, M. Tsapatsis, A. v. Neimark and M. Thommes, *Langmuir*, 2012, **28**, 12647–12654.

73 W. C. Yoo, N. Rajabbeigi, E. E. Mallon, M. Tsapatsis and M. A. Snyder, *Microporous and Mesoporous Materials*, 2014, **184**, 72–82.
74 S. K. Sze, N. Siddique, J. J. Sloan and R. Escribano, *Atmospheric Environment*, 2001, **35**, 561–568.
75 A. Sadezky, H. Muckenhuber, H. Grothe, R. Niessner and U. Pöschl, *Carbon*, 2005, **43**, 1731–1742.
76 G. A. Zickler, B. Smarsly, N. Gierlinger, H. Peterlik and O. Paris, *Carbon*, 2006, **44**, 3239–3246.
77 M. E. Davis, *Nature*, 2002, **417**, 813–821.
78 A. Corma, *Chemical Reviews*, 1995, **95**, 559–614.
79 Y. Li, L. Li and J. Yu, *Chem*, 2017, **3**, 928–949.
80 X. Meng and F. S. Xiao, *Chemical Reviews*, 2014, **114**, 1521–1543.
81 Q. Wu, X. Meng, X. Gao and F. S. Xiao, *Accounts of Chemical Research*, 2018, **51**, 1396–1403.
82 R. E. Morris and S. L. James, *Angewandte Chemie - International Edition*, 2013, **52**, 2163–2165.
83 M. Matsukata, N. Nishiyama and K. Ueyama, *Microporous Materials*, 1993, **1**, 219–222.
84 D. E. Demong, I. Ng, M. W. Miller and A. W. Stamford, *Organic Letters*, 2013, **15**, 2830–2833.
85 M.-H. Kim, H.-X. Li and M. E. Davis, *Microporous Materials*, 1993, **1**, 191–200.
86 S. G. Thoma and T. M. Nenoff, *Microporous and Mesoporous Materials*, 2000, **41**, 295–305.
87 M. Matsukata, M. Ogura, T. Osaki, P. R. Hari Prasad Rao, M. Nomura and E. Kikuchi, *Topics in Catalysis*, 1999, **9**, 77–92.
88 M. Matsukata, N. Nishiyama and K. Ueyama, *Microporous Materials*, 1996, **7**, 109–117.
89 V. Vattipalli, A. M. Paracha, W. Hu, H. Chen and W. Fan, *Angewandte Chemie - International Edition*, 2018, **57**, 3607–3611.
90 D. M. Bibby and M. P. Dale, *Nature*, 1985, **317**, 157–158.
91 E. R. Parnham and R. E. Morris, *Accounts of Chemical Research*, 2007, **40**, 1005–1013.
92 H. Ma, Z. Tian, R. Xu, B. Wang, Y. Wei, L. Wang, Y. Xu, W. Zhang and L. Lin, *Journal of the American Chemical Society*, 2008, **130**, 8120–8121.
93 E. R. Cooper, C. D. Andrews, P. S. Wheatley, P. B. Webb, P. Wormald and R. E. Morris, *Nature*, 2004, **430**, 1012–1016.
94 L. Ren, Q. Wu, C. Yang, L. Zhu, C. Li, P. Zhang, H. Zhang, X. Meng and F. S. Xiao, *Journal of the American Chemical Society*, 2012, **134**, 15173–15176.
95 Q. Wu, X. Wang, G. Qi, Q. Guo, S. Pan, X. Meng, J. Xu, F. Deng, F. Fan, Z. Feng, C. Li, S. Maurer, U. Müller and F. S. Xiao, *Journal of the American Chemical Society*, 2014, **136**, 4019–4025.
96 Q. Wu, X. Liu, L. Zhu, L. Ding, P. Gao, X. Wang, S. Pan, C. Bian, X. Meng, J. Xu, F. Deng, S. Maurer, U. Müller and F. S. Xiao, *Journal of the American Chemical Society*, 2015, **137**, 1052–1055.

97 D. Wu, X. Yu, X. Chen, G. Yu, K. Zhang, M. Qiu, W. Xue, C. Yang, Z. Liu and Y. Sun, *ChemSusChem*, 2019, **12**, 3871–3877.
98 B. Zhang, M. Douthwaite, Q. Liu, C. Zhang, Q. Wu, R. Shi, P. Wu, K. Liu, Z. Wang, W. Lin, H. Cheng, D. Ma, F. Zhao and G. J. Hutchings, *Green Chemistry*, 2020, **22**, 1630–1638.
99 G. T. Kokotailo, S. L. Lawton, D. H. Olson and W. M. Meier, *Nature*, 1978, **272**, 437–438.
100 M. B. J. Roeffaers, R. Ameloot, A. J. Bons, W. Mortier, G. de Cremer, R. de Kloe, J. Hofkens, D. E. de Vos and B. F. Sels, *Journal of the American Chemical Society*, 2008, **130**, 13516–13517.
101 A. Corma, *Chemical Reviews*, 1997, **97**, 2373–2419.
102 C. H. Christensen, K. Johannsen, I. Schmidt and C. H. Christensen, *Journal of the American Chemical Society*, 2003, **125**, 13370–13371.
103 D. H. Olson, G. T. Kokotailo, S. L. Lawton and W. M. Meier, *Journal of Physical Chemistry*, 1981, **85**, 2238–2243.
104 E. M. Flanigen, J. M. Bennett, R. W. Grose, J. P. Cohen, R. L. Patton, R. M. Kirchner and J. v Smith, *Nature*, 1978, **271**, 512–516.
105 W. Xu, J. Dong, J. Li, J. Li and F. Wu, *Journal of the Chemical Society, Chemical Communications*, 1990, 755–756.
106 S. Alfaro, M. A. Valenzuela and P. Bosch, *Journal of Porous Materials*, 2009, **16**, 337–342.
107 L. Zhang, X. Wang and Y. Chen, *Chemical Engineering Journal*, 2020, **382**, 122913.
108 Y. Yan, R. Cai, Y. Liu and S. Gu, *Journal of the American Chemical Society*, 2010, **132**, 12776–12777.
109 A. Y. Ku, P. Kulkarni, R. Shisler and W. Wei, *Journal of Membrane Science*, 2011, **367**, 233–239.
110 D. Georgis, F. v. Lima, A. Almansoori and P. Daoutidis, *Industrial and Engineering Chemistry Research*, 2014, **53**, 7461–7469.
111 F. v. Lima, P. Daoutidis, M. Tsapatsis and J. J. Marano, *Industrial and Engineering Chemistry Research*, 2012, **51**, 5480–5489.
112 M. Bracht, P. T. Alderliesten, R. Kloster, R. Pruschek, G. Haupt, E. Xue, J. R. H. Ross, M. K. Koukou and N. Papayannakos, *Energy Conversion and Management*, , DOI:10.1016/s0196-8904(96)00263-4.
113 S. Rezvani, Y. Huang, D. McIlveen-Wright, N. Hewitt and J. D. Mondol, *Fuel*, 2009, **88**, 2463–2472.
114 N. A. Al-Mufachi, N. v. Rees and R. Steinberger-Wilkens, *Renewable and Sustainable Energy Reviews*, 2015, **47**, 540–551.
115 S. J. Kim, S. Yang, G. K. Reddy, P. Smirniotis and J. Dong, *Energy and Fuels*, 2013, **27**, 4471–4480.
116 A. Lotrič, M. Sekavčnik, C. Kunze and H. Spliethoff, *Strojniski Vestnik/Journal of Mechanical Engineering*, 2011, **57**, 911–926.
117 S. J. Kim, Z. Xu, G. K. Reddy, P. Smirniotis and J. Dong, *Industrial and Engineering Chemistry Research*, 2012, **51**, 1364–1375.

118 S. Battersby, S. Smart, B. Ladewig, S. Liu, M. C. Duke, V. Rudolph and J. C. D. da Costa, *Separation and Purification Technology*, 2009, **66**, 299–305.
119 D. Ma and C. R. F. Lund, *Industrial and Engineering Chemistry Research*, 2003, **42**, 711–717.
120 A. Criscuoli, A. Basile, E. Drioli and O. Loiacono, *Journal of Membrane Science*, 2001, **181**, 21–27.
121 H. Li, J. W. Dijkstra, J. A. Z. Pieterse, J. Boon, R. W. van den Brink and D. Jansen, *Journal of Membrane Science*, 2010, **363**, 204–211.
122 S. Zhou, X. Zou, F. Sun, H. Ren, J. Liu, F. Zhang, N. Zhao and G. Zhu, *International Journal of Hydrogen Energy*, 2013, **38**, 5338–5347.
123 Y. Li, F. Liang, H. Bux, W. Yang and J. Caro, *Journal of Membrane Science*, 2010, **354**, 48–54.
124 M. Rezakazemi, K. Shahidi and T. Mohammadi, *International Journal of Hydrogen Energy*, 2012, **37**, 17275–17284.
125 F. Zhang, X. Zou, X. Gao, S. Fan, F. Sun, H. Ren and G. Zhu, *Advanced Functional Materials*, 2012, **22**, 3583–3590.
126 Y. Zhang, Z. Wu, Z. Hong, X. Gu and N. Xu, *Chemical Engineering Journal*, 2012, **197**, 314–321.
127 M. D. Dolan, N. C. Dave, A. Y. Ilyushechkin, L. D. Morpeth and K. G. McLennan, *Journal of Membrane Science*, 2006, **285**, 30–55.
128 D. Lee and S. T. Oyama, *Journal of Membrane Science*, 2002, **210**, 291–306.
129 S. Adhikari and S. Fernando, *Industrial and Engineering Chemistry Research*, 2006, **45**, 875–881.
130 H. Li, Z. Song, X. Zhang, Y. Huang, S. Li, Y. Mao, H. J. Ploehn, Y. Bao and M. Yu, *Science*, 2013, **342**, 95–98.
131 J. Franz and V. Scherer, *Journal of Membrane Science*, 2010, **359**, 173–183.
132 M. Gazzani, D. M. Turi and G. Manzolini, *International Journal of Greenhouse Gas Control*, 2014, **20**, 293–309.
133 K. A. Atsonios, K. D. Panopoulos, A. F. Doukelis, A. K. Koumanakos, J. Morud and E. Kakaras, *Energy Procedia*, 2013, **37**, 914–923.
134 A. K. Prabhu and S. T. Oyama, *Journal of Membrane Science*, 2000, **176**, 233–248.
135 S. Giessler, L. Jordan, J. Diniz da Costa and G. Q. M. Lu, *Separation and Purification Technology*, 2003, **32**, 255–264.
136 A. Basile, E. Drioli, F. Santella, V. Violante, G. Capannelli and G. Vitulli, *Gas Separation and Purification*, 1996, **10**, 53–61.
137 D. Mendes, V. Chibante, J. M. Zheng, S. Tosti, F. Borgognoni, A. Mendes and L. M. Madeira, *International Journal of Hydrogen Energy*, 2010, **35**, 12596–12608.
138 W. J. Roth, P. Nachtigall, R. E. Morris and J. Čejka, *Chemical Reviews*, 2014, **114**, 4807–4837.
139 W. J. Roth and J. Ejka, *Catalysis Science and Technology*, 2011, **1**, 43–53.
140 F. S. O. Ramos, M. K. de Pietre and H. O. Pastore, *RSC Advances*, 2013, **3**, 2084–2111.

141 M. Witman, S. Ling, P. Boyd, S. Barthel, M. Haranczyk, B. Slater and B. Smit, *ACS Central Science*, 2018, **4**, 235–245.
142 O. Knio, A. J. Medford, S. Nair and D. S. Sholl, *Chemistry of Materials*, 2019, **31**, 353–364.
143 M. E. Leonowicz, J. A. Lawton, S. L. Lawton and M. K. Rubin, *Science*, 1994, **264**, 1910–1913.
144 J. Caro, M. Noack and P. Kölsch, *Adsorption*, 2005, **11**, 215–227.
145 W. J. Koros, *AIChE Journal*, 2004, **50**, 2326–2334.
146 T. C. T. Pham, T. H. Nguyen and K. B. Yoon, *Angewandte Chemie - International Edition*, 2013, **52**, 8693–8698.
147 W. J. Koros and R. Mahajan, *Journal of Membrane Science*, 2001, **181**, 141.
148 W. gwi Kim and S. Nair, *Chemical Engineering Science*, 2013, **104**, 908–924.
149 T. C. T. Pham, H. S. Kim and K. B. Yoon, *Science*, 2011, **334**, 1533–1539.
150 Y. Yan, M. Tsapatsis, G. R. Gavalas and M. E. Davis, *Journal of the Chemical Society, Chemical Communications*, 1995, 227–228.
151 G. Bonilla, M. Tsapatsis, D. G. Vlachos and G. Xomeritakis, *Journal of Membrane Science*, 2001, **182**, 103–109.
152 A. Tuel and Y. ben Taarit, *Microporous Materials*, 1993, **1**, 179–189.
153 G. Xomeritakis, S. Nair and M. Tsapatsis, *Microporous and mesoporous materials*, 2000, **38**, 61–73.
154 T. O. Drews and M. Tsapatsis, *Microporous and Mesoporous Materials*, 2007, **101**, 97–107.
155 J. S. Lee, H. K. Jae, J. L. Young, C. J. Nak and B. Y. Kyung, *Angewandte Chemie - International Edition*, 2007, **46**, 3087–3090.
156 X. Li, Y. Peng, Z. Wang and Y. Yan, *CrystEngComm*, 2011, **13**, 3657–3660.
157 V. Nikolakis, E. Kokkoli, M. Tirrell, M. Tsapatsis and D. G. Vlachos, *Chemistry of Materials*, 2000, **12**, 845–853.
158 V. Nikolakis, M. Tsapatsis and D. G. Vlachos, *Langmuir*, 2003, **19**, 4619–4626.
159 G. Xomeritakis, Z. Lai and M. Tsapatsis, *Industrial and Engineering Chemistry Research*, 2001, **40**, 544–552.
160 Z. Lai, M. Tsapatsis and J. P. Nicolich, *Advanced Functional Materials*, 2004, **14**, 716–729.
161 Z. Lai and M. Tsapatsis, *Industrial and Engineering Chemistry Research*, 2004, **43**, 3000–3007.
162 Z. Lai, G. Bonilla, I. Diaz, J. G. Nery, K. Sujaoti, M. A. Amat, E. Kokkoli, O. Terasaki, R. W. Thompson, M. Tsapatsis and D. G. Vlachos, *Science*, 2003, **300**, 456–460.
163 J. Choi, S. Ghosh, L. King and M. Tsapatsis, *Adsorption*, 2006, **12**, 339–360.
164 S. Kumar, T. M. Davis, H. Ramanan, R. L. Penn and M. Tsapatsis, *Journal of Physical Chemistry B*, 2007, **111**, 3398–3403.
165 M. Shete, M. Kumar, D. Kim, N. Rangnekar, D. Xu, B. Topuz, K. V. Agrawal, E. Karapetrova, B. Stottrup, S. Al-Thabaiti, S. Basahel, K. Narasimharao, J. D. Rimer and M. Tsapatsis, *Angewandte Chemie - International Edition*, 2017, **56**, 535–539.

166 M. Choi, K. Na, J. Kim, Y. Sakamoto, O. Terasaki and R. Ryoo, *Nature*, 2009, **461**, 246–249.
167 P. Kumar, K. V. Agrawal, M. Tsapatsis and K. A. Mkhoyan, *Nature Communications*, , DOI:10.1038/ncomms8128.
168 K. Varoon, X. Zhang, B. Elyassi, D. D. Brewer, M. Gettel, S. Kumar, J. A. Lee, S. Maheshwari, A. Mittal, C.-Y. Sung, M. Cococcioni, L. F. Francis, A. v. McCormick, K. A. Mkhoyan and M. Tsapatsis, *Science*, 2011, **334**, 72–76.
169 K. V. Agrawal, B. Topuz, Z. Jiang, K. Nguenkam, B. Elyassi, L. F. Francis and M. Tsapatsis, *AICHE Journal*, 2013, **59**, 3458–3467.
170 M. Tsapatsis, *AICHE journal*, 2014, **60**, 2374–2381.
171 M. Tsapatsis, *Science*, 2011, **334**, 767–768.
172 M. Y. Jeon, D. Kim, P. Kumar, P. S. Lee, N. Rangnekar, P. Bai, M. Shete, B. Elyassi, H. S. Lee, K. Narasimharao, S. N. Basahel, S. Al-Thabaiti, W. Xu, H. J. Cho, E. O. Fetisov, R. Thyagarajan, R. F. Dejaco, W. Fan, K. A. Mkhoyan, J. I. Siepmann and M. Tsapatsis, *Nature*, 2017, **543**, 690–694.
173 D. Kim, M. Shete and M. Tsapatsis, *Chemistry of Materials*, 2018, **30**, 3545–3551.
174 D. Kim, M. Y. Jeon, B. L. Stottrup and M. Tsapatsis, *Angewandte Chemie - International Edition*, 2018, **57**, 480–485.
175 R. Tiriolo, N. Rangnekar, H. Zhang, M. Shete, P. Bai, J. Nelson, E. Karapetrova, C. W. Macosko, J. I. Siepmann, E. Lamanna, A. Lavano and M. Tsapatsis, *Advanced Functional Materials*, 2017, **27**, 1–7.
176 N. Rangnekar, M. Shete, K. V. Agrawal, B. Topuz, P. Kumar, Q. Guo, I. Ismail, A. Alyoubi, S. Basahel, K. Narasimharao, C. W. Macosko, K. A. Mkhoyan, S. Al-Thabaiti, B. Stottrup and M. Tsapatsis, *Angewandte Chemie - International Edition*, 2015, **54**, 6571–6575.
177 A. Navajas, N. Mittal, N. Rangnekar, H. Zhang, A. Cornejo, L. M. Gandía and M. Tsapatsis, *ACS Sustainable Chemistry and Engineering*, 2018, **6**, 15773–15780.
178 H. Zhang, Q. Xiao, X. Guo, N. Li, P. Kumar, N. Rangnekar, M. Y. Jeon, S. Al-Thabaiti, K. Narasimharao, S. N. Basahel, B. Topuz, F. J. Onorato, C. W. Macosko, K. A. Mkhoyan and M. Tsapatsis, *Angewandte Chemie - International Edition*, 2016, **55**, 7184–7187.
179 K. V. Agrawal, B. Topuz, T. C. T. Pham, T. H. Nguyen, N. Sauer, N. Rangnekar, H. Zhang, K. Narasimharao, S. N. Basahel, L. F. Francis, C. W. Macosko, S. Al-Thabaiti, M. Tsapatsis and K. B. Yoon, *Advanced Materials*, 2015, **27**, 3243–3249.
180 M. Tsapatsis and W. Fan, *ChemCatChem*, 2010, **2**, 246–248.
181 A. Schwanke and S. Pergher, *Applied Sciences (Switzerland)*, , DOI:10.3390/app8091636.
182 A. Corma, C. Corell and J. Pérez-Pariente, *Zeolites*, 1995, **15**, 2–8.
183 W. Kolodziejski, C. Zicovich-Wilson, C. Corell, J. Pérez-Pariente and A. Corma, *Journal of Physical Chemistry*, 1995, **99**, 7002–7008.
184 H. Y. Luo, V. K. Michaelis, S. Hodges, R. G. Griffin and Y. Román-Leshkov, *Chemical Science*, 2015, **6**, 6320–6324.

185 V. J. Margarit, M. E. Martínez-Armero, M. T. Navarro, C. Martínez and A. Corma, *Angewandte Chemie - International Edition*, 2015, **54**, 13724–13728.
186 A. W. C. van den Berg, S. T. Bromley, E. Flikkema, J. Wojdel, T. Maschmeyer and J. C. Jansen, *Journal of Chemical Physics*, 2004, **120**, 10285–10289.
187 J. Choi, Z. Lai, S. Ghosh, D. E. Beving, Y. Yan and M. Tsapatsisst, *Industrial and Engineering Chemistry Research*, 2007, **46**, 7096–7106.
188 M. A. Camblor, A. Corma, M.-J. Díaz-Cabañas and C. Baerlocher, *The Journal of Physical Chemistry B*, 1998, **102**, 44–51.
189 B. Elyassi, X. Zhang and M. Tsapatsis, *Microporous and Mesoporous Materials*, 2014, **193**, 134–144.
190 A. Corma, A. Martínez and V. Martínez-Soria, *Journal of Catalysis*, 2001, **200**, 259–269.
191 A. Corma, V. Fornes, S. B. Pergher, Th. L. M. Maesen and J. G. Buglass, *Nature*, 1998, **396**, 353–356.
192 A. Corma, V. Fornés, J. Martínez-Triguero and S. B. Pergher, *Journal of Catalysis*, 1999, **186**, 57–63.
193 S. Maheshwari, E. Jordan, S. Kumar, F. S. Bates, R. L. Penn, D. F. Shantz and M. Tsapatsis, *Journal of the American Chemical Society*, 2008, **130**, 1507–1516.
194 J. Choi and M. Tsapatsis, *Journal of the American Chemical Society*, 2010, **132**, 448–449.
195 S. Sinha Ray and M. Okamoto, *Progress in Polymer Science (Oxford)*, 2003, **28**, 1539–1641.
196 M. E. Giannelis E.P., Krishnamoorti R., *Polymers in Confined Environments. Advances in Polymer Science*.
197 S. A. Monemian, V. Goodarzi, P. Zahedi and M. Torabi Angaji, *Advances in Polymer Technology*, 2007, **26**, 247–257.
198 R. Qi, X. Jin, J. Nie, W. Yu and C. Zhou, *Journal of Applied Polymer Science*, 2005, **97**, 201–207.
199 A. Usuki, N. Hasegawa, H. Kadoura and T. Okamoto, *Nano Letters*, 2001, **1**, 271–272.
200 D. Donescu, M. C. Corobea, V. Uricanu, C. Radovici, S. Serban, S. A. Garea and H. Iovu, *Journal of Dispersion Science and Technology*, 2007, **28**, 671–679.
201 D. C. Lee and L. W. Jang, *Journal of Applied Polymer Science*, 1996, **61**, 1117–1122.
202 K. A. Carrado and L. Xu, *Chemistry of Materials*, 1998, **10**, 1440–1445.
203 C. O. Oriakhi, I. v. Farr and M. M. Lerner, *Clays and Clay Minerals*, 1997, **45**, 194–202.
204 W. Awad and A. R. Amal Esawi, *Proceedings of Multifunctional Nanocomposites and Nanomaterials International Conference*, 2209, 75–80.
205 D. Kim, J. S. Lee, C. F. Barry and J. L. Mead, *Journal of Applied Polymer Science*, 2008, **109**, 2924–2934.
206 L. Liu, Z. Qi and X. Zhu, *Journal of Applied Polymer Science*, 1999, **71**, 1133–1138.
207 T. McNally, W. R. Murphy, C. Y. Lew, R. J. Turner and G. P. Brennan, *Polymer*, 2003, **44**, 2761–2772.

208 P. Sun, J. Zhu, T. Chen, Z. Yuan, B. Li, Q. Jin, D. Ding and A. Shi, *Chinese Science Bulletin*, 2004, **49**, 1664–1666.
209 J. Zhu, X. Wang, F. Tao, G. Xue, T. Chen, P. Sun, Q. Jin and D. Ding, *Polymer*, 2007, **48**, 7590–7597.
210 B. Momani, M. Sen, M. Endoh, X. Wang, T. Koga and H. H. Winter, *Polymer*, 2016, **93**, 204–212.
211 X. Wang, Y. Gao, K. Mao, G. Xue, T. Chen, J. Zhu, B. Li, P. Sun, Q. Jin, D. Ding and A. C. Shi, *Macromolecules*, 2006, **39**, 6653–6660.
212 T. Chen, J. Zhu, B. Li, S. Guo, Z. Yuan, P. Sun, D. Ding and A. C. Shi, *Macromolecules*, 2005, **38**, 4030–4033.
213 V. A. Tanna, J. S. Enokida, E. B. Coughlin and H. H. Winter, *Macromolecules*, 2019, **52**, 6135–6141.
214 W. J. Roth, T. Sasaki, K. Wolski, Y. Song, D. M. Tang, Y. Ebina, R. Ma, J. Grzybek, K. Kałahurska, B. Gil, M. Mazur, S. Zapotoczny and J. Cejka, *Science Advances*, , DOI:10.1126/sciadv.aay8163.
215 S. Sabnis, V. A. Tanna, C. Li, J. Zhu, V. Vattipalli, S. S. Nonnenmann, G. Sheng, Z. Lai, H. H. Winter and W. Fan, *Chemical Communications*, 2017, **53**, 7011–7014.
216 P. Frontera, F. Testa, R. Aiello, S. Candamano and J. B. Nagy, *Microporous and Mesoporous Materials*, 2007, **106**, 107–114.
217 R. Schenkel, J. Barth, J. Kornatowski and A. Lercher, *Studies in surface science and catalysis*, 2002, **142**, 69–76.
218 M. A. Camblor, A. Corma, M. J. Díaz-Cabañas and C. Baerlocher, *Journal of Physical Chemistry B*, 1998, **102**, 44–51.
219 M. Geri, B. Keshavarz, T. Divoux, C. Clasen, D. J. Curtis and G. H. McKinley, *Physical Review X*, 2018, **8**, 41042.
220 M. Mours and H. H. Winter, *Rheologica Acta*, 1994, **33**, 385–397.
221 V. Tanna, C. Wetzel and H. Henning Winter, *Rheologica Acta*, 2017, **56**, 527–537.
222 W. J. Roth, P. Chlubná, M. Kubů and D. Vitvarová, *Catalysis Today*, 2013, **204**, 8–14.
223 B. Gil, W. Makowski, B. Marszalek, W. J. Roth, M. Kubu, J. Čejka and Z. Olejniczak, *Journal of the Chemical Society. Dalton Transactions*, 2014, **43**, 10501–10511.
224 G. G. Juttu and R. F. Lobo, *Microporous and Mesoporous Materials*, 2000, **40**, 9–23.
225 A. Corma, U. Diaz, V. Fornés, J. M. Guil, J. Martínez-Triguero and E. J. Creyghton, *Journal of Catalysis*, 2000, **191**, 218–224.
226 W. J. Roth, J. Čejka, R. Millini, E. Montanari, B. Gil and M. Kubu, *Chemistry of Materials*, 2015, **27**, 4620–4629.
227 W. J. Roth, T. Sasaki, K. Wolski, Y. Song, D. M. Tang, Y. Ebina, R. Ma, J. Grzybek, K. Kałahurska, B. Gil, M. Mazur, S. Zapotoczny and J. Cejka, *Science Advances*, , DOI:10.1126/sciadv.aay8163.
228 D. P. Serrano and R. van Grieken, 2001, **46**, 35–46.

229 K. Egeblad, M. Kustova, S. K. Klitgaard, K. Zhu and C. H. Christensen, 2007, **101**, 214–223.
230 D. Sung, J. Chang, J. Hwang, S. Park and J. Man, 2004, **68**, 77–82.
231 A. Kuperman, S. Nadimi, S. Oliver, G. A. Ozin, J. M. Garcest and M. M. Olkent, 239–242.
232 J. L. Guth, H. Kessler, J. M. Higel, J. M. Lamblin, J. Patarin, A. Seive, J. M. Chezeau, R. Wey, D. Recherche, S. No, E. N. Supérieure, D. Chimie, A. Werner and M. Cedex, .
233 W. G. Kim, S. Choi and S. Nair, *Langmuir*, 2011, **27**, 7892–7901.
234 K. V. Agrawal, B. Topuz, T. C. T. Pham, T. H. Nguyen, N. Sauer, N. Rangnekar, H. Zhang, K. Narasimharao, S. N. Basahel, L. F. Francis, C. W. Macosko, S. Al-Thabaiti, M. Tsapatsis and K. B. Yoon, *Advanced Materials*, 2015, **27**, 3243–3249.